（要約）

博士論文

Studies on Crystallinity of Cellulose Nanofibers

（セルロースナノファイバーの結晶性に関する研究）

Kazuho Daicho

Graduate School of Agricultural and Life Sciences,
The University of Tokyo

Contents

Contents

Chapter 1

General introduction

1.1 Introduction

In 2016, the Paris Agreement was signed by countries party to the United Nations Framework Convention on Climate Change (UNFCCC)[1]. The Paris Agreement is dedicated to combatting climate change, as well as accelerating the actions and investments needed for a sustainable low-carbon future. Since 2016, the idea of sustainability has become a financially valuable target for investment. Globally, people are becoming increasingly aware of the benefits of biomass. To realize a sustainable low-carbon society, we need to investigate techniques for conversion of biomass into usable materials, as well as methods for efficient and cyclical production of these materials, through the promotion of fundamental science and applied research.

Cellulose is the most abundant biopolymer on Earth[2], with an estimated production of approximately 7.5×10^{10} tons per year[3]. Cellulose is synthesized by various living organisms, such as higher plants, bacteria, algae, fungi, and tunicates. The primary sources of cellulose for products are the cell walls of trees and cotton plants. Plant cellulose is isolated as pulp fiber, and historically used in the textile, pulp, and paper industries. Recently, cellulose has been utilized for packing materials, medical products, cosmetics, and food additives.

Cellulose is composed of a linear biopolymer, (1→4)-*β*-D-glucan, and its chemical structure is shown in Figure 1.1. The degree of polymerization depends on the cellulose source material; typical DP values are 6000–9000 for bacterial cellulose, ~5000 for unbleached kraft paper pulp, 2000 for acidic sulfite dissolving pulp, and 300–600 for rayon staple fiber[3].

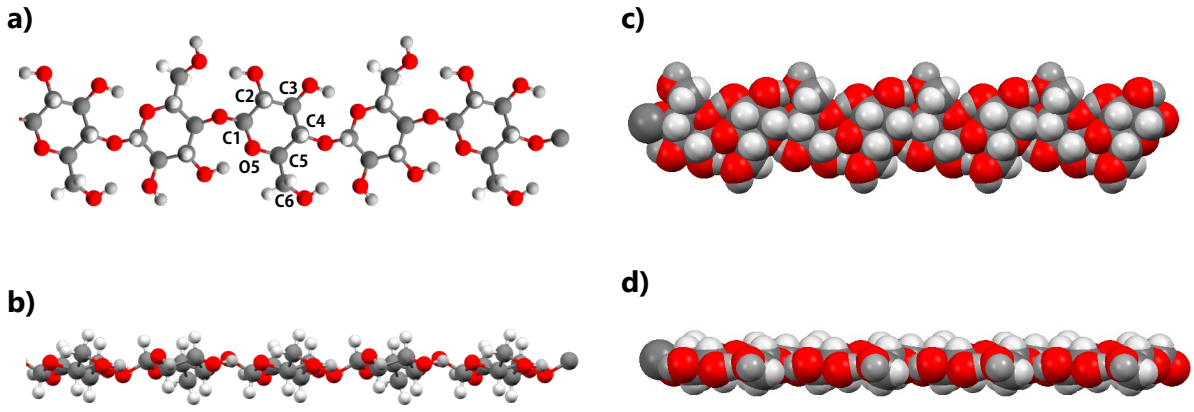

Figure 1.1. Schematic models of cellulose molecules. The ball-and-stick form models are viewed **a)** perpendicular to the flat surface of the molecule and **b)** along the molecular axis. The space-filling style models are viewed **c)** perpendicular to the flat surface of the molecule and **d)** along the molecular axis. The red, gray, and white balls indicate oxygen, carbon, hydrogen atoms, respectively.

1.2 Crystal structure of native cellulose

1.2.1 Pyranose ring conformation

The conformation of a six-membered aliphatic ring, such as a glucopyranosyl unit, can be expressed as "boat", "half-chair", "chair" or "skew" in principle, which can be described by Cremer-Pucker puckering parameters. When the parameter θ is close to 0°, the ring sits in the classical $^4C_1$ chair conformation, which is the most stable for glucose. In crystalline cellulose, glucose takes the $^4C_1$ chair conformation with $\theta = 2–10°$[3].

1.2.2 Glycosidic linkage

The rotation around the glycosidic bonds in polysaccharides determines flexibility. The solid-state structure of cellulose is governed by three main parameters[4]: **1)** the conformation of the cellulose chain, which is fixed with the following glycosidic torsion angles: O5–C1–O1–C4 (ϕ) and C1–O1–C4–C5 (ψ) (Figure. 1.2a). **2)** The conformation of the exocyclic $C6H_2OH$ group, which is described by the dihedral angle χ around the C5-C6 single bond. The $C6H_2OH$ group has three possible arrangements: trans-gauche (*tg*), gauche-trans (*gt*), and gauche-gauche (*gg*) (Figure 1.2b). The notation *tg* indicates that the O6 position is trans to O5 and gauche to C4; *gt* indicates that the O6 position is gauche to O5 and trans to C4; and finally, *gg* indicates that the O6 position is gauche to both O5 and C4.

Conformation can be identified by using solid-state ^{13}C NMR. The signals resulting from the *gg*, *gt*, and *gt* conformations appear at 60–62.6 ppm, 62.5–64.5 ppm, and 65.5–66.5 ppm, respectively[5].

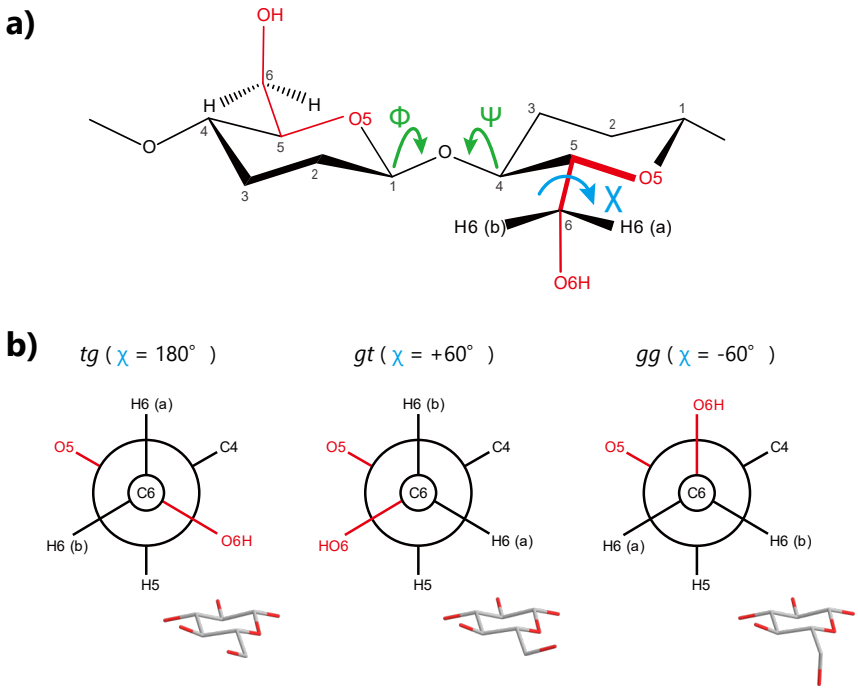

Figure 1.2. Geometric parameters for solid structure of cellulose. a) Glycosidic torsion angles (ϕ and ψ). **b)** Conformation of hydroxymethyl groups: *gg* (gauche-gauche), *gt* (gauche-trans), and *tg* (trans-gauche).

1.2.3 Unit cells of cellulose Iα and Iβ

Cellulose has four primary polymorphs: cellulose I, II, III, and IV. Cellulose I (naturally occurring cellulose) has two allomorphs Iα and Iβ[6-9], which coexist in various proportions depending on the cellulose source[10-12]. Algae and bacteria mostly produce Iα[13, 14], while terrestrial plants mostly produce Iβ[15]. Cellulose Iα is thermodynamically metastable and can be converted into cellulose Iβ by annealing at temperatures over 260 °C [13, 16], or by ultrasonication[17].

Figure 1.3 shows the schematic images of the unit cells of cellulose Iα and Iβ. Cellulose Iα is a triclinic P1 unit cell crystal (a = 6.717 Å, b = 5.962 Å, c = 10.400 Å, α = 118.08°, β = 114.80°, γ = 80.37°, Density = 1.61 g/cm^3) which contains a unique chain with two different glucosyl residues[18]. Cellulose Iβ is a monoclinic $P2_1$ unit cell containing two

conformationally distinct chains (*a* =7.784 Å, *b* = 8.201 Å, *c* = 10.380 Å, *γ* = 96.5°, density = 1.63 g/cm^3), which are referred to as the corner and center chains[19]. The cellulose chains in both cellulose Iα and Iβ are organized in a parallel-up fashion, where the reducing end of the chain is oriented in the same direction as the unit cell *c*-axis[20]. In cellulose I*α*, the chains are continuously shifted along the molecular axis by *c*/4 (~2.58 Å) against the adjacent sheet. In contrast the sheets in cellulose Iβ are alternately shifted, and the center chains are shifted by *c*/4 against the corner chains[12].

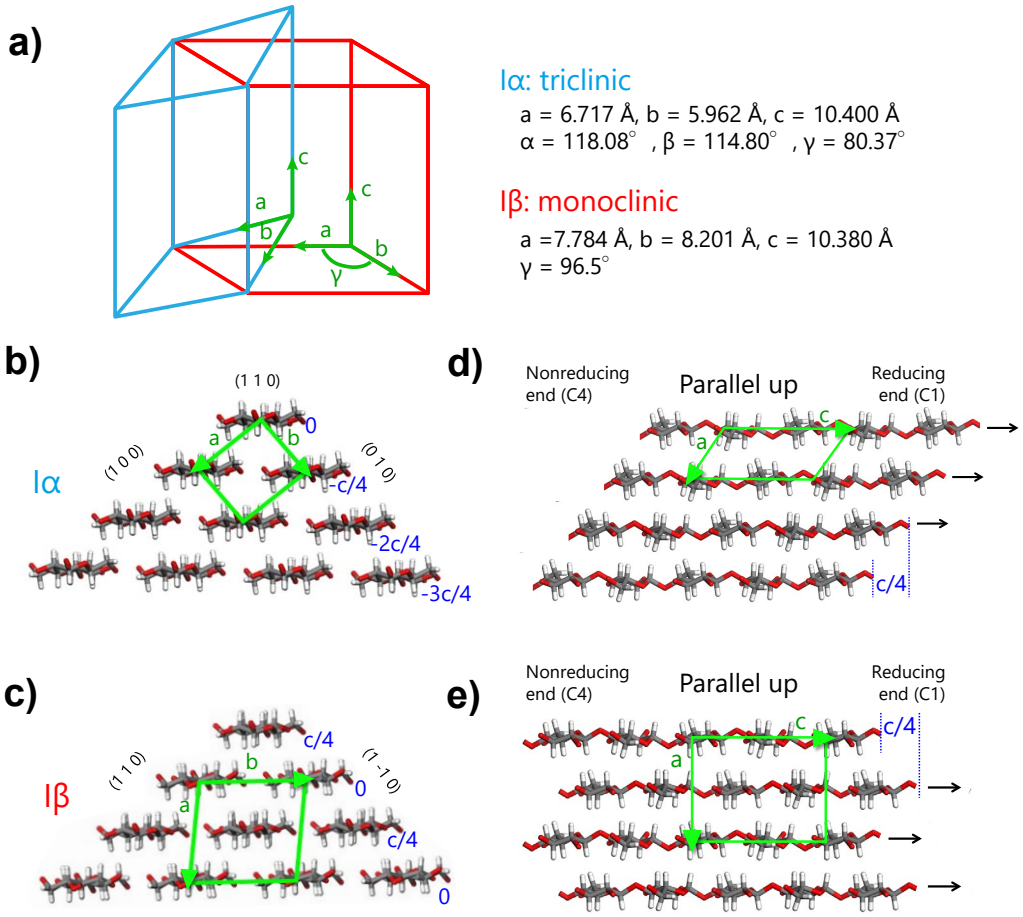

Figure 1.3. Schematic images for unit cell of cellulose I*α* and I*β*. a) Relative configuration of I*α* with respect to I*β* unit cell. Schematic projections along the chain direction with the **b)** Iα and **c)** I*β* unit cells. Schematic projections of four cellulose chains viewed **d)** parallel to the (1 1 0) planes of the I*α* and **e)** along b axis direction of I*β*.

1.2.4 Intra / Inter-hydrogen bonding

In cellulose I, a variety of hydrogen bonds are formed. O2, O3, and O6 act as donors or acceptors of hydrogen bonds, along with ether oxygen at O4 and O5 (ring oxygen), which

acts as an acceptor[18, 19]. Although strong hydrogen bonds are not formed between the hydrogen-bonding sheets (Figure 1.4), the intersheets are stabilized by hydrophobic interactions and weak C–H···O hydrogen bonds[18, 19, 21, 22].

In both cellulose Iα and β, all O6 primary alcohol groups exist in *tg* conformations[18, 19], which can establish intra-chain hydrogen bonds. The O3 secondary alcohol group of each residue donates its proton to the O5 ring atom of a neighboring residue to form an intra-chain hydrogen bond. The O2 secondary alcohol and O6 hydroxymethyl groups also form an intra-chain hydrogen bond within the sheets. Here, the position of the H atoms covalently bound to O2 and O6 is variable. Thus, the intra-hydrogen bond pattern at O2 and O6 is intrinsically disorganized, whereas the intramolecular hydrogen bond at O3 is explicitly well organized.

Cellulose I contains one strong inter-chain hydrogen bond, O6–H···O3, while the other weak hydrogen bond, O6–H···O2, occur in the hydrogen-bonding sheet. The two hydrogen atoms involving HO2 and HO6 are delocalized into two locations each, and two hydrogen-bonding patterns occur (Networks A and B in Figure 1.4)[22].

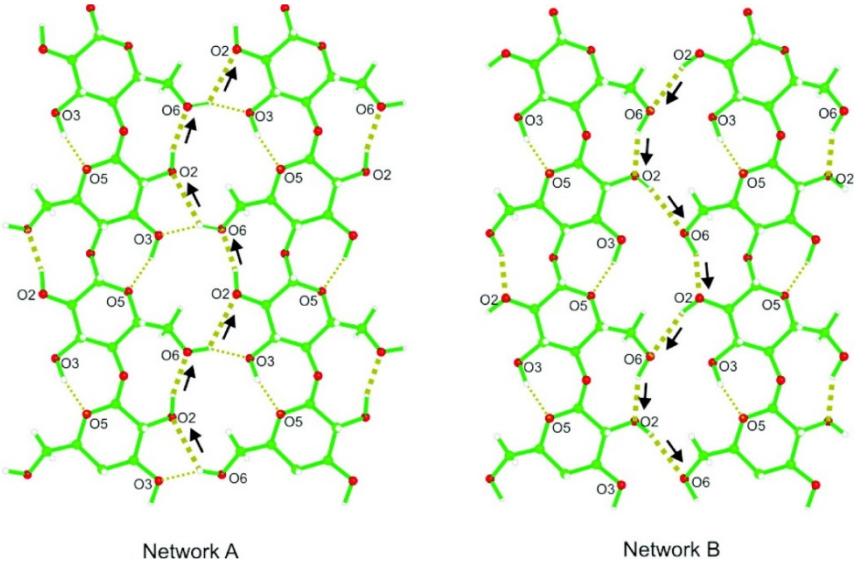

Figure 1.4. Two types of hydrogen bonding networks, pattern A and pattern B.
©Nishiyama Y. *et al. Biomacromolecules* **9** (11), 3133–3140, doi.org/10.1021/bm800726v.

1.3 Physical property of cellulose I

The physical properties of cellulose I, such as elastic modulus, deformation by stain, and thermal expansion, are directly related to its crystal structure. The elastic modulus of cellulose I has been measured using various experimental and simulation methods[23, 24]. The

experimental modulus in the axial direction is reported to be 137–220 GPa[23-26]. To describe the axial elasticity mechanism, the importance of hydrogen bonds (as well as covalent bonds) is often emphasized, although the intrinsic stiffness of hydrogen bonds is relatively low. According to a recent paper, the total contribution of axial stiffness from hydrogen bonds is only 12 % [27]. Several other simulation studies have proposed similar ideas[28-30]. Hydrogen bonds may also contribute to preservation of the crystal structure and may also help direct axial deformation mechanisms towards higher energy deformation and stiffness[27, 29]. Additionally, the modulus in the b-axis direction is lower than the axial modulus, and is estimated to be 14.8 GPa according to the inelastic XRD method[31].

Poisson's ratio is the negative of the ratio of the lateral or transverse strain to the axial strain in tensile loading, which is an important physical constant for anisotropy in deformation, along with elastic moduli. The experimental Poisson's ratio of cellulose Iβ is 0.377, 0.639, and 0.442 for [2 0 0]/[0 0 4], [1 1 0]/[0 0 4], and [1 -1 0]/[0 0 4], respectively[32].

The linear coefficients of thermal expansion (CTE) of the a and b axes of cellulose Iβ are 43 ppm K^{-1} and 5 ppm K^{-1} at room temperature, respectively[33]. In other words, upon heating, cellulose Iβ easily expands along the a-axis direction rather than the b-axis. Such anisotropic behavior between the a and b axes can be ascribed to the inter-chain hydrogen-bonding system in cellulose Iβ[33, 34].

1.4 Cellulose microfibril

1.4.1 Biosynthesis

In nature, cellulose chains are continuously synthesized and elongated by cellulose synthases of membrane-embedded glycosyltransferases at the plasma membrane[35, 36]. Cellulose synthase catalyzes glucose transfer from uridine diphosphate–glucose (UDP-glucose, the donor) to the terminal C4 hydroxyl of the nascent cellulose polymer (the acceptor)[37]. Recently, the structure of the bacterial cellulose synthase (BcsA) has been revealed, providing insights into the mechanism responsible for coupling of cellulose synthesis and translocation of individual glucan chains[35] (Figure 1.5). At the plasma

membrane, the cellulose synthases are densely assembled to form subunits, and further build up a supramolecular complex called the terminal complex (TC).

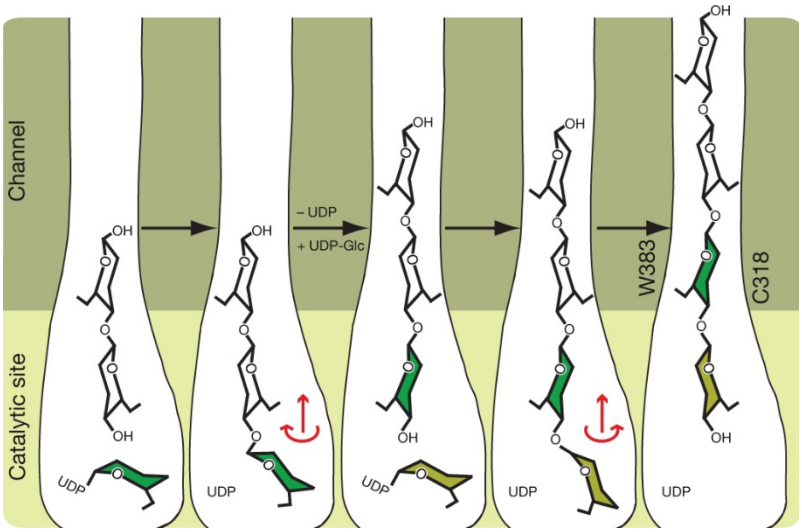

Figure 1.5. Proposed model for cellulose biosynthesis and translocation. After glycosyl transfer, the newly added glucose could rotate around the acetal linkage into the plane of the polymer. The rotation direction would be determined by steric interactions and formation of the intra-chain hydrogen bonds between O3H···O5. The glucan may be translocated into the channel during this relaxation. This process would be repeated with a second UDP-Glucose, but the rotation direction after the glycosyl transfer would be in the opposite direction due to steric constraints. Alternatively, the glucan may not be translocated into the channel until UDP is replaced by UDP-Glucose. © JLW Morgan *et al. Nature* **000**, 1-6 (2012) doi:10.1038/nature11744.

TCs exhibit different organization types depending on cellulose resources, and so far, two main types of TCs have been reported[38]. One is linear TCs that consist of parallel arrays of cellulose synthase proteins, which are typically visible in some bacterial biosynthetic machinery. The other is the rosette TCs which are visible in higher plants and algae, where they are typically organized into a symmetrical hexame[38-42] shape, although octagonal symmetry has also been reported in a limited number of algae species.

As a cellulose chain is translocated outside the cell membrane through the transmembrane channel of each cellulose synthase in the TC, the chain's hydrophobic groups are ejected from the water molecules, and the adjacent chains are entropically stacked through hydrophobic interactions. Accordingly, a dozen or several dozen cellulose chains form a-few-nanometers-wide crystalline fibrils of cellulose I, with hydrophobic methine groups and

hydrophilic hydrogen groups in the axial and equatorial directions of the molecular sheets, respectively. These crystalline fibrils are histologically defined in structure as "cellulose microfibrils."

In the cell walls of wood, microfibrils are interact strongly with each other via other biopolymers, such as hemicelluloses and lignin, and play a significant role in the structural support of plant bodies. Figure 1.6 shows a schematic model of the biosynthesis of microfibrils in a plant cell wall.

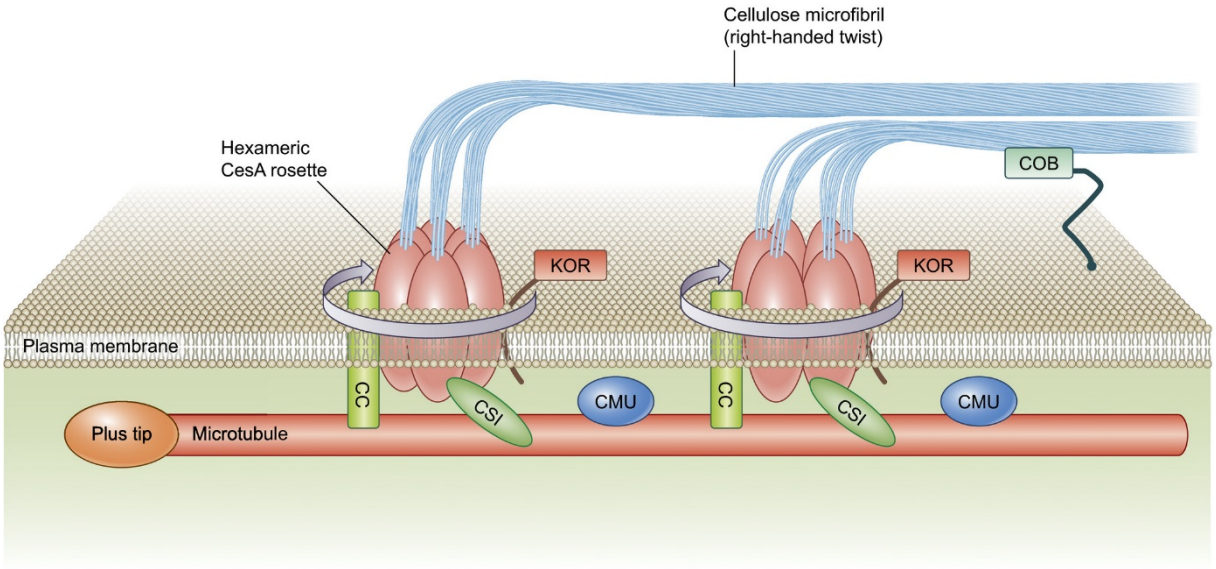

Figure 1.6. Proposed model for microfibril arrangement[43]. Cellulose (blue fibrils) is produced by cellulose synthase rosettes (light red), which are integral to the plasma membrane (yellow). The rosette TCs move along microtubules (red bar) forward through the force generated by cellulose polymerization. The microtubules serve as guiding tracks for the rosettes and determine the direction of the cellulose microfibril alignment. Arrangement of microtubules differs between bioresources. In wood, within the second cell wall the microtubules are likely to be parallel to one another. The cellulose synthase interacting (CSI) protein (green) is a linker protein that connects the cellulose synthase rosettes with microtubules. Another linker protein has recently been discovered, called the companion of cellulose synthase (CC) (light green). Additional microtubule-associated proteins (MAPs) are also involved in the guidance process (e.g., cellulose synthase-microtubule uncoupling (CMU; blue circles)), but how exactly this occurs remains unclear. Additional proteins known to be involved in cellulose biosynthesis are cobra (COB) and korrigan (KOR). Cellulose microfibrils have frequently been reported as having regular (frequently right-handed) twists, which implies that the rosettes are rotating while spinning out the nascent fibril. However, it is currently not known how the linker proteins CSI and CC would respond to such hypothetical rotation. © Henrik B. and Agnes B. *New Phytologist*, **225** (1), 53–69 (2019) doi: (10.1111/nph.16034)

1.4.2 Morphology

Microfibril morphology, along with a number of chains containing microfibrils, is associated with the organization of the TC. It has been proposed that in higher plants, each subunit in the TC consists of trimers, tetramers, or hexamers, thereby giving rise to 18, 24, or 36 cellulose synthases (CesAs) in each TC, respectively. Assuming that all individual CesA proteins are active synthases, a corresponding maximum number of chains are subsequently crystallized to form microfibrils[44, 45]. Recently, several analytical techniques have been developed, and the results of multiple analytical approaches including scattering analysis, solid-state NMR analysis, molecular simulations, and image analysis of cellulose microfibrils or globular components of rosette TCs support that the cellulose microfibril consists of less than 36 chains, with most containing approximately 18–24 chains[46-52]. The elucidation of the precise structure of the microfibrils, including the number of constituent chains, shape, and crystallinity, provides significant insight into cellulose biosynthesis mechanisms and the formation of hierarchical structures such as wood cell walls.

1.5 Cellulose Nanofibers (CNFs)

In recent years, several techniques have been developed for fine dispersing microfibrils in water as cellulose nanofibers (CNFs). CNFs are attracting attention as sustainable materials.

1.5.1 CNF production

CNFs can be obtained by disintegration of the cellulose source material into single microfibrils or fine-bundled microfibrils. The primary source of CNFs is wood. Wood is disintegrated into a pulp consisting of tiny fibers by cooking, and the pulp is purified by bleaching. The bleached pulp fibers are further disintegrated into CNFs. Conventionally, the process of further disintegration of pulp fibers is a high-energy consuming process, and the resulting CNFs are thick and heterogeneous in diameter (10–100 nm)[53, 54], because of strong cohesion between microfibrils in pulp fibers. However, chemical[55-57] or enzymatic[58, 59] pretreatment has considerably alleviated these problems. The representative pretreatment is

surface modification using a water-soluble nitroxyl radical of 2,2,6,6-*tetra*methylpiperidinyl-1-oxyl (TEMPO) as a catalyst.

1.5.2 TEMPO oxidation

Catalytic oxidation using stable nitroxyl radicals such as TEMPO is one of method for selective oxidation of primary alcohol groups into aldehydes and/or carboxylic acid groups. Application of the TEMPO-oxidation to polysaccharides offers highly selective conversion of primary hydroxyl groups to carboxylate ones in aqueous medium.

Nooy *et al.* first applied this catalytic oxidation to water-soluble polysaccharides such as potato starch, amylodextrin and pullulan, where NaClO was used as a primary oxidant with catalytic amounts of NaBr and TEMPO under weakly alkaline conditions[60]. Selective oxidation of the C6 primary hydroxyl groups of the polysaccharides to carboxylate ones was achieved, and the corresponding polyuronic acids were obtained quantitatively.

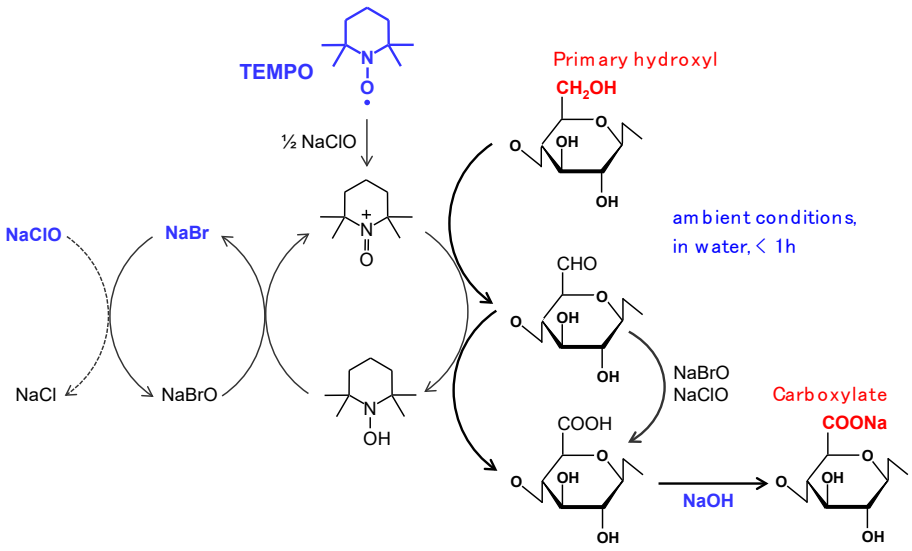

Figure 1.7. The oxidation of cellulose in the TEMPO/NaBr/NaClO reaction system.

1.5.3 TEMPO-oxidized CNF

When wood cellulose is oxidized in the TEMPO/NaBr/NaClO system, the C6 hydroxy groups exposed on the cellulose microfibril surfaces are oxidized via regioselectivity to sodium carboxylate groups while maintaining their crystallinity and morphology (Figure 1.7)

[60-62]. The sodium carboxylate groups are then dissociated in water, and electric double layer repulsion is induced between the assembled fibrils. Accordingly, the carboxylated microfibrils (carboxylate content >1.2 mmol/g) readily disperse in water as physically isolated CNFs (2–3 nm in width) by mechanical disintegration (Figure 1.8)[61].

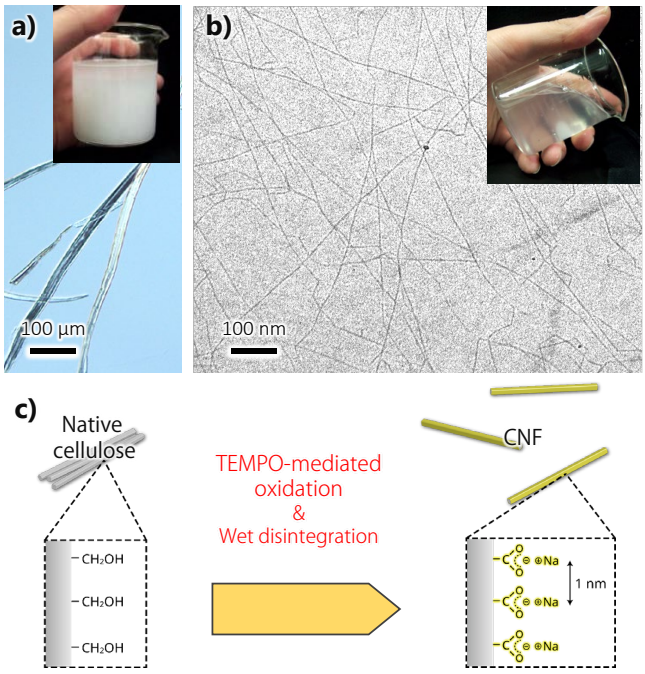

Figure 1.8. CNF production (a) Pulp fibers chemically modified via TEMPO-oxidation. **(b)** CNFs obtained by disintegration of pulp in water[55]. **(c)** Schematic model for TEMPO-mediated oxidation and wet disintegration of native cellulose.

Today, a wide variety of CNFs with different compositions, morphologies, and surface functionalities can be manufactured (Figure 1.9)[57, 62-70]. Various functional groups are responsible for the dispersibility and morphology of CNFs; those produced via the TEMPO-oxidation method have carboxyl groups on the surface. Functionalization can also be attained by using the carboxyl groups as reaction points. Examples include: (1) exchange of the surface carboxyl group counter ion with a multivalent metal ion, which causes the CNF film to have low water resistance[66]; (2) exchange the surface carboxyl group counter ion with quaternary alkylammonium, which causes the CNF film to exhibit hydrophobicity[71]; (3) grafting the aminated polymer onto the carboxyl group, which allows the CNFs to be

dispersible in low-polarity solvents such as chloroform and toluene[68] so that the CNFs can be homogeneously blended with resin without any agglomeration. Furthermore, recent advances in technology have enabled us to precisely design the CNF surface structure to achieve the desired material property, which includes (4) blending organic and inorganic ions as the counter ion of the carboxyl group to precisely control the film properties[69], and (5) controlling the thickness and density of the polymer layer grafted onto the surface of the CNF[70].

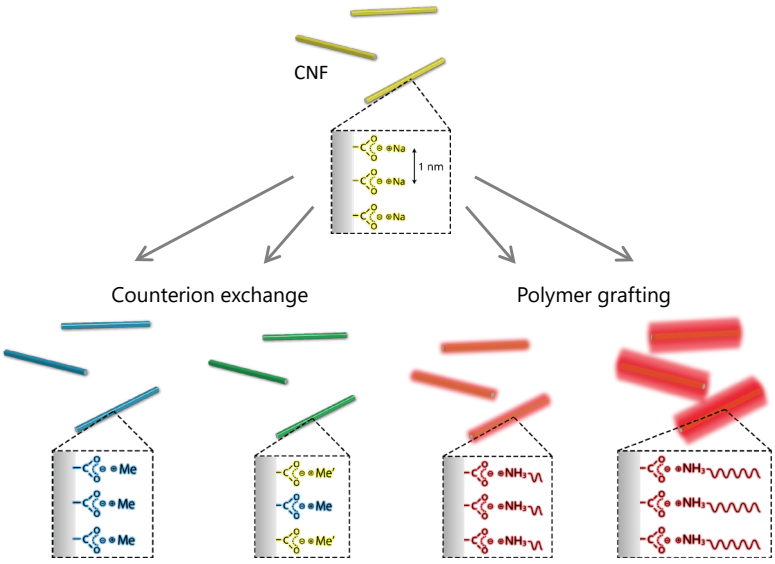

Figure 1.9. Surface functionalization of CNFs.

1.5.4 CNF application

Individualized CNFs produced by TEMPO oxidation process exhibit high strength (2–6 GPa)[72], high stiffness (130–150 GPa)[26, 73, 74], low thermal expansion along the *c*-axis direction (0–6 ppm K^{-1})[75, 76], and high thermal conductivity[77]. These properties are related to the crystallinity of CNFs, or the uniaxial orientation and lateral packing of cellulose molecules.

Through assembly, the individualized CNFs can be structured into various forms, such as film materials, porous materials, and CNF-plastic composites[78-82]. These CNF assemblies possess unique properties, as summarized in Figure 1.10, and are expected to be utilized in the establishment of a low-carbon society.

By evaporative drying of a dispersion of individualized CNFs, optically transparent films can be obtained. In the film, the CNFs are locally oriented and stacked in a plywood-like manner at the nanoscale by consolidation of the CNF alignment in aqueous dispersions. The CNF film possess high strength (tensile strength: 200–400 MPa; Young's modulus: 10–15 GPa), thermal expansion as low as for glasses (6–10 ppm K^{-1}), and superior gas-barrier properties (~0.002 mL μm m^{-2} $day^{-1}kPa^{-1}$), high thermal conductivity and electrical resistivity. These multi-functional CNF films have attracted attention as conceptually new "transparent papers". Their possible applications range from structural members of energy, electronic, and sensing devices to direct uses as display panels and packaging materials[68, 78, 81, 83, 84].

In contrast, by freeze drying or supercritical drying of the CNF dispersion, porous materials with a high specific surface area (500–600 m^2g^{-1}) and high porosity (98–99.7%) can be obtained[81]. In the porous materials, CNFs are partially assembled to form a network structure with fine, anisotropic pores. The porous materials exhibit low thermal conductivity comparable to vacuum insulators (0.015–0.04 $Wm^{-1}K^{-1}$), high optical transparency, and high mechanical property. The porous materials have attracted attention as "transparent insulator", which are expected as candidates for transparent insulators in offices and automobiles.

Furthermore, CNFs are utilized as a reinforcing material for plastics, because of the excellent mechanical and thermomechanical properties of the CNFs[85].

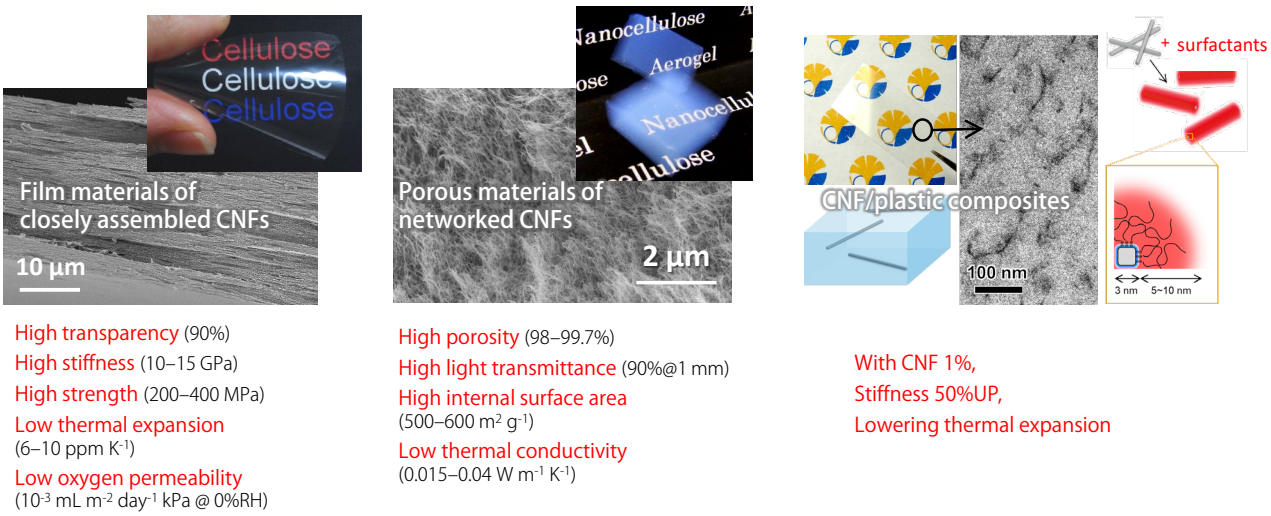

High transparency (90%)
High stiffness (10–15 GPa)
High strength (200–400 MPa)
Low thermal expansion (6–10 ppm K^{-1})
Low oxygen permeability (10^{-3} mL m^{-2} day^{-1} kPa @ 0%RH)

High porosity (98–99.7%)
High light transmittance (90%@1 mm)
High internal surface area (500–600 m^2 g^{-1})
Low thermal conductivity (0.015–0.04 W m^{-1} K^{-1})

With CNF 1%,
Stiffness 50%UP,
Lowering thermal expansion

Figure 1.10. CNF assemblies. Film materials of closely assembled CNFs (left). Porous materials of networked CNFs (middle). CNF/plastic composite (right).

1.6 Objectives

Many CNF production process have been developed, and a variety of CNFs with different chemical compositions, morphologies, and surface functionalities are widely available. However, technology for exploiting the potential of CNFs has not been established, so that the practical application of CNFs remains hindered. One reason for the situation is that the structure of the CNFs is still not understood indeed.

The excellent properties of CNFs, such as high modulus and high thermal conductivity, are related to the crystallinity of cellulose. Therefore, understanding the crystallinity of CNF is vital for exploiting potential. Unfortunately, this area is still lacking. The purpose of this study is thus to investigate the influence of the CNF production process on the crystallinity. A comprehensive analysis of a series of CNFs with different chemical compositions, morphologies, and surface functionalities was performed.

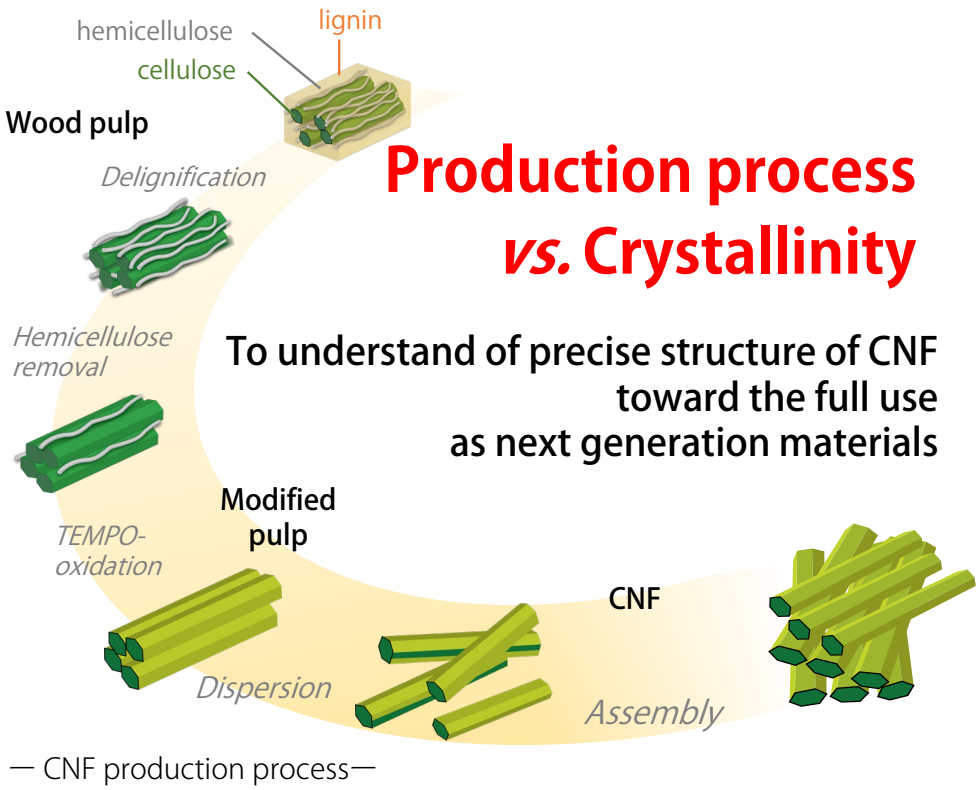

Figure 1.11. Purpose of my research

1.7 Reference

1. What is the Paris Agreement? https://unfccc.int/process-and-meetings/the-paris-agreement/the-paris-agreement

2. Bar-On, Y. M.; Phillips, R.; Milo, R., The biomass distribution on Earth. *Proceedings of the National Academy of Sciences* **2018,** *115* (25), 6506-6511.

3. French, A. D.; Pérez, S.; Bulone, V.; Rosenau, T.; Gray, D., Cellulose. In *Encyclopedia of Polymer Science and Technology*, 2018; pp 1-69.

4. torsion angle. In *IUPAC Compendium of Chemical Terminology*, 2009.

5. Horii, F.; Hirai, A.; Kitamaru, R., Solid-state 13C-NMR study of conformations of oligosaccharides and cellulose. *Polymer Bulletin* **1983,** *10* (7-8), 357-361.

6. Atalla, R. H.; Vanderhart, D. L., Native cellulose: a composite of two distinct crystalline forms. *Science* **1984,** *223* (4633), 283-5.

7. VanderHart, D. L.; Atalla, R. H., Studies of microstructure in native celluloses using solid-state carbon-13 NMR. *Macromolecules* **1984,** *17* (8), 1465-1472.

8. Horii, F.; Hirai, A.; Kitamaru, R., CP/MAS carbon-13 NMR spectra of the crystalline components of native celluloses. *Macromolecules* **1987,** *20* (9), 2117-2120.

9. Sugiyama, J.; Persson, J.; Chanzy, H., Combined infrared and electron diffraction study of the polymorphism of native celluloses. *Macromolecules* **1991,** *24* (9), 2461-2466.

10. Horikawa, Y.; Sugiyama, J., Localization of crystalline allomorphs in cellulose microfibril. *Biomacromolecules* **2009,** *10* (8), 2235-9.

11. Imai, T.; Sugiyama, J., *Macromolecules* **1998,** *31*, 6275.

12. Sugiyama, J.; Vuong, R.; Chanzy, H., Electron diffraction study on the two crystalline phases occurring in native cellulose from an algal cell wall. *Macromolecules* **1991,** *24* (14), 4168-4175.

13. Yamamoto, H.; Horii, F., CPMAS carbon-13 NMR analysis of the crystal transformation induced for Valonia cellulose by annealing at high temperatures. *Macromolecules* **1993,** *26* (6), 1313-1317.

14. Imai, T.; Sugiyama, J.; Itoh, T.; Horii, F., Almost Pure Iα Cellulose in the Cell Wall of Glaucocystis. *Journal of Structural Biology* **1999,** *127* (3), 248-257.

15. Belton, P. S.; Tanner, S. F.; Cartier, N.; Chanzy, H., High-resolution solid-state carbon-13 nuclear magnetic resonance spectroscopy of tunicin, an animal cellulose. *Macromolecules* **1989,** *22* (4), 1615-1617.

16. Wada, M.; Kondo, T.; Okano, T., Thermally induced crystal transformation from cellulose I α to I β. *Polymer journal* **2003,** *35* (2), 155-159.

17. Briois, B.; Saito, T.; Pétrier, C.; Putaux, J.-L.; Nishiyama, Y.; Heux, L.; Molina-Boisseau, S., $I\alpha \rightarrow I\beta$ transition of cellulose under ultrasonic radiation. *Cellulose* **2013,** *20* (2), 597-603.

18. Nishiyama, Y.; Sugiyama, J.; Chanzy, H.; Langan, P., Crystal structure and hydrogen bonding system in cellulose I(alpha) from synchrotron X-ray and neutron fiber diffraction. *J Am Chem Soc* **2003,** *125* (47), 14300-6.

19. Nishiyama, Y.; Langan, P.; Chanzy, H., Crystal structure and hydrogen-bonding system in cellulose Ibeta from synchrotron X-ray and neutron fiber diffraction. *J Am Chem Soc* **2002,** *124* (31), 9074-82.

20. Koyama, M.; Helbert, W.; Imai, T.; Sugiyama, J.; Henrissat, B., Parallel-up structure evidences the molecular directionality during biosynthesis of bacterial cellulose. *Proc Natl Acad Sci U S A* **1997,** *94* (17), 9091-5.

21. Mazeau, K., Structural Micro-heterogeneities of Crystalline Iβ-cellulose. *Cellulose* **2005,** *12* (4), 339-349.

22. Nishiyama, Y.; Johnson, G. P.; French, A. D.; Forsyth, V. T.; Langan, P., Neutron crystallography, molecular dynamics, and quantum mechanics studies of the nature of hydrogen bonding in cellulose Ibeta. *Biomacromolecules* **2008,** *9* (11), 3133-40.

23. Sakurada, I.; Nukushina, Y.; Ito, T., Experimental determination of the elastic modulus of crystalline regions in oriented polymers. *J. Polym. Sci.* **1962,** *57*, 651.

24. Nishino, T.; Takano, K.; Nakamae, K., *J. Polym. Sci., Part B: Polym. Phys.* **1995,** *33*, 1647.

25. Diddens, I.; Murphy, B.; Krisch, M.; Muller, M., Anisotropic Elastic Properties of Cellulose Measured Using Inelastic X-ray Scattering. *Macromolecules* **2008,** *41* (24), 9755-9759.

26. Šturcová, A.; Davies, G. R.; Eichhorn, S. J., Elastic modulus and stress-transfer properties of tunicate cellulose whiskers. *Biomacromolecules* **2005,** *6* (2), 1055-1061.

27. Djahedi, C.; Bergenstrahle-Wohlert, M.; Berglund, L. A.; Wohlert, J., Role of hydrogen bonding in cellulose deformation: the leverage effect analyzed by molecular modeling. *Cellulose* **2016,** *23* (4), 2315-2323.

28. Altaner, C. M.; Thomas, L. H.; Fernandes, A. N.; Jarvis, M. C., How cellulose stretches: synergism between covalent and hydrogen bonding. *Biomacromolecules* **2014,** *15* (3), 791-8.

29. Wohlert, J.; Bergenstråhle-Wohlert, M.; Berglund, L. A., Deformation of cellulose nanocrystals : entropy, internal energy and temperature dependence. *Cellulose* **2012,** *19*, 1821.

30. Nishiyama, Y., Structure and properties of the cellulose microfibril. *Journal of Wood Science* **2009,** *55* (4), 241-249.

31. Diddens, I.; Murphy, B.; Krisch, M.; Müller, M., Anisotropic Elastic Properties of Cellulose Measured Using Inelastic X-ray Scattering. *Macromolecules* **2008,** *41* (24), 9755-9759.

32. Nakamura, K.; Wada, M.; Kuga, S.; Okano, T., *J. Polym. Sci., Polym. Phys.* **2004,** *42*, 1206.

33. Wada, M., Lateral thermal expansion of cellulose Iβ and IIII polymorphs. *Journal of Polymer Science Part B: Polymer Physics* **2002,** *40* (11), 1095-1102.

34. Bergenstråhle, M.; Berglund, L. A.; Mazeau, K., Thermal response in crystalline Iβ cellulose: a molecular dynamics study. *The Journal of Physical Chemistry B* **2007,** *111* (30), 9138-9145.

35. Morgan, J. L.; Strumillo, J.; Zimmer, J., Crystallographic snapshot of cellulose synthesis and membrane translocation. *Nature* **2013,** *493* (7431), 181-6.

36. Bi, Y. C.; Hubbard, C.; Purushotham, P.; Zimmer, J., Insights into the structure and function of membrane-integrated processive glycosyltransferases. *Curr Opin Struc Biol* **2015,** *34*, 78-86.

37. Lin, F. C.; Brown, R. M., Jr.; Drake, R. R., Jr.; Haley, B. E., Identification of the uridine 5'-diphosphoglucose (UDP-Glc) binding subunit of cellulose synthase in Acetobacter

xylinum using the photoaffinity probe 5-azido-UDP-Glc. *The Journal of biological chemistry* **1990,** *265* (9), 4782-4.

38. Brown, R. M., The Biosynthesis of Cellulose. *Journal of Macromolecular Science, Part A* **1996,** *33* (10), 1345-1373.

39. Kimura, S.; Laosinchai, W.; Itoh, T.; Cui, X.; Linder, C. R.; Brown, R. M., Jr., Immunogold labeling of rosette terminal cellulose-synthesizing complexes in the vascular plant vigna angularis. *Plant Cell* **1999,** *11* (11), 2075-86.

40. Brown, R. M.; Montezinos, D., Cellulose microfibrils: visualization of biosynthetic and orienting complexes in association with the plasma membrane. *Proceedings of the National Academy of Sciences* **1976,** *73* (1), 143-147.

41. Mueller, S. C.; Brown, R. M., Jr, Evidence for an intramembrane component associated with a cellulose microfibril-synthesizing complex in higher plants. *Journal of Cell Biology* **1980,** *84* (2), 315-326.

42. Vandavasi, V. G.; Putnam, D. K.; Zhang, Q.; Petridis, L.; Heller, W. T.; Nixon, B. T.; Haigler, C. H.; Kalluri, U.; Coates, L.; Langan, P.; Smith, J. C.; Meiler, J.; O'Neill, H., A Structural Study of CESA1 Catalytic Domain of Arabidopsis Cellulose Synthesis Complex: Evidence for CESA Trimers. *Plant Physiol* **2016,** *170* (1), 123-35.

43. Buschmann, H.; Borchers, A., Handedness in plant cell expansion: a mutant perspective on helical growth. *New Phytologist* **2020,** *225* (1), 53-69.

44. Jarvis, M. C., Cellulose biosynthesis: counting the chains. *Plant Physiol* **2013,** *163* (4), 1485-6.

45. Cosgrove, D. J., Growth of the plant cell wall. *Nat Rev Mol Cell Biol* **2005,** *6* (11), 850-61.

46. Fernandes, A. N.; Thomas, L. H.; Altaner, C. M.; Callow, P.; Forsyth, V. T.; Apperley, D. C.; Kennedy, C. J.; Jarvis, M. C., Nanostructure of cellulose microfibrils in spruce wood. *Proc Natl Acad Sci U S A* **2011,** *108* (47), E1195-203.

47. Thomas, L. H.; Forsyth, V. T.; Sturcova, A.; Kennedy, C. J.; May, R. P.; Altaner, C. M.; Apperley, D. C.; Wess, T. J.; Jarvis, M. C., Structure of cellulose microfibrils in primary cell walls from collenchyma. *Plant Physiol* **2013,** *161* (1), 465-76.

48. Newman, R. H.; Hill, S. J.; Harris, P. J., Wide-angle x-ray scattering and solid-state nuclear magnetic resonance data combined to test models for cellulose microfibrils in mung bean cell walls. *Plant Physiol* **2013,** *163* (4), 1558-67.

49. Oehme, D. P.; Downton, M. T.; Doblin, M. S.; Wagner, J.; Gidley, M. J.; Bacic, A., Unique Aspects of the Structure and Dynamics of Elementary Iβ Cellulose Microfibrils Revealed by Computational Simulations. *Plant Physiol.* **2015,** *168*, 3.

50. Nixon, B. T.; Mansouri, K.; Singh, A.; Du, J.; Davis, J. K.; Lee, J. G.; Slabaugh, E.; Vandavasi, V. G.; O'Neill, H.; Roberts, E. M.; Roberts, A. W.; Yingling, Y. G.; Haigler, C. H., Comparative Structural and Computational Analysis Supports Eighteen Cellulose Synthases in the Plant Cellulose Synthesis Complex. *Sci. Rep.* **2016,** *6*, 28696.

51. Phyo, P.; Wang, T.; Yang, Y.; O'Neill, H.; Hong, M., Direct determination of hydroxymethyl conformations of plant cell wall cellulose using 1H polarization transfer solid-state NMR. *Biomacromolecules* **2018,** *19* (5), 1485-1497.

52. Kubicki, J. D.; Yang, H.; Sawada, D.; O'Neill, H.; Oehme, D.; Cosgrove, D., The shape of native plant cellulose microfibrils. *Scientific reports* **2018,** *8* (1), 1-8.

53. Turbak, A. F.; Snyder, F. W.; Sandberg, K. R., *J. Appl. Polym. Sci.: Appl. Polym. Symp.* **1983,** *37*, 815.

54. Herrick, F. W.; Casebier, R. L.; Hamilton, J. K.; Sandberg, K. R. In *Microfibrillated cellulose: morphology and accessibility*, J. Appl. Polym. Sci.: Appl. Polym. Symp.;(United States), ITT Rayonier Inc., Shelton, WA: 1983.

55. Saito, T.; Nishiyama, Y.; Putaux, J. L.; Vignon, M.; Isogai, A., Homogeneous suspensions of individualized microfibrils from TEMPO-catalyzed oxidation of native cellulose. *Biomacromolecules* **2006,** *7* (6), 1687-91.

56. Wagberg, L.; Decher, G.; Norgren, M.; Lindstrom, T.; Ankerfors, M.; Axnas, K., The build-up of polyelectrolyte multilayers of microfibrillated cellulose and cationic polyelectrolytes. *Langmuir* **2008,** *24* (3), 784-95.

57. Noguchi, Y.; Homma, I.; Matsubara, Y., Complete nanofibrillation of cellulose prepared by phosphorylation. *Cellulose* **2017,** *24* (3), 1295-1305.

58. Paakko, M.; Ankerfors, M.; Kosonen, H.; Nykanen, A.; Ahola, S.; Osterberg, M.; Ruokolainen, J.; Laine, J.; Larsson, P. T.; Ikkala, O.; Lindstrom, T., Enzymatic hydrolysis

combined with mechanical shearing and high-pressure homogenization for nanoscale cellulose fibrils and strong gels. *Biomacromolecules* **2007,** *8* (6), 1934-41.

59. Henriksson, M.; Henriksson, G.; Berglund, L. A.; Lindstrom, T., An environmentally friendly method for enzyme-assisted preparation of microfibrillated cellulose (MFC) nanofibers. *Eur Polym J* **2007,** *43* (8), 3434-3441.

60. De Nooy, A. E.; Besemer, A. C.; van Bekkum, H., On the use of stable organic nitroxyl radicals for the oxidation of primary and secondary alcohols. *Synthesis* **1996,** *1996* (10), 1153-1176.

61. Saito, T.; Hirota, M.; Tamura, N.; Kimura, S.; Fukuzumi, H.; Heux, L.; Isogai, A., Individualization of nano-sized plant cellulose fibrils by direct surface carboxylation using TEMPO catalyst under neutral conditions. *Biomacromolecules* **2009,** *10* (7), 1992-6.

62. Saito, T.; Isogai, A., Introduction of aldehyde groups on surfaces of native cellulose fibers by TEMPO-mediated oxidation. *Colloids and Surfaces a-Physicochemical and Engineering Aspects* **2006,** *289* (1-3), 219-225.

63. Okita, Y.; Saito, T.; Isogai, A., Entire surface oxidation of various cellulose microfibrils by TEMPO-mediated oxidation. *Biomacromolecules* **2010,** *11*, 1696.

64. Tanaka, R.; Saito, T.; Hanninen, T.; Ono, Y.; Hakalahti, M.; Tammelin, T.; Isogai, A., Viscoelastic Properties of Core-Shell-Structured, Hemicellulose-Rich Nanofibrillated Cellulose in Dispersion and Wet-Film States. *Biomacromolecules* **2016,** *17* (6), 2104-11.

65. Tanaka, R.; Saito, T.; Hondo, H.; Isogai, A., Influence of Flexibility and Dimensions of Nanocelluloses on the Flow Properties of Their Aqueous Dispersions. *Biomacromolecules* **2015,** *16* (7), 2127-31.

66. Shimizu, M.; Saito, T.; Isogai, A., Water-resistant and high oxygen-barrier nanocellulose films with interfibrillar cross-linkages formed through multivalent metal ions. *Journal of Membrane Science* **2016,** *500*, 1-7.

67. Shimizu, M.; Saito, T.; Fukuzumi, H.; Isogai, A., Hydrophobic, ductile, and transparent nanocellulose films with quaternary alkylammonium carboxylates on nanofibril surfaces. *Biomacromolecules* **2014,** *15* (11), 4320-5.

68. Fujisawa, S.; Saito, T.; Kimura, S.; Iwata, T.; Isogai, A., Surface engineering of ultrafine cellulose nanofibrils toward polymer nanocomposite materials. *Biomacromolecules* **2013,** *14* (5), 1541-6.

69. Kubo, R.; Saito, T.; Isogai, A., Dual Counterion Systems of Carboxylated Nanocellulose Films with Tunable Mechanical, Hydrophilic, and Gas-Barrier Properties. *Biomacromolecules* **2019,** *20* (4), 1691-1698.

70. Soeta, H.; Fujisawa, S.; Saito, T.; Isogai, A., Interfacial layer thickness design for exploiting the reinforcement potential of nanocellulose in cellulose triacetate matrix. *Composites Science and Technology* **2017,** *147*, 100-106.

71. Shimizu, M.; Saito, T.; Isogai, A., Bulky quaternary alkylammonium counterions enhance the nanodispersibility of 2,2,6,6-tetramethylpiperidine-1-oxyl-oxidized cellulose in diverse solvents. *Biomacromolecules* **2014,** *15* (5), 1904-9.

72. Saito, T.; Kuramae, R.; Wohlert, J.; Berglund, L. A.; Isogai, A., An Ultrastrong Nanofibrillar Biomaterial: The Strength of Single Cellulose Nanofibrils Revealed via Sonication-Induced Fragmentation. *Biomacromolecules* **2013,** *14*, 248.

73. Lahiji, R. R.; Xu, X.; Reifenberger, R.; Raman, A.; Rudie, A.; Moon, R. J., Atomic force microscopy characterization of cellulose nanocrystals. *Langmuir* **2010,** *26* (6), 4480-8.

74. Iwamoto, S.; Kai, W.; Isogai, A.; Iwata, T., Elastic modulus of single cellulose microfibrils from tunicate measured by atomic force microscopy. *Biomacromolecules* **2009,** *10* (9), 2571-6.

75. Hori, R.; Wada, M., The thermal expansion of wood cellulose crystals. *Cellulose* **2005,** *12* (5), 479-484.

76. Nishino, T.; Matsuda, I.; Hirao, K., *Macromolecules* **2004,** *37*, 7683.

77. Uetani, K.; Okada, T.; Oyama, H. T., Crystallite Size Effect on Thermal Conductive Properties of Nonwoven Nanocellulose Sheets. *Biomacromolecules* **2015,** *16* (7), 2220-7.

78. Fukuzumi, H.; Saito, T.; Iwata, T.; Kumamoto, Y.; Isogai, A., Transparent and High Gas Barrier Films of Cellulose Nanofibers Prepared by TEMPO-Mediated Oxidation. *Biomacromolecules* **2009,** *10*, 162.

79. Saito, T.; Uematsu, T.; Kimura, S.; Enomae, T.; Isogai, A., Self-aligned integration of native cellulose nanofibrils towards producing diverse bulk materials. *Soft Matter* **2011,** *7* (19), 8804-8809.

80. Zhao, M.; Ansari, F.; Takeuchi, M.; Shimizu, M.; Saito, T.; Berglund, L.; Isogai, A., Nematic structuring of transparent and multifunctional nanocellulose papers. *Nanoscale Horizons* **2018,** *3* (1), 28-34.

81. Kobayashi, Y.; Saito, T.; Isogai, A., Aerogels with 3D ordered nanofiber skeletons of liquid-crystalline nanocellulose derivatives as tough and transparent insulators. *Angew Chem Int Ed Engl* **2014,** *53* (39), 10394-7.

82. Yamasaki, S.; Sakuma, W.; Yasui, H.; Daicho, K.; Saito, T.; Fujisawa, S.; Isogai, A.; Kanamori, K., Nanocellulose Xerogels With High Porosities and Large Specific Surface Areas. *Front Chem* **2019,** *7*, 316.

83. Fukui, S.; Ito, T.; Saito, T.; Noguchi, T.; Isogai, A., Counterion Design of TEMPO-Nanocellulose used as Filler to Improve Properties of Hydrogenated Acrylonitrile-Butadiene Matrix. *Compos. Sci. Technol.* **2018,** *167*, 339.

84. Inui, T.; Koga, H.; Nogi, M.; Komoda, N.; Suganuma, K., A miniaturized flexible antenna printed on a high dielectric constant nanopaper composite. *Adv Mater* **2015,** *27* (6), 1112-6.

85. Fujisawa, S., Material design of nanocellulose/polymer composites via Pickering emulsion templating. *Polymer Journal* **2020**, 1-7.

Chapter 2
Dispersion-Induced Disordering of the Grain Boundary in Biologically Structured Cellulose

2.1 Abstract

In trees, a-few-nanometers-wide crystalline fibrils of cellulose are tightly bundled with other biopolymers, such as lignin and hemicelluloses, to form robust cell walls. Cellulose nanofibers (CNFs) are obtained by successive treatments including the purification, modification, and disintegration of cell-wall cellulose. This chapter reports that the crystallinity of CNFs is governed by the interface between the bundled cellulose fibrils. The cellulose molecules at the interface or at the surface of the individual fibrils are ordered when the fibrils are more densely bundled upon removal of hemicelluloses. In turn, the interfacial molecules become disordered when bundled fibrils disperse upon disintegration as CNFs. Morphological analysis of the dispersed fibrils supports a model where single-cellulose fibrils in trees are composed of 18 molecular chains. Considering the 18-chain model, the surface molecules of the dispersed fibrils are disordered in the conformation of carbon atoms as analyzed by NMR, while all of the 18 chains are fully ordered in molecular sheet stacking to diffract X-rays.

2.2 Introduction

Cellulose nanofibers (CNFs) are attracting attention as wood-derived new material, combining high-performance biobased materials combining high strength[1, 2], high stiffness[3, 4], low thermal expansion[5, 6], and high dielectric properties[7]. These excellent properties of CNFs are based on the molecular packing of cellulose in the microfibrils or the uniaxial molecular orientation and high crystallinity, as described in general introduction. In particular, the crystallinity of CNFs is a variable structural factor that is responsible for their material performance.

According to the International Union of Pure and Applied Chemistry (IUPAC), crystallinity is defined as the presence of three-dimensional order at the level of the atomic dimensions. The crystallinity of a material is expressed as the crystallinity index (CI), which is

the mass ratio of the crystalline substance in the total dry sample on the basis of the crystallographic two-phase model. Although synthetic polymers crystallize from their melt or solution states in thermodynamic equilibria, cellulose is created by an enzyme complex by biological machinery and crystallizes with uniaxial molecular orientation[8, 9]. Accordingly, there is no clear boundary between the crystalline and noncrystalline phases in naturally occurring cellulosic structures. It is thus difficult to determine their CI values. The CI value of celluloses is often evaluated by solid-state CP/MAS ^{13}C NMR spectroscopy or X-ray diffraction (XRD). However, the CI values of cellulosic materials greatly vary depending on the measurement technique and analytical processing[10-24]. The purity and morphology also affect the CI values[15, 25, 26]. Therefore, CI evaluation of CNFs with structural variety in the chemical composition and morphology is difficult, and it is still not defined in a single uniform way.

In this chapter, it is reported that the crystallinity of CNFs is governed by the interface between bundled cellulose microfibrils. Specifically, the cellulose molecules at the interface or at the surface of the individual microfibrils are partly crystalline and become disordered when the microfibrils disperse as CNFs. The CI values of approximately 20 samples ranging from a wood pulp to CNFs were measured by NMR and XRD techniques. The rationality of the resulting CI values is discussed in terms of the cellulose content, specific surface area (SSA), crystal size, and nanofiber width. The CNF samples were prepared by the TEMPO oxidation process. Before analysis, all of the pulp and CNF samples were freeze-dried from an undried wet state containing approximately 30% *tert*-butyl alcohol to prevent dry agglomeration[27]. All of the samples prepared in the present study are listed in Table 2.1. Hereafter, each sample is referred to by the corresponding sample number in Table 2.1; *e.g.*, sample 5 is the dewaxed pulp. Scheme 2.1 illustrates nanostructural changes occurring in the samples by chemical purification, surface modification, and mechanical disintegration.

Table 2.1. List of the cellulosic samples.

Number	Sample
1	acid-hydrolyzed tunicate cellulose
2	acid-hydrolyzed cotton cellulose
3	acid-hydrolyzed wood cellulose
4	amorphous cellulose
5	dewaxed pulp
6	delignified pulp
7	hemicellulose-extracted pulp
8	sample 7 mechanically treated for 80 min*
9	TEMPO-oxidized pulp with NaClO addition of 5 mmol/g
10	CNFs, sample 9 mechanically treated for 5 min*
11	CNFs, sample 9 mechanically treated for 20 min*
12	CNFs, sample 9 mechanically treated for 40 min*
13	CNFs, sample 9 mechanically treated for 80 min*
14	CNFs, sample 9 treated with a high-pressure homogenizer
15	TEMPO-oxidized pulp with NaClO addition of 10 mmol/g
16	CNFs, sample 15 mechanically treated for 5 min*
17	CNFs, sample 15 mechanically treated for 20 min*
18	CNFs, sample 15 mechanically treated for 40 min*
19	CNFs, sample 15 mechanically treated for 80 min*
20	CNFs, sample 15 treated with a high-pressure homogenizer
21	CNFs, sample 15 treated with a magnetic stirrer

*Treated with a double-cylinder-type mechanical homogenizer.

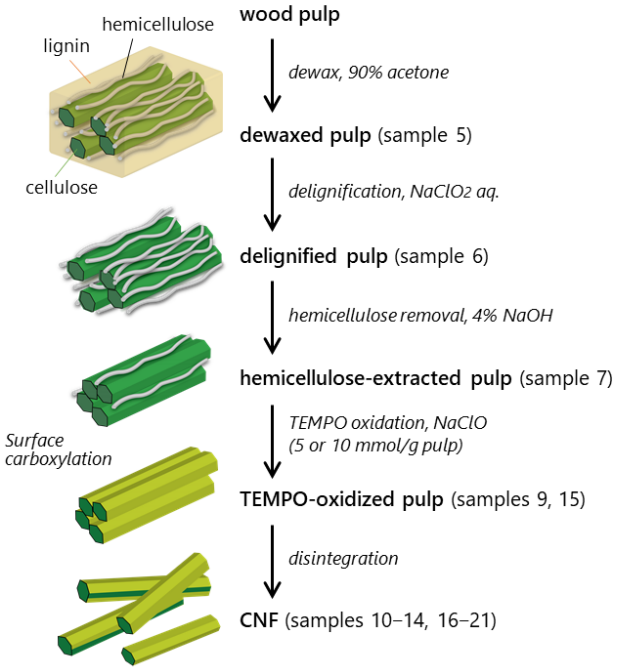

Scheme 2.1. Nanostructural changes occurring in a series of the samples from a wood pulp to CNFs.

2.3 Experimental section

2.3.1 Materials

A refiner mechanical softwood pulp maintained in an undried state after pulping (Nippon Paper Industries, Japan) was used as the starting sample. The pulp was a mixture of several softwood species and produced mainly from the chips of *Cryptomeria japonica* and *Pinus densiflora*. An ash-less filter pulp (Advantec Toyo, Japan) was used as the cotton sample. Tunicate cellulose was purified from mantles of *Halocynthia roretzi* by alternating treatment with NaOH and $NaClO_2$. The preparation of acid hydrolysates and amorphous cellulose (samples 1–4). All the chemicals were of laboratory grade (FUJIFILM Wako Pure Chemical Corporation, Osaka, Japan) and used as received.

2.3.2 Purification

The refiner mechanical pulp (10 g by dry weight) was dewaxed with a 90% (w/w) acetone solution (1 L) for 1 day under ambient conditions, followed by filtration and washing with a 90% (w/w) acetone solution and an excess amount of distilled water (sample 5). The

dewaxed pulp (5 g by dry weight) was delignified with a $NaClO_2$ (2 g) solution (300 mL) containing acetic acid (0.4 mL) at 75 °C for 1 h, followed by filtration. This $NaClO_2$ treatment was repeated three times using fresh chemicals, followed by washing with distilled water (sample 6). The delignified pulp (20 g by dry weight) was treated with a 4% (w/v) NaOH solution (1 L) under ambient conditions for 1 h with bubbling nitrogen gas, followed by filtration and washing. The NaOH treatment was repeated one more time (sample 7). At each purification step, part of the washed pulp was freeze-dried after the addition of approximately 30% (w/w) *tert*-butanol with respect to its water content[27], and conditioned at 23 °C and 50% relative humidity for more than 1 day.

2.3.3 TEMPO-mediated oxidation

The NaOH-treated pulp in the undried state (sample 7; 2 g by dry weight) was TEMPO-oxidized with the NaClO addition of 5 or 10 mmol/g of pulp according to a previously reported method.[28] The oxidized pulps were treated with $NaBH_4$ (0.2 g) in water (200 mL) at pH 10 for 3 h to eliminate unstable aldehyde groups in the pulp (samples 9 and 15). The carboxylate contents of the resulting pulps with the NaClO addition of 5 and 10 mmol/g were determined to be 0.8 and 1.4 mmol/g, respectively, by conductivity titration. Parts of the oxidized pulps were freeze-dried and conditioned in the same manner as that for the purified pulps.

2.3.4 Preparation of acid-hydrolyzed cellulose

The cellulose samples (0.1 g) were treated with 1 M H_2SO_4 solution at 105 °C for 4 h. The residual solid hydrolysate was thoroughly washed with distilled water by filtration, freeze-dried, and conditioned in the same manner as for the purified pulps.

2.3.5 Preparation of amorphous cellulose

High-purity fibrillated softwood cellulose (Celish, Daicel FineChem Ltd., Japan) (0.02 g) was suspended in ethylenediamine (5 mL) at room temperature for 4 days. The sample was centrifuged at 12,000 g for 10 min, and the sediment was then suspended in methanol (35 mL). This methanol-rinsing process was repeated three times. The final methanol suspension was stirred for 3 h and then centrifuged. The sediment was suspended in *N*,*N*-dimethylacetamide (DMAc) (35 mL), followed by centrifugation. After repeating the DMAc-rinsing process three times, the final DMAc suspension was stirred overnight. The sample was collected by

centrifugation and dissolved in 8% LiCl/DMAc solution with stirring at room temperature for a week. The resulting cellulose solution was passed through a polytetrafluoroethylene membrane with a mean pore size 0.45 μm, and the filtrate was injected into an excess amount of distilled water to regenerate amorphous cellulose. The regenerated cellulose was thoroughly washed with distilled water.

2.3.6 Cellulose content

The cellulose contents of the pulps were calculated from the sample weights by subtracting the lignin and hemicellulose contents. The lignin contents of the dewaxed pulps were determined by the Klason lignin method as the sums of the acid-soluble and -insoluble lignin contents. The acid-soluble lignin contents were measured according to TAPPI standard method T 222 om-98, and the residual lignin was then collected by filtration after sulfuric acid hydrolysis of the carbohydrates in the pulp according to TAPPI standard method T 222 om-02. The residual lignin was dissolved in a 3% sulfuric acid solution, and light absorbance measurement was performed at 280 nm using a Jasco V-670 spectrophotometer. The lignin contents of the other pulps were determined from their Kappa numbers by multiplying by 0.15 according to the TAPPI classical method T 236 cm-85. The hemicellulose contents were determined by neutral sugar composition analysis according to a previously reported method.[29] In brief, the pulps (0.05 g) were acid-hydrolyzed in two steps with 72% and 3% sulfuric acid solutions. Myo-inositol (20 mg/mL) was then added to the resulting hydrolysates as the internal standard. $BaSO_4$ precipitates were then formed by adding $Ba(OH)_2$ (1.7 g) and $BaCO_3$ powders until the pH reached 5.5–6.5. The supernatants were separated by centrifugation, followed by filtration and freeze-drying. The dried hydrolysates were dissolved in distilled water (0.5 mL) and then mixed with acetonitrile (0.5 mL). After sonication for 10 min, the mixtures (∼1 mL) were passed through a poly(tetrafluoroethylene) membrane filter with a mean pore size of 0.45 μm. The filtrates were analyzed by a high-performance liquid chromatography system equipped with a Shodex Asahipak NH2P-50-4E column and a Wyatt Technology Optilab T-rEx interferometric refractometer (k = 658 nm). A 75% (v/v) acetonitrile/water mixture containing 250 mM H_3PO_4 was used as the eluent, and the flow rate and temperature were set to 1.0 mL/min and 50 °C, respectively.

2.3.7 Fibrillation

The TEMPO-oxidized pulps in the undried state (samples 9 and 15; 0.3 g by dry weight) were suspended in distilled water (300 mL), and the suspensions were then treated with a Physcotron NS-56 mechanical homogenizer equipped with a 20-mm-diameter shaft at 7500 rpm for up to 80 min. At treatment times of 5, 20, 40, and 80 min, samples of the resulting CNF dispersions (50 mL at each point) were taken (samples 10–13 and 16–19). Parts of the oxidized pulps were disintegrated by passing the suspensions (0.2%, 1 L) through a high-pressure water jet system (HJP-25001, Sugino Machine) at 150 MPa (samples 14 and 20) or by gently stirring the suspensions (0.1%, 1 L) with a magnetic rotator at 500 rpm for 20 days (sample 21).

2.3.8 CP/MAS ^{13}C NMR spectroscopy

The conditioned samples with moisture contents of approximately 10% (~0.1 g) were packed into airtight tubes and analyzed by CP/MAS ^{13}C NMR spectroscopy. The CP/MAS ^{13}C NMR measurements were performed with a JEOL JNM-ECAII 500 spectrometer equipped with a 3.2 mm HXMAS probe and ZrO_2 rotors at 125.77 MHz. The 90° proton decoupler pulse width, contact time, relaxation delay, and spinning frequency were set to 2.5 μs, 2 ms, 5 s, and 6 kHz, respectively. Note here that the 2 ms of contact time is optimized parameter for calculating the NMR-based CI value (see Appendix for the detail of the optimization). Adamantane was used as the internal standard for the ^{13}C chemical shifts.

2.3.9 XRD

The conditioned samples were pressed at approximately 750 MPa for 1 min using a tableting device for XRD. The resulting discotic pellets had bulk densities of approximately 1.3 g/cm^3. XRD measurements were performed at 23 °C under ambient pressure in the diffraction angle 2θ range 5–45° using a Rigaku RINT 2000 diffractometer with Ni-filtered Cu Kα radiation (λ = 0.15418 nm) at 40 kV and 40 mA by the reflection method. Although the measurements were not under humidity control, the moisture contents of the pellets (~10%) were nearly unchanged (±0.2%) after the measurements.

2.3.10 SSA

SSA values were calculated from the nitrogen adsorption–desorption isotherms based on Brunauer–Emmett–Teller theory. The isotherms were determined with a Quantachrome NOVA 4200e system at −196 °C after degassing the samples in the system at 105 °C for 20 h.

2.3.11 Turbidity

Turbidity curves of 0.1% (w/w) CNF dispersions were measured using poly(methyl methacrylate) cuvettes with a 1 cm path length in the wavelength range 280–900 nm using a Jasco V-670 spectrophotometer under ambient conditions with distilled water as a reference. The weighted average widths of dispersed CNFs were estimated from their turbidity curves according to a previously reported method[30].

2.3.12 AFM analysis

CNF dispersions were diluted to 0.0005% (w/w) with distilled water, dropped onto a mica plate, and dried in a desiccator under ambient conditions. AFM observation was performed using a Bruker MultiMode 8 microscope equipped with a NanoScope V controller and a ScanAsyst-Air probe with a low spring constant of 0.4 N/m and a tip diameter of 2 nm in peak-force tapping mode with monitoring to ensure that the repulsion time was approximately 10%. The heights of approximately 50 CNFs were measured for each CNF sample.

2.3.13 True density

True density values were measured using a MicrotracBEL helium pycnometer (BELPycno). The freeze-dried sample (~60 mg) was placed in the chamber with a volume of 1 cm^3 and heated at 105 °C for 3 h under vacuum. Then, helium gas was purged 30 times at 145 kPa. A density value was measured at 25 ± 0.1 °C when no change of over 0.06 kPa for 30 s was observed. The measurement was repeated until a standard deviation of less than 1% for consecutive 30 measurements was achieved, and finally the average value of the last three measurements was taken as the true density value of the corresponding sample.

2.4 Results and discussion

2.4.1 CI measurements

The NMR-based CI values (CI-NA) were calculated from the area ratio of the two signals centered at 88.8 and 84 ppm, which correspond to the crystalline and noncrystalline C4 carbon atoms of cellulose, respectively (Figure 2.1.a)[25, 31].

Peak separation of the signals was performed using pseudo-Voigt functions in the order of 71.9 and 74.8 ppm (C2, C3, and C5), 105 ppm (C1), 88.8 ppm (crystalline C4), 84 ppm (noncrystalline C4), and 65.2, 62.5, and 60.6 ppm (C6) to maximize the peak height and width of each signal. This peak separation order limits the degree of freedom by the analyst and results in fitting with the highest average correlation coefficient R^2 (see Figure 2.2 for the fitting results).

The XRD-based CI values were obtained by comparing either the intensities (CI-XI) or areas (CI-XA) of the powder XRD peaks of pelletized samples. The CI-XI value is the ratio of the maximum intensity at 2θ of around 22.6° to the minimum intensity between the (2 0 0) and (1 1 0) peaks at around 18.5° (λ = 0.1548 nm; Figure 2.1b). The CI-XA value is the ratio of the sum of the crystalline peak areas to the total area, assuming broad peaklike noncrystalline scattering centered at 20.6° (Figure 2.1c). The peak shape of the noncrystalline scattering was determined by maximizing both its height and full width at half-maximum before separating the crystalline diffraction peaks. The center positions of the noncrystalline (20.6°) and crystalline (14.6, 16.4, 22.6, and 34.5°) peaks were determined from the XRD profiles of an amorphous cellulose (sample 4) and an acid-hydrolyzed tunicate cellulose (sample 1), respectively (Figure 2.1d). Peak fitting of the XRD profiles was performed using pseudo-Voigt functions, where the (1 0 2) and (0 1 2) diffractions at approximately 20–21° were not taken into account, assuming that these two diffractions would be sufficiently small for pelletized samples with the preferred orientation of the crystallites[22]. The XRD profiles include a variety of scatterings by atoms and glucose units of cellulose and by air molecules and moisture (bound water), which are irrespective of the crystallinity of the samples. It is thus desirable to eliminate such scattering contributions from the XRD profile as the background[19, 32]. To experimentally determine the background function, four cellulose samples with different crystallinities, or three

acid hydrolysates of tunicate, cotton, and wood celluloses and an amorphous cellulose (samples 1–4), were subjected to XRD measurement (Figure 2.1d). The intensities at both ends of the XRD profiles from 8° to 45° are nearly the same for all of the samples with different crystallinities. Therefore, a straight line connecting the two points at 8° and 45° was used as the background function. Both CI-XI and CI-XA values were calculated from the XRD profiles after subtracting the linear background.

The crystal sizes of the (2 0 0) plane were also calculated from the XRD profiles using Scherrer's equation (shape factor $K = 0.9$)[33, 34]. It should be noted that the Scherrer dimension is a weighted mean column length, and it is perpendicular to the (2 0 0) plane[34]. The (2 0 0) diffraction peak was separated by one of the following two processes: (1) the peak was fitted to the profile after subtracting the linear background and without assuming broad peaklike noncrystalline scattering centered at 20.6° (Figure 2.1b); (2) the peak was fitted after subtracting both the linear background and noncrystalline scattering in the same manner as that for the CI-XA calculation (Figures 2.1c and 2.2 and 2,3). Hereafter, the crystal sizes calculated by processes 1 and 2 are thus referred to as CS-I and CS-A, respectively. Note also that the CS values constitute a lower limit of the crystallite dimension because the peak broadening due to disorder and instrumental factors was not taken into account in the present study[34, 35].

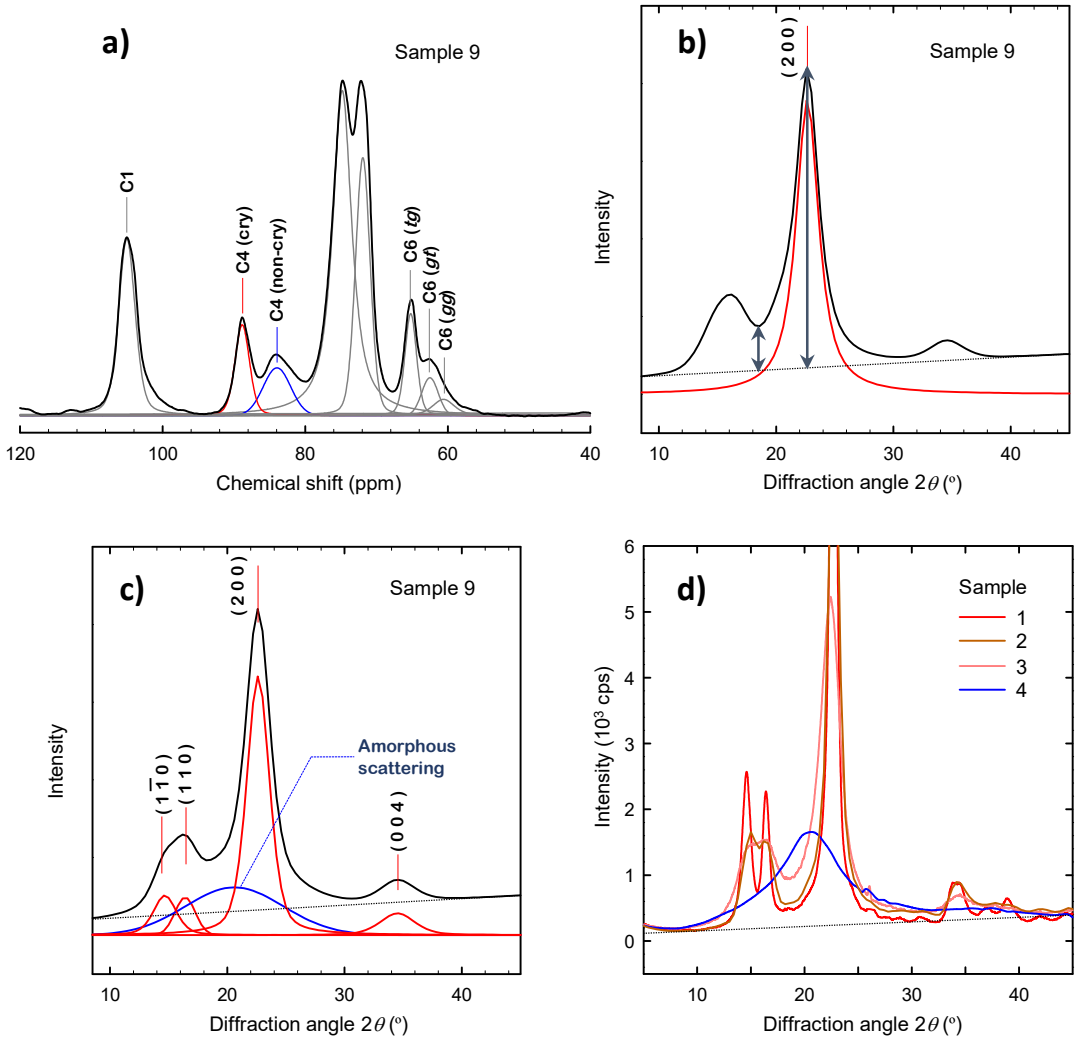

Figure 2.1. CI measurements. a) Peak deconvolution of a CP/MAS ^{13}C NMR spectrum for the C4-based CI-NA and C6 conformation analyses. The black line is the experimental spectrum, and the red, blue, and gray lines show peak separation of the corresponding carbon atoms using pseudo-Voigt functions. b) Intensity analysis and peak separation of an XRD profile for determination of the CI-XI and CS-I values, respectively. c) Peak separation of a XRD profile for determination of the CI-XA and CS-A values. In parts b and c, the black line is the experimental data, the red and blue lines show the separated peaks, and the gray line shows the background. d) XRD profiles of cellulosic samples with different crystallinities for background determination. The gray straight line shows the background. (sample 9: TEMPO-oxidized pulp with NaClO addition of 5 mmol/g, sample 1: acid-hydrolyzed tunicate cellulose, sample 2: acid-hydrolyzed cotton cellulose, sample 3: acid-hydrolyzed wood cellulose, sample 4: amorphous cellulose.)

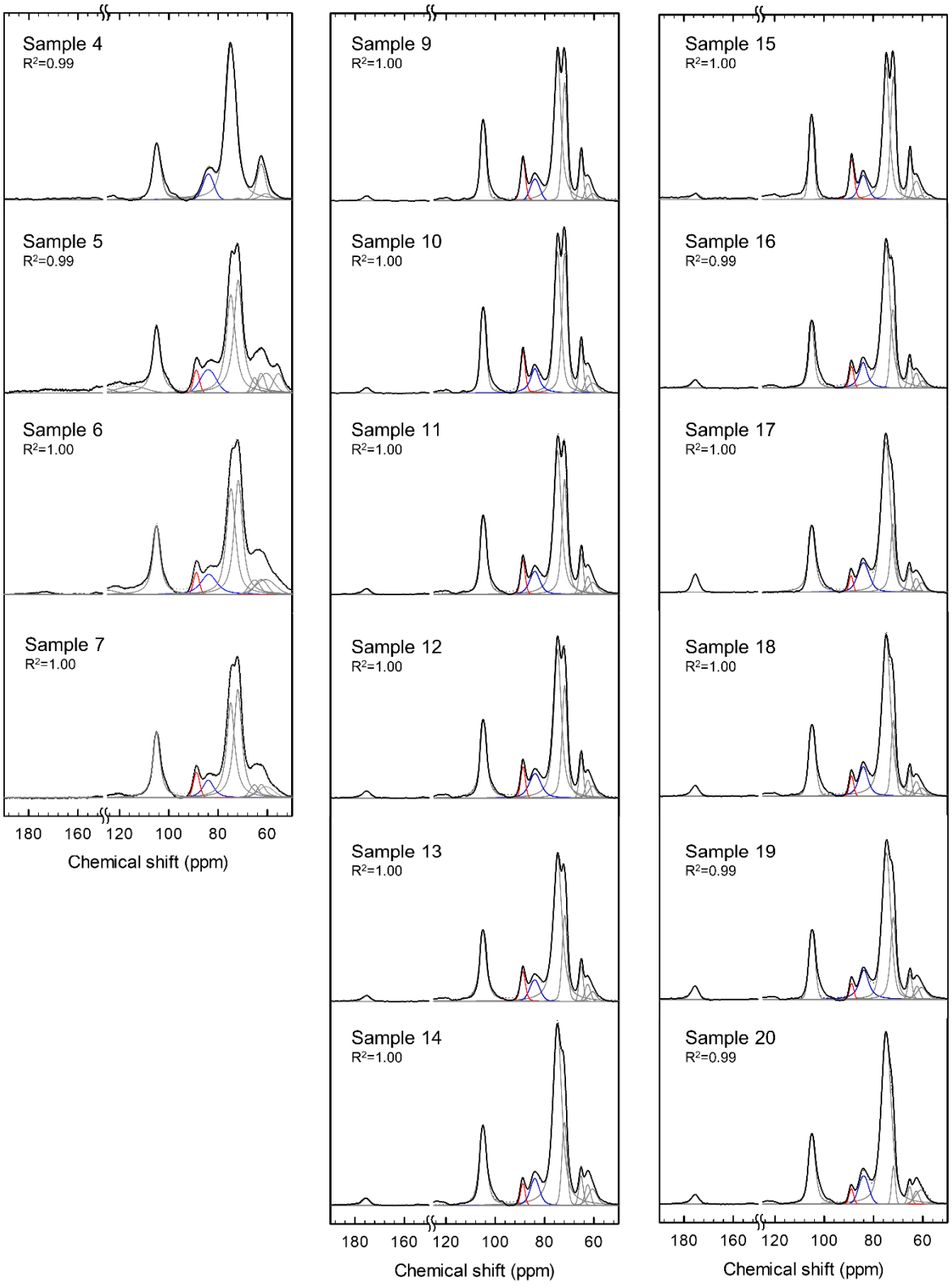

Figure 2.2. Peak deconvolution of the CP/MAS ^{13}C NMR spectra. The black lines are the experimental spectra, the red, blue, and gray lines are the separated peaks of the corresponding carbon atoms, and the dotted lines, which almost overlap with the black lines, are the fitting results. (sample 4: amorphous cellulose, sample 5: dewaxed pulp, sample 6:

delignified pulp, sample 7: hemicellulose-extracted pulp, sample 9: TEMPO-oxidized pulp with NaClO addition of 5 mmol/g, sample 10–13: CNFs; sample 9 mechanically treated for 5–80 min, respectively, sample 14: CNFs; sample 9 treated with a high-pressure homogenizer, ,sample 15: TEMPO-oxidized pulp with NaClO addition of 10 mmol/g, sample 16–20: CNFs; sample 15 mechanically treated for 5–80 min with the double-cylinder-type mechanical homogenizer and with the high-pressure homogenizer, respectively.)

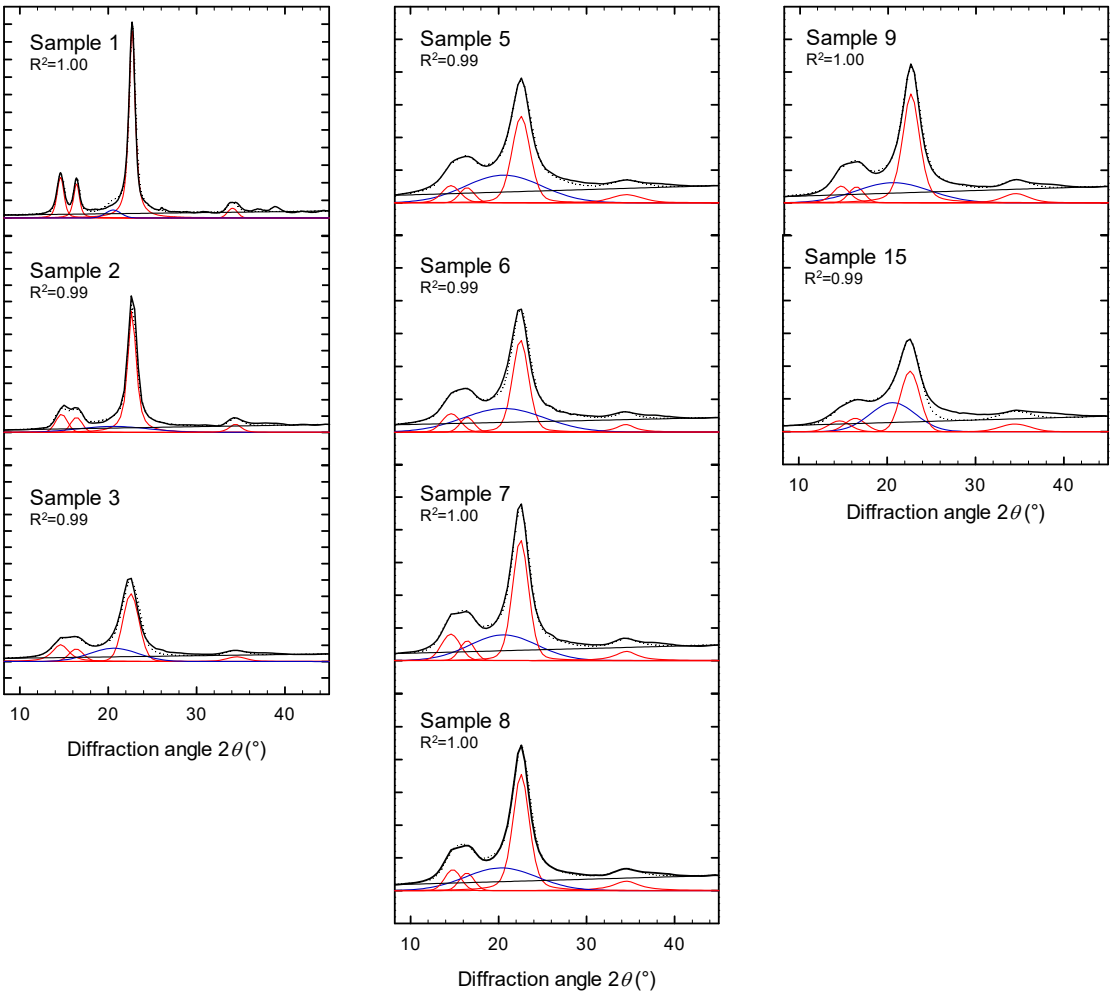

Figure 2.3. Background subtraction and peak separation of the XRD profiles from the pulp samples. The curved and straight lines in black are the experimental data and background, respectively, and the blue and red lines are the separated peaks of amorphous scattering and crystalline diffraction. The dotted lines are the fitting results. The intervals of the vertical axis for the intensity are 1,000 cps. (sample 1: acid-hydrolyzed tunicate cellulose, sample 2: acid-hydrolyzed cotton cellulose, sample 3: acid-hydrolyzed wood, sample 5: dewaxed pulp, sample 6: delignified pulp, sample 7: hemicellulose-extracted pulp, sample 8: sample 7 mechanically treated for 80 min, sample 9 and 15: TEMPO-oxidized pulp samples with carboxylate contents of 0.8 and 1.4, respectively.)

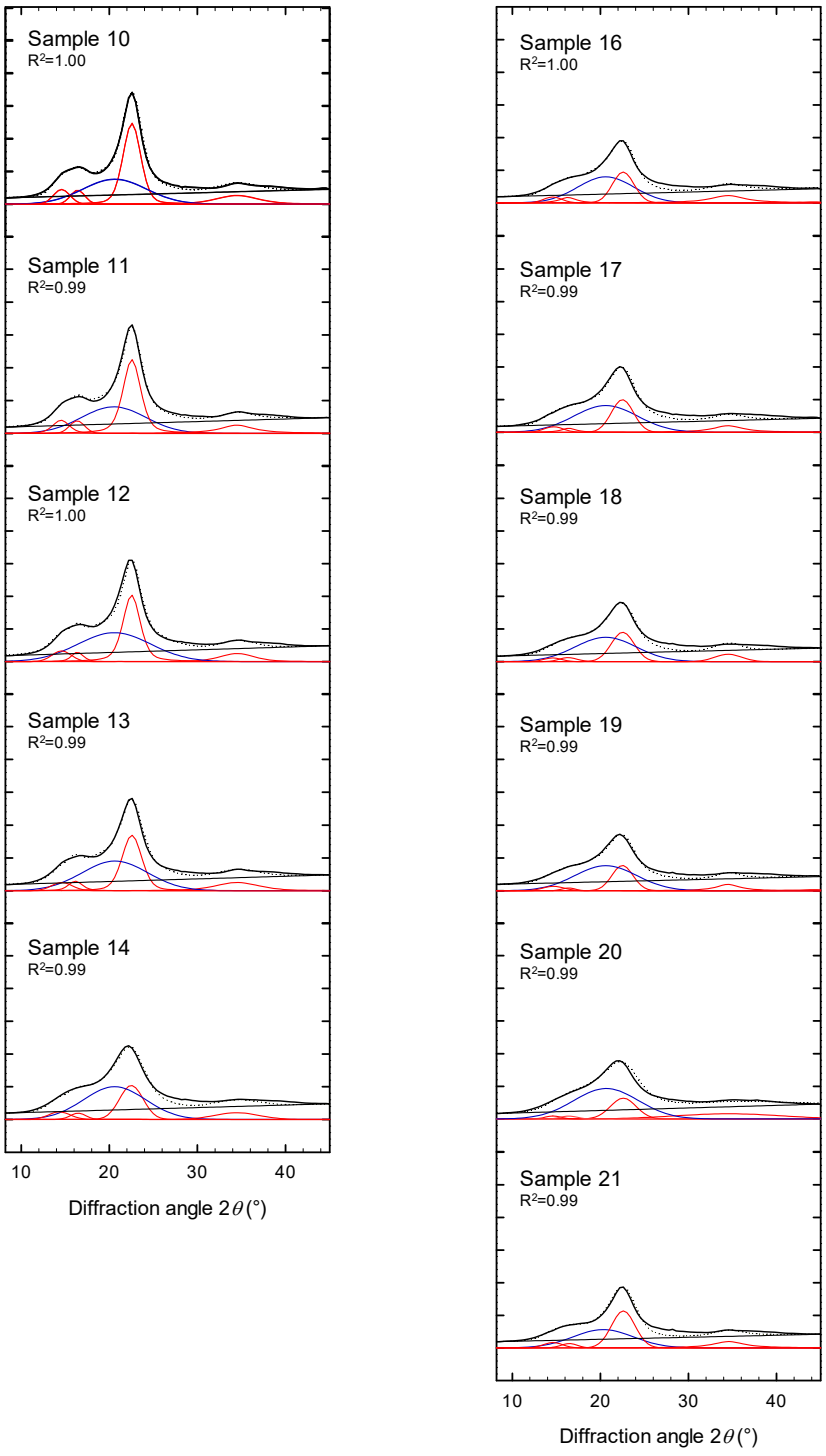

Figure 2.4. Background subtraction and peak separation of the XRD profiles from the CNF samples. The profiles are analyzed in the same way as shown in Figure 2.3.(sample 10–14: CNF samples with carboxylate contents of 0.8 mmol/g mechanically treated for 5–80 min with the double-cylinder-type mechanical homogenizer and with the high-pressure homogenizer, respectively, sample 16–20: CNF samples with carboxylate contents of 1.4 mechanically treated for 5–80 min with the double-cylinder-type mechanical homogenizer, with the high-pressure homogenizer, and with a magnetic stirrer, respectively.)

2.4.2 Cellulose content *vs.* CI value

Cellulose is a crystalline component, whereas lignin and hemicelluloses are amorphous. Thus, the cellulose content is an indication of the CI of wood-derived cellulosic materials.[15] Figure 2.5 shows the relationships between the cellulose contents and the CI values of wood pulps purified in a stepwise manner (see Figure 2.6 for other composition analyses). Most of the lignin in the starting pulp (sample 5) was removed by bleaching treatment, resulting in an approximately 15% increase in the cellulose content (sample 6). The residual lignin and part of the hemicelluloses were then removed by alkaline treatment using a 4% NaOH solution, and the cellulose content increased by approximately 10% (sample 7). The residual hemicelluloses that were insoluble in a 4% NaOH solution were removed by TEMPO oxidation, and the cellulose content finally increased to approximately 99% (samples 9 and 15).

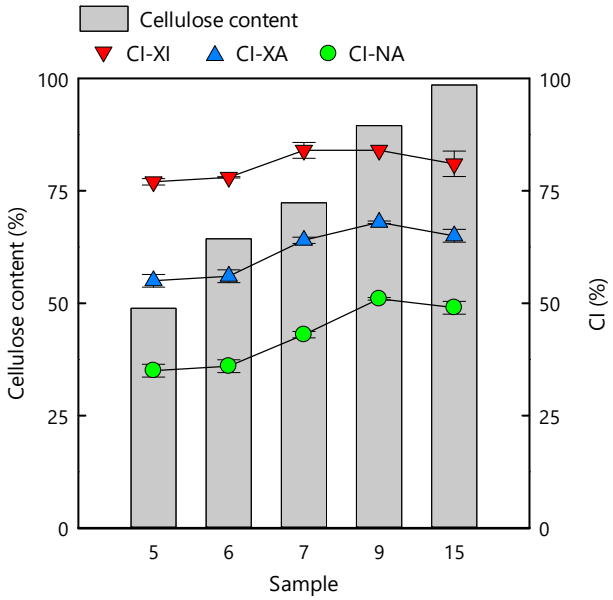

Figure 2.5. Relationships between the CI values of the purified pulps and the cellulose content. The standard deviations are calculated from three measurements for each CI value. (sample 5: dewaxed pulp, sample 6: delignified pulp, sample 7: hemicellulose-extracted pulp, sample 9 and 15: TEMPO-oxidized pulp samples with carboxylate contents of 0.8 and 1.4, respectively)

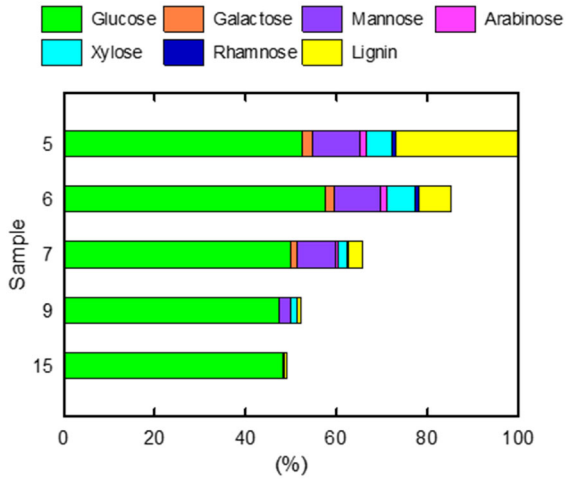

Figure 2.6. Chemical compositions of the pulp samples. (sample 5: dewaxed pulp, sample 6: delignified pulp, sample 7: hemicellulose-extracted pulp, sample 9 and 15: TEMPO-oxidized pulp samples with carboxylate contents of 0.8 and 1.4, respectively.)

Although the CI values show apparently similar trends, their absolute values are substantially different and they are in the order CI-XI > CI-XA > CI-NA. The CI-NA values of the dewaxed and delignified pulps (samples 5 and 6) are almost the same, even though the cellulose contents are approximately 15% different. However, this result is reasonable because the NMR signals due to lignin appear at different positions (120 and 55 ppm) and are not part of the C4 region used in the CI-NA calculation (79–92 ppm). Then, the CI-NA values proportionally increase with increasing cellulose content by alkali treatment and subsequent TEMPO oxidation (samples 7 and 9). This is because one of the NMR signals of the major hemicelluloses, such as xylan and glucomannan, appears at approximately 82 ppm, which overlaps with the signal of the noncrystalline C4 carbon atoms[25, 36, 37]. In fact, the CI-NA value can reflect the extent of hemicellulose removal. Meanwhile, the XRD-based CI values show a relatively weak dependence on the cellulose content: (1) some of the XRD-based CI values are higher than the corresponding cellulose contents; (2) it is not clear why the XRD-based CI values are nearly unchanged after delignification (samples 5 and 6); (3) the CI-XI values are also unchanged after the large increase in the cellulose content by TEMPO oxidation with the NaClO addition of 5 mmol/g (samples 7 and 9). These three points on the XRD-based CI values will be interpreted in the latter part of this paper. Note that all of the CI values for sample 15 are slightly less than those for sample 9 even though the cellulose

content increases by approximately 9% by additional TEMPO oxidation. This was found to arise from swelling or slight fibrillation of the pulp fibers oxidized for a long time with stirring (Figure 2.7), which will also be interpreted in the latter part..

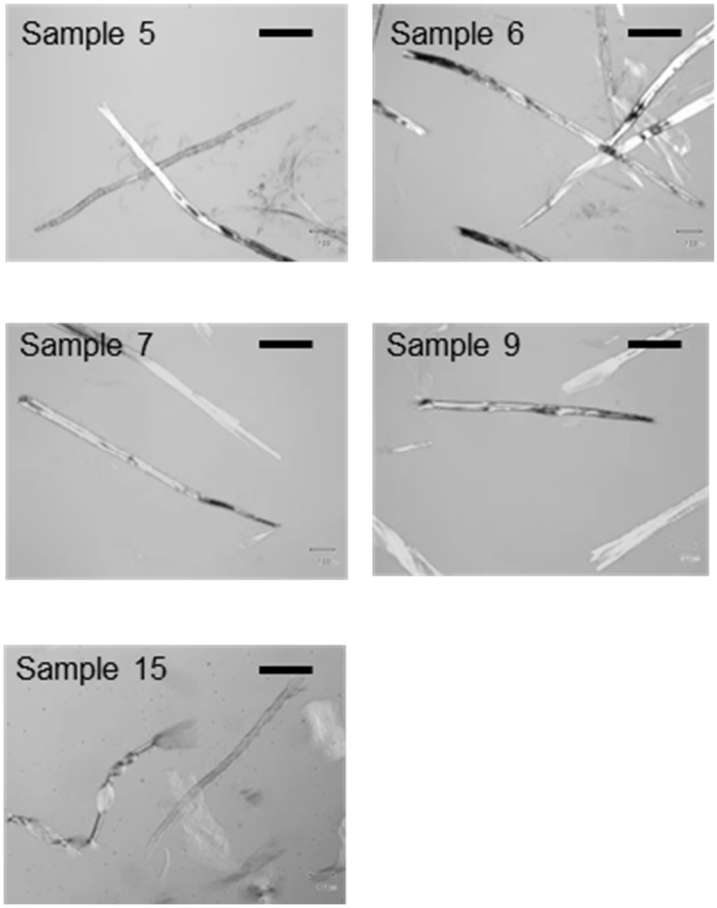

Figure 2.7. Optical microscope images of the pulp samples. (sample 5: dewaxed pulp, sample 6: delignified pulp, sample 7: hemicellulose-extracted pulp, sample 9 and 15: TEMPO-oxidized pulp samples with carboxylate contents of 0.8 and 1.4, respectively)

2.4.3 Mechanical fibrillation *vs.* CI value

CNF samples with different degrees of fibrillation were prepared from the oxidized pulps by wet mechanical disintegration using a double-cylinder-type homogenizer. Figure 2.8a shows the Tyndall phenomena of two CNF dispersions. The turbid dispersion (sample 11) includes a more unfibrillated fraction, and the laser beam is greatly scattered. In contrast, the CNFs in the transparent dispersion (sample 19) are sufficiently fibrillated, and the laser path is

thin and sharp. The weighted average width of such transparent CNFs is estimated to be 3.0 nm from its turbidity curve (Figure 2.9)[30].

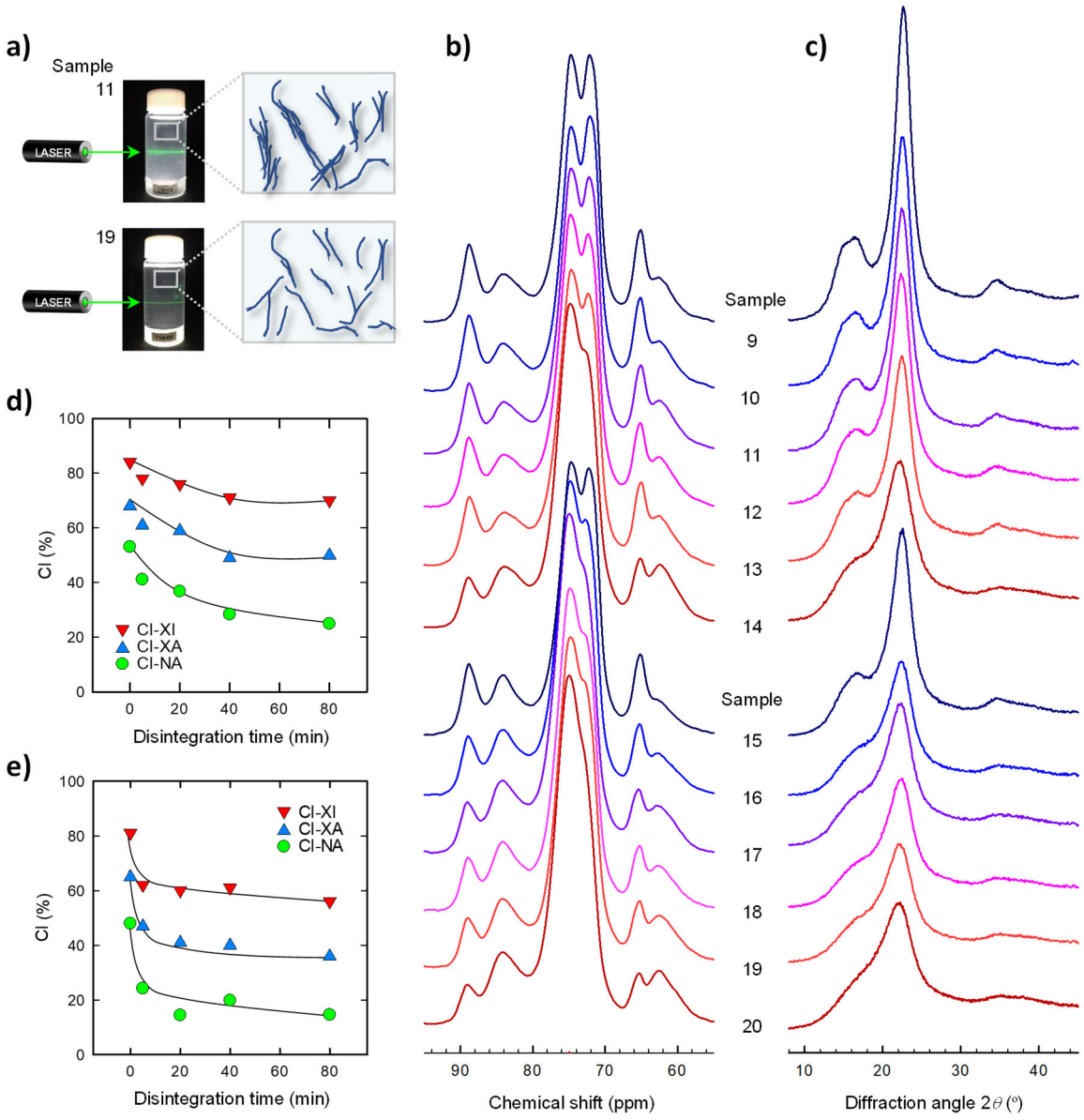

Figure 2.8. Effect of fibrillation. a) Tyndall phenomena of two CNF dispersions with different degrees of fibrillation. The magnified images in the right part are hand-drawn sketches of simplified CNF structures in the corresponding dispersions. b) CP/MAS ^{13}C NMR spectra of the CNF samples. c) XRD profiles of the CNF samples. d) and e) Changes in the CI values with the disintegration time for the CNF samples with carboxylate contents of 0.8 and 1.4 mmol/g, respectively.

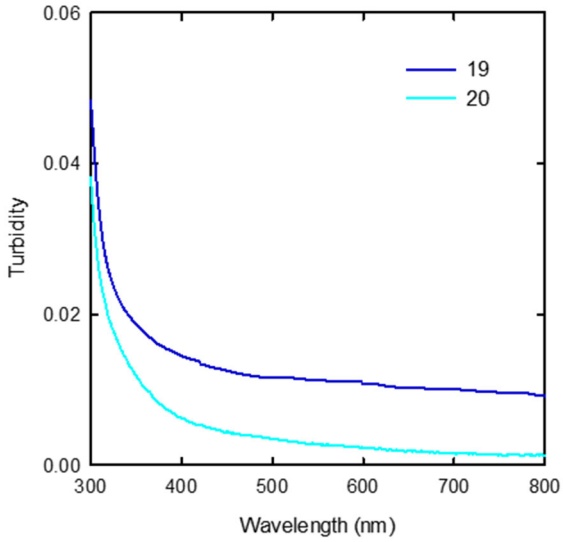

Figure 2.9. Turbidity curves of samples 19 and 20

As fibrillation proceeds, the NMR spectrum gradually changes (Figure 2.8b). The change is clearly visible in the C4 region; the crystalline signal at 88.8 ppm decreased with fibrillation, and instead the noncrystalline signal increased. The similar trend was observed in the C6 region. Although the other signals (C2, C3, and C5) are overlapped and are difficult to precisely interpret, they changed in shape. The XRD profiles also show a drastic change in both the intensity and shape (Figure 2.8c). All of the crystalline peaks at 14.6, 16.4, 22.6, and 34.5° were weakened in intensity and became broadened. Accordingly, the dip at around 18° between the crystalline peaks became invisible. The CI values calculated from these NMR and XRD data are shown in Figure 2.8d,e for the two types of CNF samples with carboxylate contents of 0.8 and 1.4 mmol/g (samples 9–20), respectively. Similar to the case of the cellulose content in Figure 2.5, the three CI values show trends similar with mechanical disintegration. The CI values decrease with increasing disintegration time. However, there is a clear difference between the two CNF samples. The CI values of the low carboxylate content sample gradually decrease with increasing disintegration time (Figure 2.8d). In contrast, the CI values of the high carboxylate content sample rapidly decrease at the initial stage and then reach plateaus (Figure 2.8e). The disintegration treatment adopted here is sufficiently mild that it does not destroy the crystal structure of cellulose (the CI values of samples 7 and 8 are almost the same;

see Figure 2.10). Therefore, the decreases in the CI values should be because of fibrillation rather than destruction of the crystallites.

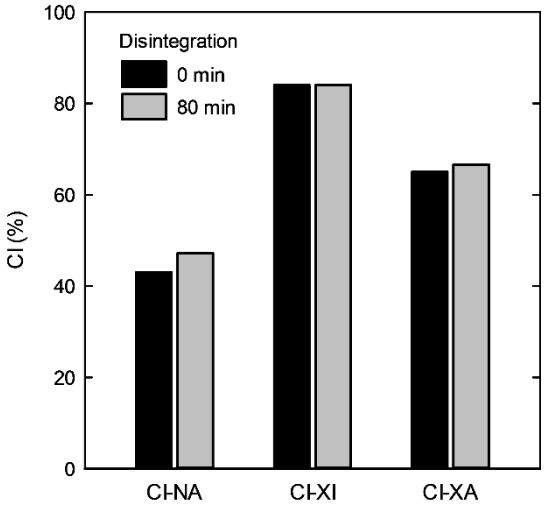

Figure 2.10. Changes in the CI values of the hemicellulose-extracted pulp with wet mechanical disintegration (samples 7 and 8).

2.4.4 Specific surface area *vs.* CI value

The CI values for all of the CNF samples are plotted against their SSAs in Figure 2.11. Here, two additional samples are included: a highly fibrillated sample prepared using a high-pressure homogenizer (sample 20) and a gently fibrillated sample prepared by magnetic stirring (sample 21). As the SSA increases with fibrillation, the three CI values decrease in a similar manner (by approximately 30%) and finally reach plateaus where a-few-nanometers-wide CNFs are individually dispersed (see Figure 2.16). The following three points should be noted: (1) the CI values for the sample gently fibrillated by magnetic stirring (sample 21) fit each approximate curve for the CI values of the other CNF samples, (2) the SSA of amorphous cellulose (sample 4) is as low as 15 m^2/g, and (3) even when the dispersed CNFs were further subjected to prolonged disintegration treatment using a high-pressure homogenizer, the resulting CNFs with shortened lengths and more kinks showed little change in the CI value (~1%; see Figure 2.12). Considering these results, it is reasonable to consider that the decrease in the CI values, accompanied by the increase in the SSA, is mainly because of fibrillation rather than destruction of the microfibril structure, such as shortening and kinking; such

destructions are likely to occur locally along the long axis of CNFs, resulting in minor contributions to the CI values.[38]

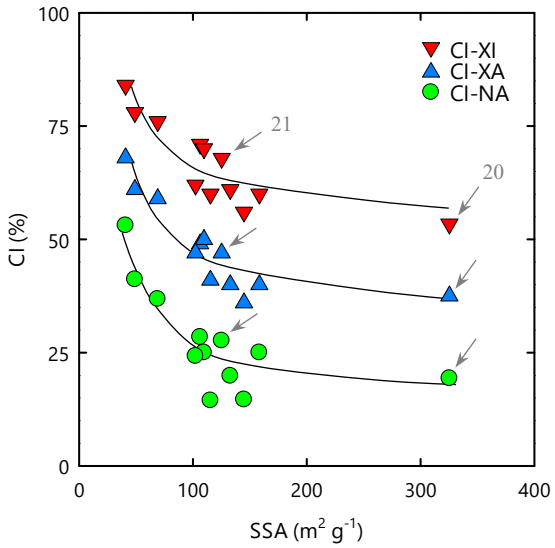

Figure 2.11. Relationships between the CI values and the SSA. The arrows indicate the CNF samples prepared using a high-pressure homogenizer (sample 20) and a magnetic stirrer (sample 21). The other points are for the CNF samples prepared using a double-cylinder-type homogenizer.

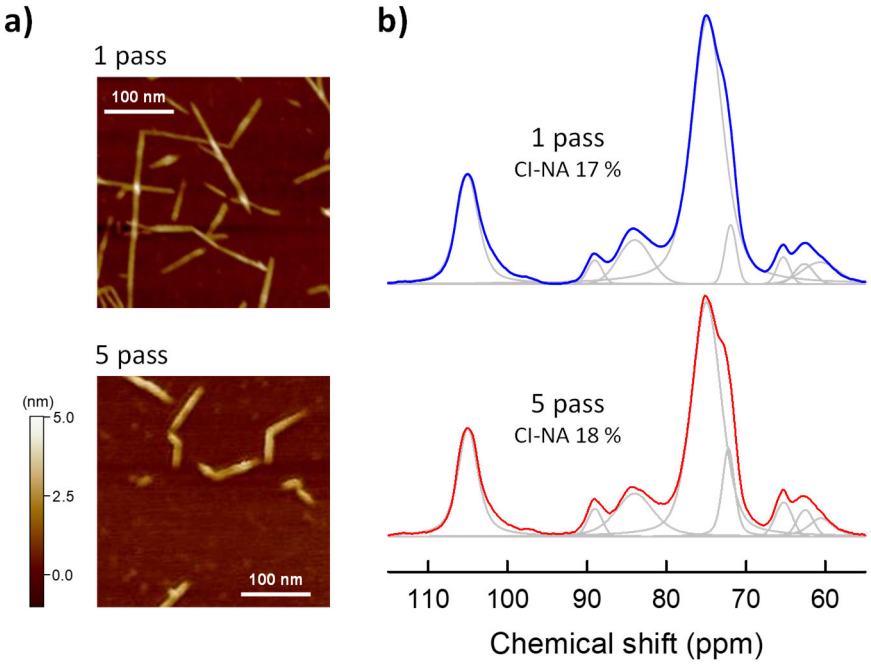

Figure 2.12. Changes in morphology and crystallinity of CNFs by prolonged disintegration treatment using a high-pressure homogenizer: a) AFM images, b) CP/MAS ^{13}C NMR spectra.

2.4.5 Crystal size *vs.* CI value

The relationships between the XRD-based CI values and crystal sizes of a series of samples are shown in Figure 2.13. Both CI values (CI-XI and CI-XA) show strong correlations with the corresponding crystal sizes (CS-I and CS-A). As the CI values of the pulps increase with hemicellulose removal (samples 6 and 7), their crystal sizes also increase. It has been reported that the crystal size of cellulose in wood pulps increases by some processes that induce the agglomeration of cellulose microfibrils, such as purification, drying, and hydrothermal treatment[39-42]. The gradual decreases in the CI values in the process of fibrillation (samples 9–21) are accompanied by decreases in the crystal sizes. These results indicate that (1) the crystallinity increases as the microfibrils are more densely bundled with increasing cellulose content and (2) the crystallinity decreases as the microfibrils disperse with disintegration as CNFs; the interfacial molecules between bundled microfibrils are partly crystalline, which is the same concept as the structural insights described by Newman et al. and Jarvis et al. using the term "twinning" [43, 44]. This interpretation is supported by the solid curve in Figure 2.13 based on the simulation data reported by French and Santiago Cintrón[30], which shows the ideal relationship between the Segal CI value and the crystal size of the (2 0 0) plane, eliminating any contributions of scattering from the simulated XRD profiles. The simulation-based CI value and crystal size are calculated in the same manner as the CI-XI and CS-I values in the present study, respectively. Surprisingly, our experimental data for a series of samples with different cellulose contents or degrees of fibrillation (CI-XI/CS-I for samples 5–21) well fit the simulated curve. Furthermore, the data for the acid hydrolysates, or chemically isolated crystallites, of tunicate, cotton, and wood celluloses (samples 1–3) are included in Figure 13, and they also fit the curve. These results suggest that the XRD profiles of the wood pulps and CNFs are mostly composed of crystalline diffraction peaks, and the broad peaklike scattering by the amorphous components and moisture is sufficiently weak that it can be ignored. In other words, the assumption of amorphous scattering in the CI-XA/CS-A calculation (Figure 2.1c) is overestimated; this is most likely because the crystalline diffractions tend to focus on the equator in the power XRD profiles of pelletized or filmlike samples by the reflection method), whereas the scattering by the amorphous components and moisture is averaged over all azimuthal angles..

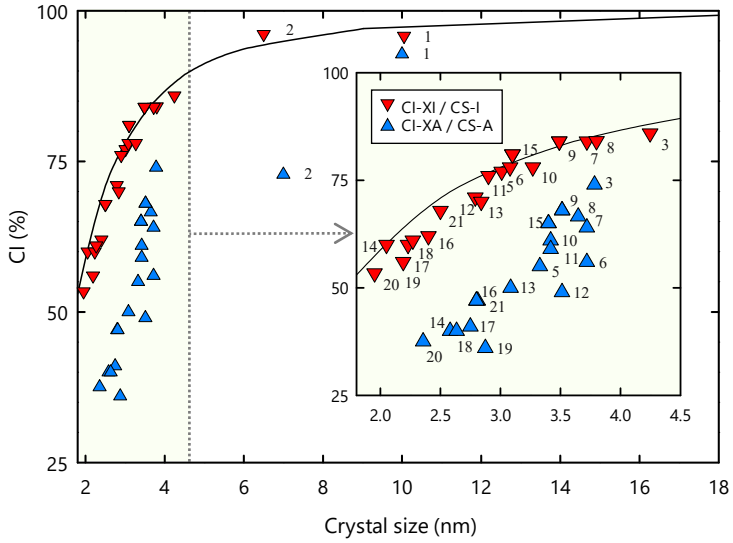

Figure 2.13. Relationships between the CI values and crystal sizes. The numbers next to the symbols indicate the corresponding samples. The solid curve is drawn based on the simulation data reported by French and Santiago Cintrón. (sample 1: acid-hydrolyzed tunicate cellulose, sample 2: acid-hydrolyzed cotton cellulose, sample 3: acid-hydrolyzed wood cellulose, sample 6: delignified pulp, sample 7: hemicellulose-extracted pulp, sample 8: mechanically treated hemicellulose-extracted pulp, sample 9: TEMPO-oxidized pulp with NaClO addition of 5 mmol/g, sample 10–13: CNFs; sample 9 mechanically treated for 5–80 min, respectively, sample 14: CNFs; sample 9 treated with a high-pressure homogenizer, ,sample 15: TEMPO-oxidized pulp with NaClO addition of 10 mmol/g, sample 16–21: CNFs; sample 15 mechanically treated for 5–80 min with the double-cylinder-type mechanical homogenizer and with the high-pressure homogenizer, respectively.)

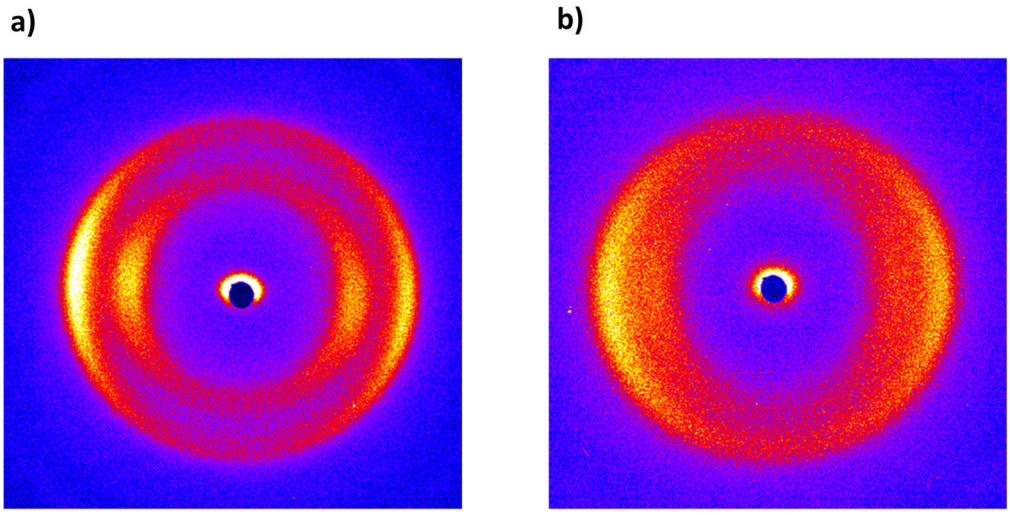

Figure 2.14. XRD diagrams of the pelletized samples for the incident beam parallel to the pellet plane: a) sample 5: dewaxed pulp, b) sample 20: CNF sample with carboxylate contents of 1.4 treated by using high-pressure homogenizer.

2.4.6 Crystal size *vs.* AFM height

The crystal sizes were then compared with the AFM height profiles of the respective CNF samples spread on flat mica surfaces (Figure 2.15a). To minimize experimental error, the AFM measurements of the CNF heights were performed in peak-force tapping mode with careful monitoring to ensure that the tip did not compress the sample. The largest height values measured along the isolated, straight, and nontwisted parts of CNFs in the fiber axis direction were taken as the true height values of the respective CNFs, taking into consideration that the tapping step (∼2 nm) is similar to the CNF width (approximately 2–3 nm)[45]. The twisting was clearly visible on bundled microfibrils in the AFM observation, as reported by Usov et al., where detection relies on the local increase in the AFM height along the microfibrils[46].

As the fibrillation proceeds, both CS-I and CS-A values significantly decrease, whereas the AFM height values are nearly unchanged within a narrow mean value range of 2.4–2.6 nm. These height values are in good agreement with those reported for individualized microfibrils[1, 45-47]. The CS-A values decrease from 3.4 to 2.4 nm with fibrillation. The latter is close to the AFM height value (2.6 nm). However, this result is not rational because, even for an ideal crystallite, the Scherrer crystal size, or a lower limit of the crystallite dimension, is at least one molecular thickness smaller than the actual geometric dimension of the crystallite in the corresponding direction. [Note that, assuming the cross-sectional shapes of the 18-chain models as discussed in the latter part of this paper, the AFM height should have a mean value with a large standard deviation, as shown in Figure 2.15a, while the CS value is the crystal size of the (2 0 0) plane, which, on average, is smaller than those of the other planes.] The CS-I values decrease from 2.9 to 2.0 nm. The value of 2.0 nm in the final stage of fibrillation is suitably smaller than the AFM height value (2.6 nm).

Figure 2.15b shows an AFM image of sample 12. The two CNFs indicated by parts a and b in the image have the same height value (2.6 nm), but they have considerably different widths. These CNFs are assumed to a microfibril bundle and an individualized microfibril. As fibrillation proceeds, these bundles disintegrate into individual microfibrils, and the CNFs finally become uniform (Figure 2.17). In fact, CNFs with low degrees of fibrillation are ribbon-like bundles of laterally associated cellulose microfibrils, as reported for cellulose nanocrystals[34] . The separation of such associated surfaces results in a decrease of the CS value

(Figure 2.15a), and the laterally associated surfaces should be crystalline. Accordingly, the CS value decreases inversely with the SSA (Figure 2.17); it is explained based on the following relationship between the theoretical SSA of ribbon-like microfibril bundles with rectangular cross sections of a constant thickness and their widths D_w:

$$\mathrm{SSA} = \alpha + \frac{\beta}{D_w}$$

where α and β are constants related to the thickness and true density, and the fibril length is assumed to be infinite.

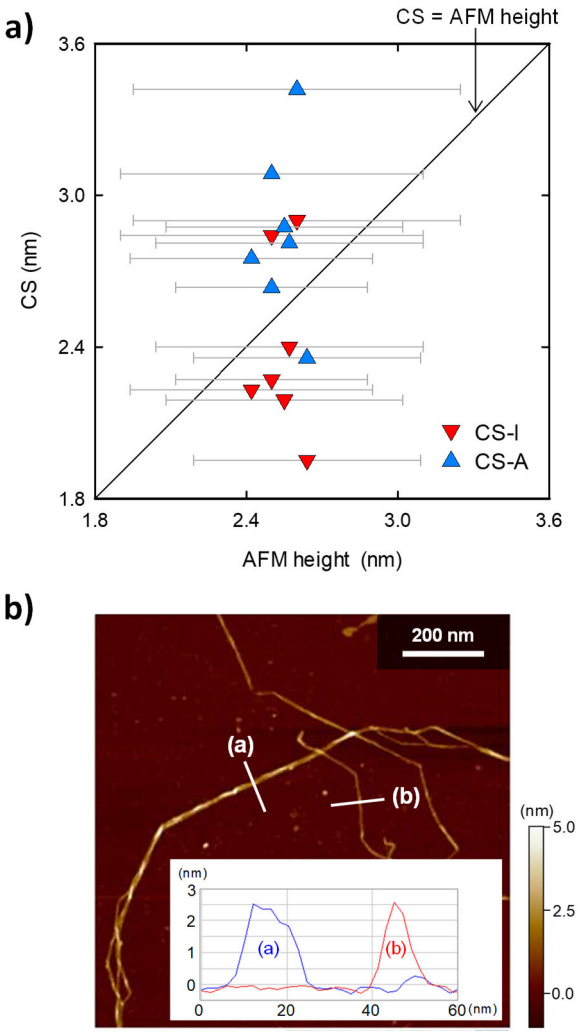

Figure 2.15. Morphological analysis of the CNF samples. a) Relationship between the CS values and the AFM heights of the CNF samples spread on flat mica surfaces. The gray lines indicate the standard deviations of the AFM heights. b) AFM height images of CNFs with different degrees of fibrillation.

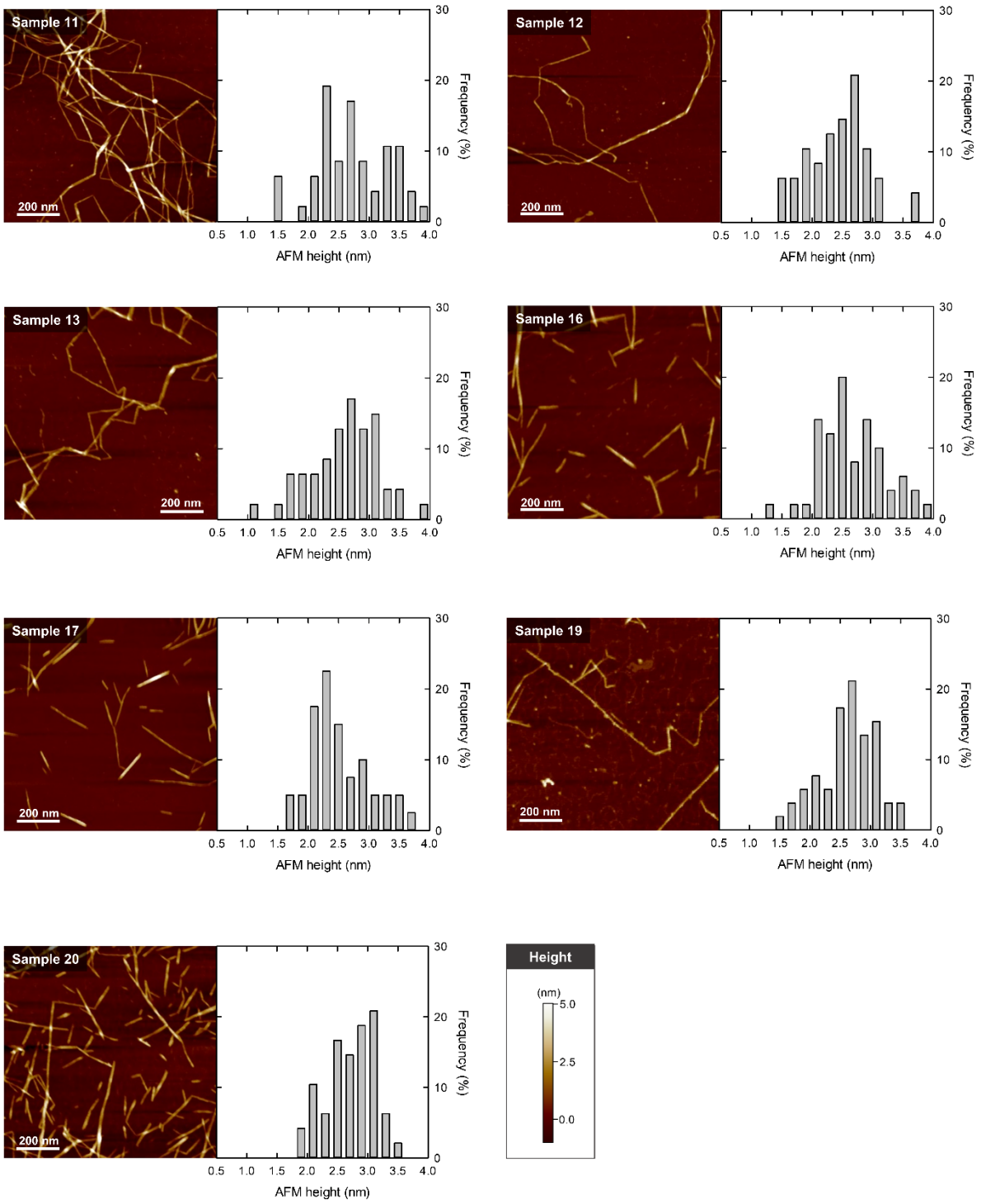

Figure 2.16. AFM height images and height distribution histograms of the CNF samples. (sample 11–13: CNF samples with carboxylate contents of 0.8 mechanically treated for 20–80 min, respectively, sample 16–20: CNF samples with carboxylate contents of 1.4 mechanically treated for 5–80 min with the double-cylinder-type mechanical homogenizer and with the high-pressure homogenizer, respectively.)

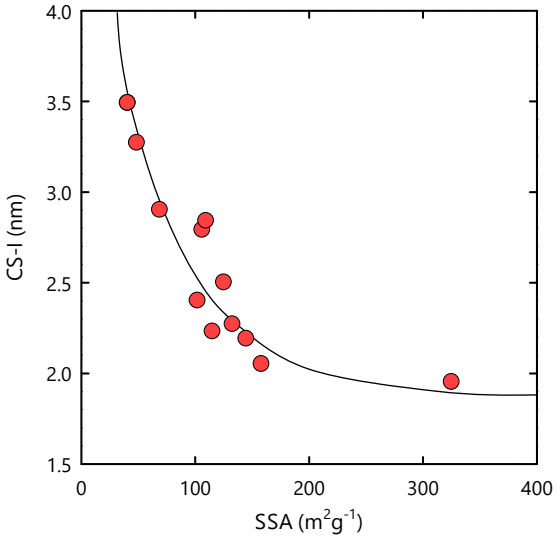

Figure 2.17. Relationship between the CS-I and SSA values.

2.4.7 The C6 conformation *vs.* crystal size

Cellulose has three C6 conformations: trans–gauche (*tg*), gauche–trans (*gt*), and gauche–gauche [47] with signals centered at 65.2, 62.5, and 60.6 ppm, respectively.[48] It has been proposed that the *tg* conformation is crystalline and occurs in the core region of the microfibril, while the *gg* conformation is noncrystalline[8, 35, 48, 49]. Although these attributions have recently been shown to be oversimplified by multidimensional NMR spectroscopy,[50] the following facts have also been observed; when a cellulose I type sample is chemically treated by TEMPO oxidation, both the *tg* signal and XRD-based crystal size of the original sample are preserved, the gg signal decreases, and instead a carbonyl signal appears at 174 ppm[51, 52]. Here, the decrement in the *gg* signal quantitatively corresponds to the signal area of the carbonyl groups upon examination under appropriate conditions[52, 53](see Appendix). Therefore, the C6 signals were divided into three contributions: *tg*, *gt*, and the sum of *gg* and carbonyl carbon (*gg* + C═O). The signal area ratios of the contributions with respect to the total C6 area are plotted against the CS-I values in Figure 2.18. With decreasing CS-I value, the *tg* ratio decreases in a roughly linear manner from about 50% to 20% (Figure 2.18a). It should be noted that the decrease in the *tg* ratio of approximately 30% is nearly the same as the decrease in the C4-based CI-NA value (Figure 2.19). The *gg* + C═O ratio increases from about 20% to 60% as the CS-I value decreases (Figure 2.18b). These analyses also indicate that the cellulose molecules at the

interface between bundled microfibrils or at the surface of the individual microfibrils are partly crystalline and become disordered when the microfibrils disperse as CNFs.

The *gt* carbon atoms have been suggested to be an intermediate conformation existing in the noncrystalline region of the microfibrils[49], but this is still under debate. The *gt* ratio shows a slight decreasing trend with decreasing CS-I value (Figure 2.18c), which is similar to the trend of the crystalline *tg* ratio (Figure 2.18a) but opposite to that of the *gg* ratio (Figure 2.18b).

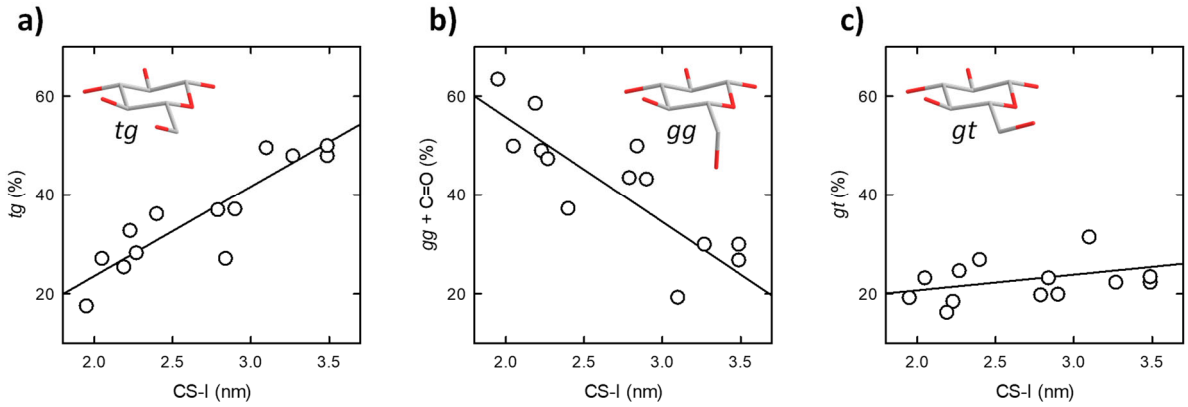

Figure 2.18. Relationships between the CS-I value and the ratios of C6 carbons in the a) *tg*, b) *gg* + C=O, and c) *gt* conformations.

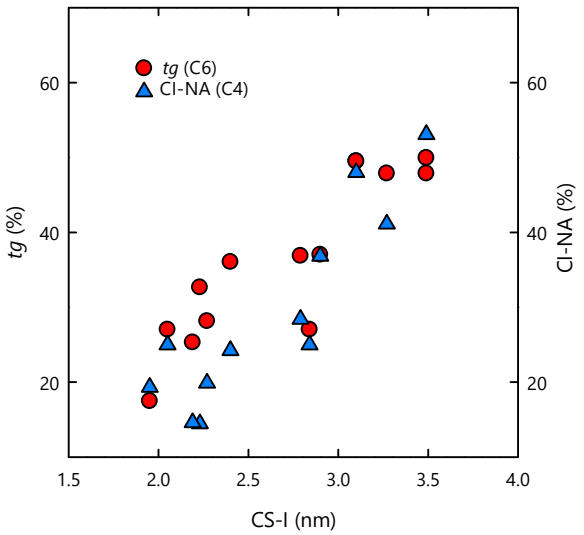

Figure 2.19. Relationship between the *tg* ratio of C6 carbons and the C4-based CI-NA value as a function of the CS-I value.

2.4.8 Model analysis

Figure 2.20 shows schematic models of the cross section of a cellulose microfibril consisting of 18 molecular chains, which are two models of a variety of the proposals by Newman et al.[43] It has been proposed that the 18- or 24-chain model is plausible for the number of cellulose molecular chains in a single microfibril[35, 50, 54-57]. Our morphological analyses of the individualized microfibrils (sample 20) support the 18-chain model (see Figure 2.21 for the 24-chain model). For the cross-sectional dimension, AFM analysis gives an arithmetic mean of 2.6 nm with a standard deviation of 0.5 nm, and the weighted mean estimated from the turbidity curve is 2.8 nm (Figure 2.9)[30]. Surprisingly, a most recent study proved the structure of a poplar cellulose synthase CesA homotrimer, which strongly supports the cellulose microfibril is consists of 18 chains[58].

The *gg* + C═O and *tg* ratios of sample 20 are approximately 63% and 17%, respectively; note here that the cellulose content of sample 20 is sufficiently high (~99%; see Figures 2.5 and 2.6). On the basis of the 18-chain model, the *gg* + C═O ratio is in good agreement with the ratio of the surface 12 chains to whole 18 chains (~67%), and the *tg* ratio suggests that three or four chains in the core region of an individualized microfibril are crystalline, which is equivalent to the C4-based CI-NA value (~17%). Meanwhile, the CS-I value of sample 20 is approximately 2.0 nm, which is similar to the crystal size of the (2 0 0) plane for the 18-chain model in Figure 2.20 (1.95 nm). Considering the 18-chain model, not only the core but also the surface molecules, which are regarded as a noncrystalline region in conformational analysis of the C4 and C6 carbon atoms by NMR, are ordered in molecular sheet stacking to diffract X-rays[59].

For verification of the molecular sheet stacking, we measured the true density values of three types of cellulosic samples: a pulp with a high cellulose content of approximately 97%, its TEMPO-oxidized one, and fibrillated CNFs. The true density of the original pulp was 1.57 g/cm^3, which is a reasonable value considering the crystal density of cellulose Iβ (1.63 g/cm^3) and the residual hemicelluloses (~3%). Then, the value reasonably increased up to 1.69 g/cm^3 through oxidation or conversion of the C6 hydroxyl groups to sodium carboxylates (~1.7 mmol/g). The value for the oxidized pulp was indeed nearly unchanged even after fibrillation, and the true density of the CNF sample stayed at 1.67 g/cm^3. These results indicate that the

conformational changes in the constituent carbon atoms, detected by NMR, are insensitive to the density of the molecular sheet stacking in microfibrils. The structural changes occurring at the microfibril surfaces are graphically summarized in Figure 2.22.

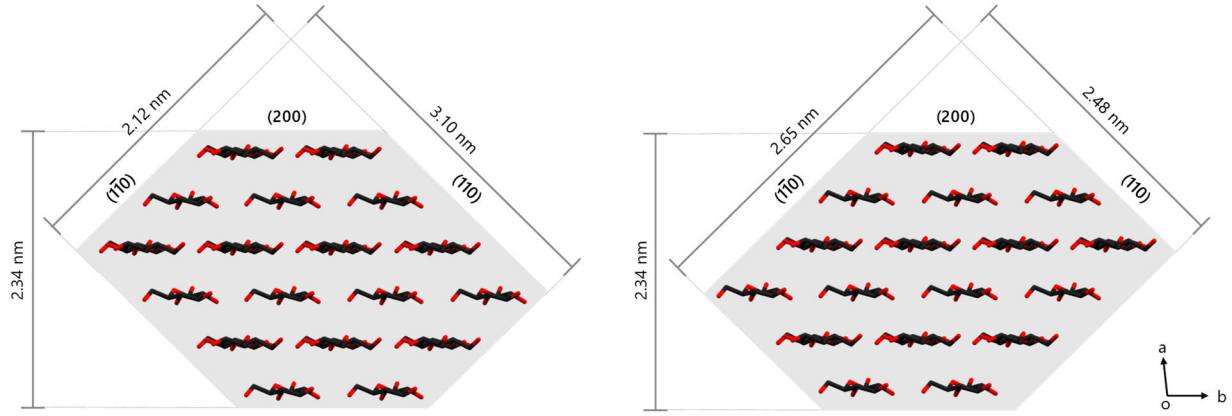

Figure 2.20. Cross-sectional dimensions of the 18-chain model of cellulose microfibrils.

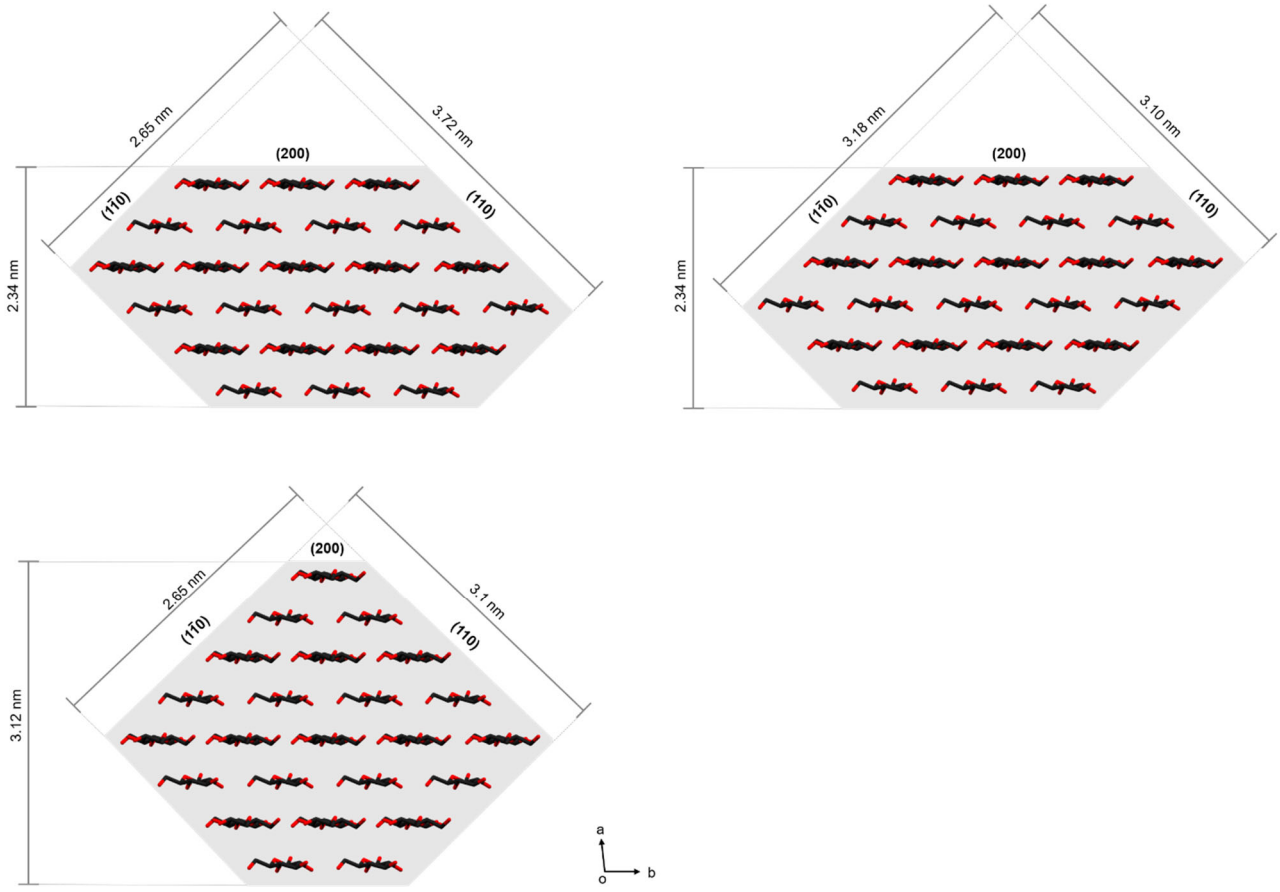

Figure 2.21. Cross-sectional dimensions of the 24-chain model of cellulose microfibrils.

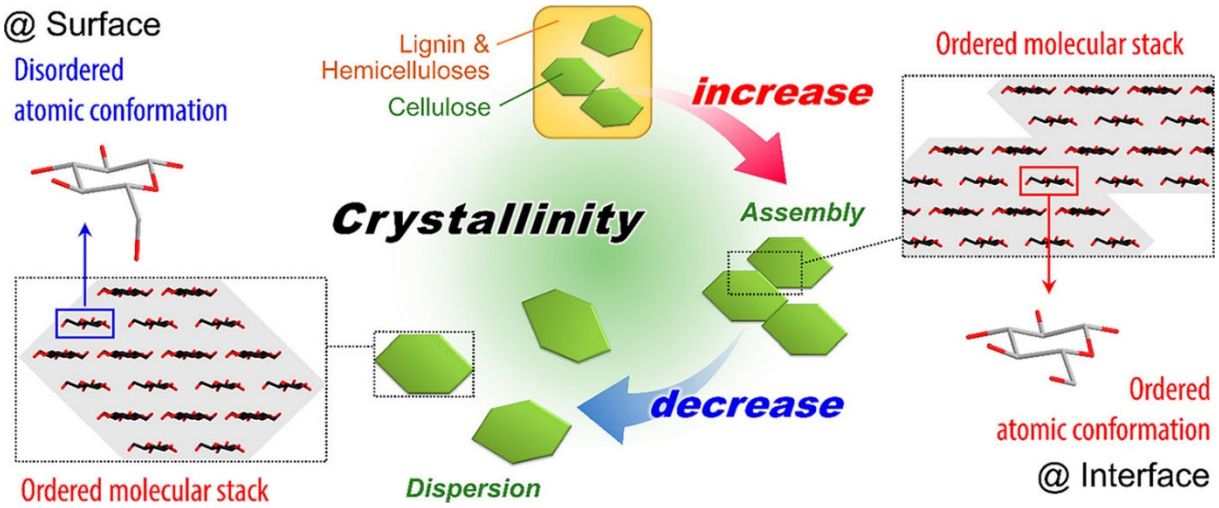

Figure 2.22. The dispersion-induced disordering of the interfacial molecules between bundled microfibrils in wood cellulosic structure.

2.5 Conclusions

The Three types of CI values for approximately 20 samples ranging from a wood pulp to CNFs were measured. The CI values were first compared with the cellulose contents of the samples: (1) all of the CI values are nearly unchanged with delignification; (2) the CI-NA value proportionally increases with increasing cellulose content with hemicellulose removal; (3) both XRD-based CI values are higher than the cellulose contents in some cases, and they show relatively weak dependence on the cellulose content. Next, the effect of fibrillation on the CI values was investigated; as the SSA increases with fibrillation, the three CI values decrease by approximately 30% in a similar manner, reaching plateaus where microfibrils are individually dispersed as a-few-nanometers-wide CNFs.

The relationships between the CI values and either the crystal size or SSA show the following trends: (1) as the CI values increase with hemicellulose removal, the crystal size also increases; (2) the decrease of the CI values in the process of fibrillation is accompanied by a decrease in the crystal size and by an increase in SSA. These results suggest that the cellulose molecules at the interface between bundled microfibrils are partly crystalline and become disordered when the microfibrils disperse as CNFs. Interestingly, the relationship between the CI-XI value and crystal size fits the simulation data reported by French and Santiago Cintrón[22] demonstrating that broad peaklike X-ray scattering by the amorphous components is sufficiently weak that it can be ignored.

Morphological analysis of the individualized microfibrils supported the 18-chain model. Considering the 18-chain model, not only the core but also the surface molecules, which are regarded as a noncrystalline region in conformational analysis of the C4 and C6 carbon atoms by NMR, are ordered in molecular sheet stacking to diffract X-rays.

Overall, we conclude the following points about the crystallinity of CNFs: (1) The NMR-based CI value is rational, but the samples need to be delignified in advance. (2) The XRD-based CI value can be approximated with a function of the crystal size, as reported by French and Santiago Cintrón,[22] when being calculated after subtracting the background from the powder XRD profiles of pelletized or filmlike samples by the reflection method. (3) Dispersion-induced disordering of the interfacial molecules between bundled microfibrils governs the crystallinity of the CNFs.

2.6 References

1. Saito, T.; Kuramae, R.; Wohlert, J.; Berglund, L. A.; Isogai, A., An ultrastrong nanofibrillar biomaterial: the strength of single cellulose nanofibrils revealed via sonication-induced fragmentation. *Biomacromolecules* **2013,** *14* (1), 248-53.

2. Wu, X.; Moon, R. J.; Martini, A., Tensile strength of Iβ crystalline cellulose predicted by molecular dynamics simulation. *Cellulose* **2014,** *21* (4), 2233-2245.

3. Sakurada, I.; Nukushina, Y.; Ito, T., Experimental determination of the elastic modulus of crystalline regions in oriented polymers. *J. Polym. Sci.* **1962,** *57*, 651.

4. Wohlert, J.; Bergenstråhle-Wohlert, M.; Berglund, L. A., Deformation of cellulose nanocrystals : entropy, internal energy and temperature dependence. *Cellulose* **2012,** *19*, 1821.

5. Hori, R.; Wada, M., The thermal expansion of wood cellulose crystals. *Cellulose* **2005,** *12* (5), 479-484.

6. Bergenstråhle, M.; Berglund, L. A.; Mazeau, K., Thermal Response in Crystalline Iβ Cellulose: A Molecular Dynamics Study. *J. Phys. Chem. B* **2007,** *111*, 9138.

7. Inui, T.; Koga, H.; Nogi, M.; Komoda, N.; Suganuma, K., A miniaturized flexible antenna printed on a high dielectric constant nanopaper composite. *Adv Mater* **2015,** *27* (6), 1112-6.

8. Nishiyama, Y.; Langan, P.; Chanzy, H., Crystal Structure and Hydrogen-Bonding System in Cellulose Iβ from Synchrotron X-ray and Neutron Fiber Diffraction. *J. Am. Chem. Soc.* **2002,** *124*, 9074.

9. Koyama, M.; Helbert, W.; Imai, T.; Sugiyama, J.; Henrissat, B., Parallel-up structure evidences the molecular directionality during biosynthesis of bacterial cellulose. *Proc Natl Acad Sci U S A* **1997,** *94* (17), 9091-5.

10. Hermans, P. H.; Weidinger, A., Quantitative X-Ray Investigations on the Crystallinity of Cellulose Fibers - a Background Analysis. *Journal of Applied Physics* **1948,** *19* (5), 491-506.

11. Segal, L.; Creely, J. J.; Martin, A. E.; Conrad, C. M., An Empirical Method for Estimating the Degree of Crystallinity of Native Cellulose Using the X-Ray Diffractometer. *Text. Res. J.* **1959,** *29*, 786.

12. Isogai, A.; Usuda, M., Crystallinity Indexes of Cellulosic Materials. *Sen'i Gakkaishi* **1990,** *46*, 324.

13. Akerholm, M.; Hinterstoisser, B.; Salmen, L., Characterization of the crystalline structure of cellulose using static and dynamic FT-IR spectroscopy. *Carbohydrate Research* **2004,** *339* (3), 569-578.

14. Andersson, S.; Serimaa, R.; Paakkari, T.; Saranpaa, P.; Pesonen, E., Crystallinity of wood and the size of cellulose crystallites in Norway spruce (Picea abies). *Journal of Wood Science* **2003,** *49* (6), 531-537.

15. Thygesen, A.; Oddershede, J.; Lilholt, H.; Thomsen, A. B.; Ståhl, K., On the determination of crystallinity and cellulose content in plant fibres. *Cellulose* **2005,** *12*, 563.

16. Park, S.; Baker, J. O.; Himmel, M. E.; Parilla, P. A.; Johnson, D. K., Cellulose crystallinity index: measurement techniques and their impact on interpreting cellulase performance. *Biotechnol. Biofuels* **2010,** *3*, 10.

17. Bansal, P.; Hall, M.; Realff, M. J.; Lee, J. H.; Bommarius, A. S., Multivariate statistical analysis of X-ray data from cellulose: a new method to determine degree of crystallinity and predict hydrolysis rates. *Bioresour Technol* **2010,** *101* (12), 4461-71.

18. Park, S.; Johnson, D. K.; Ishizawa, C. I.; Parilla, P. A.; Davis, M. F., Measuring the crystallinity index of cellulose by solid state 13C nuclear magnetic resonance. *Cellulose* **2009,** *16* (4), 641-647.

19. Driemeier, C.; Calligaris, G. A., Theoretical and experimental developments for accurate determination of crystallinity of cellulose I materials. *Journal of Applied Crystallography* **2011,** *44*, 184-192.

20. Terinte, N.; Ibbett, R.; Schuster, K. C., Overview on Native Cellulose and Microcrystalline Cellulose I Structure Studied by X-ray Diffraction (WAXD): Comparison between Measurement Techniques. *Lenzinger Berichte* **2011,** *89*, 118.

21. Kim, S. H.; Lee, C. M.; Kafle, K., Characterization of crystalline cellulose in biomass: Basic principles, applications, and limitations of XRD, NMR, IR, Raman, and SFG. *Korean Journal of Chemical Engineering* **2013,** *30* (12), 2127-2141.

22. French, A. D.; Cintron, M. S., Cellulose polymorphy, crystallite size, and the Segal Crystallinity Index. *Cellulose* **2013,** *20* (1), 583-588.

23. Ju, X.; Bowden, M.; Brown, E. E.; Zhang, X., An improved X-ray diffraction method for cellulose crystallinity measurement. *Carbohydr Polym* **2015,** *123*, 476-81.

24. Nam, S.; French, A. D.; Condon, B. D.; Concha, M., Segal Segal crystallinity index revisited by the simulation of X-ray diffraction patterns of cotton cellulose Iβ and cellulose II. *Carbohydr. Polym.* **2016,** *135*, 1.

25. Wickholm, K.; Larsson, P. T.; Iversen, T., Assignment of non-crystalline forms in cellulose I by CP/MAS 13C NMR spectroscopy. *Carbohydr. Res.* **1998,** *312*, 123.

26. Heux, L.; Dinand, E.; Vignon, M. R., Structural aspects in ultrathin cellulose microfibrils followed by 13C CP-MAS NMR. *Carbohydr. Polym.* **1999,** *40*, 115.

27. Nemoto, J.; Saito, T.; Isogai, A., Simple Freeze-Drying Procedure for Producing Nanocellulose Aerogel-Containing, High-Performance Air Filters. *ACS Appl Mater Interfaces* **2015,** *7* (35), 19809-15.

28. Okita, Y.; Saito, T.; Isogai, A., Entire surface oxidation of various cellulose microfibrils by TEMPO-mediated oxidation. *Biomacromolecules* **2010,** *11*, 1696.

29. Ono, Y.; Tanaka, R.; Funahashi, R.; Takeuchi, M.; Saito, T.; Isogai, A., SEC–MALLS analysis of ethylenediamine-pretreated native celluloses in LiCl/N,N-dimethylacetamide: softwood kraft pulp and highly crystalline bacterial, tunicate, and algal celluloses. *Cellulose* **2016,** *23* (3), 1639-1647.

30. Shimizu, M.; Saito, T.; Nishiyama, Y.; Iwamoto, S.; Yano, H.; Isogai, A.; Endo, T., Fast and Robust Nanocellulose Width Estimation Using Turbidimetry. *Macromol Rapid Commun* **2016,** *37* (19), 1581-1586.

31. Larsson, P. T.; Wickholm, K.; Iversen, T., A CP/MAS13C NMR investigation of molecular ordering in celluloses. *Carbohydrate Research* **1997,** *302* (1-2), 19-25.

32. Driemeier, C.; Bragatto, J., Crystallite width determines monolayer hydration across a wide spectrum of celluloses isolated from plants. *J Phys Chem B* **2013,** *117* (1), 415-21.

33. Alexander, L. E.; Robert, E., *X-ray Diffraction Methods in Polymer Science*. 1979; p 423.

34. Elazzouzi-Hafraoui, S.; Nishiyama, Y.; Putaux, J. L.; Heux, L.; Dubreuil, F.; Rochas, C., The shape and size distribution of crystalline nanoparticles prepared by acid hydrolysis of native cellulose. *Biomacromolecules* **2008,** *9* (1), 57-65.

35. Fernandes, A. N.; Thomas, L. H.; Altaner, C. M.; Callow, P.; Forsyth, V. T.; Apperley, D. C.; Kennedy, C. J.; Jarvis, M. C., Nanostructure of cellulose microfibrils in spruce wood. *Proc Natl Acad Sci U S A* **2011,** *108* (47), E1195-203.

36. Marchessault, R. H.; Taylor, M. G.; Winter, W. T., 13C CP/MAS NMR spectra of poly-β - D (1→4) mannose: mannan. *Can. J. Chem.* **1990,** *68*, 1192.

37. Silveira, R. L.; Stoyanov, S. R.; Kovalenko, A.; Skaf, M. S., Cellulose Aggregation under Hydrothermal Pretreatment Conditions. *Biomacromolecules* **2016,** *17* (8), 2582-90.

38. Nystrom, G.; Arcari, M.; Adamcik, J.; Usov, I.; Mezzenga, R., Nanocellulose Fragmentation Mechanisms and Inversion of Chirality from the Single Particle to the Cholesteric Phase. *ACS Nano* **2018,** *12* (6), 5141-5148.

39. Kuribayashi, T.; Ogawa, Y.; Rochas, C.; Matsumoto, Y.; Heux, L.; Nishiyama, Y., Hydrothermal Transformation of Wood Cellulose Crystals into Pseudo-Orthorhombic Structure by Cocrystallization. *Acs Macro Letters* **2016,** *5* (6), 730-734.

40. Silveira, R. L.; Stoyanov, S. R.; Kovalenko, A.; Skaf, M. S., Cellulose Aggregation under Hydrothermal Pretreatment Conditions. *Biomacromolecules* **2016,** *17*, 2582.

41. Nishiyama, Y.; Langan, P.; O'Neill, H.; Pingali, S. V.; Harton, S., Structural coarsening of aspen wood by hydrothermal pretreatment monitored by small- and wide-angle scattering of X-rays and neutrons on oriented specimens. *Cellulose* **2013,** *21* (2), 1015-1024.

42. Newman, R. H., Carbon-13 NMR evidence for cocrystallization of cellulose as a mechanism for hornification of bleached kraft pulp. *Cellulose* **2004,** *11* (1), 45-52.

43. Newman, R. H.; Hill, S. J.; Harris, P. J., Wide-angle x-ray scattering and solid-state nuclear magnetic resonance data combined to test models for cellulose microfibrils in mung bean cell walls. *Plant Physiol* **2013,** *163* (4), 1558-67.

44. Thomas, L. H.; Forsyth, V. T.; Martel, A.; Grillo, I.; Altaner, C. M.; Jarvis, M. C., Diffraction evidence for the structure of cellulose microfibrils in bamboo, a model for grass and cereal celluloses. *BMC Plant Biol* **2015,** *15*, 153.

45. Tanaka, R.; Saito, T.; Hanninen, T.; Ono, Y.; Hakalahti, M.; Tammelin, T.; Isogai, A., Viscoelastic Properties of Core-Shell-Structured, Hemicellulose-Rich Nanofibrillated Cellulose in Dispersion and Wet-Film States. *Biomacromolecules* **2016,** *17* (6), 2104-11.

46. Usov, I.; Nystrom, G.; Adamcik, J.; Handschin, S.; Schutz, C.; Fall, A.; Bergstrom, L.; Mezzenga, R., Understanding nanocellulose chirality and structure-properties relationship at the single fibril level. *Nat Commun* **2015,** *6*, 7564.

47. Jakob, H. F.; Fengel, D.; Tschegg, S. E.; Fratzl, P., The elementary cellulose fibril in Picea abies: Comparison of transmission electron microscopy, small-angle X-ray scattering, and wide-angle X-ray scattering results. *Macromolecules* **1995,** *28* (26), 8782-8787.

48. Horii, F.; Hirai, A.; Kitamaru, R., Solid-state 13C-NMR study of conformations of oligosaccharides and cellulose. *Polymer Bulletin* **1983,** *10* (7-8), 357-361.

49. Viëtor, R. J.; Newman, R. H.; Ha, M. A.; Apperley, D. C.; Jarvis, M. C., Conformational features of crystal-surface cellulose from higher plants. *Plant J.* **2002,** *30*, 721.

50. Wang, T.; Hong, M., Solid-state NMR investigations of cellulose structure and interactions with matrix polysaccharides in plant primary cell walls. *J. Exp. Bot.* **2016,** *67*, 503.

51. Funahashi, R.; Okita, Y.; Hondo, H.; Zhao, M.; Saito, T.; Isogai, A., Different Conformations of Surface Cellulose Molecules in Native Cellulose Microfibrils Revealed by Layer-by-Layer Peeling. *Biomacromolecules* **2017,** *18* (11), 3687-3694.

52. Saito, T.; Hirota, M.; Tamura, N.; Kimura, S.; Fukuzumi, H.; Heux, L.; Isogai, A., Individualization of nano-sized plant cellulose fibrils by direct surface carboxylation using TEMPO catalyst under neutral conditions. *Biomacromolecules* **2009,** *10* (7), 1992-6.

53. Montanari, S.; Rountani, M.; Heux, L.; Vignon, M. R., Topochemistry of carboxylated cellulose nanocrystals resulting from TEMPO-mediated oxidation. *Macromolecules* **2005,** *38* (5), 1665-1671.

54. Jarvis, M. C., Cellulose biosynthesis: counting the chains. *Plant Physiol* **2013,** *163* (4), 1485-6.

55. Cosgrove, D. J., Re-constructing our models of cellulose and primary cell wall assembly. *Curr Opin Plant Biol* **2014,** *22*, 122-131.

56. Oehme, D. P.; Downton, M. T.; Doblin, M. S.; Wagner, J.; Gidley, M. J.; Bacic, A., Unique Aspects of the Structure and Dynamics of Elementary Iβ Cellulose Microfibrils Revealed by Computational Simulations. *Plant Physiol.* **2015,** *168*, 3.

57. Nixon, B. T.; Mansouri, K.; Singh, A.; Du, J.; Davis, J. K.; Lee, J. G.; Slabaugh, E.; Vandavasi, V. G.; O'Neill, H.; Roberts, E. M.; Roberts, A. W.; Yingling, Y. G.; Haigler, C. H.,

Comparative Structural and Computational Analysis Supports Eighteen Cellulose Synthases in the Plant Cellulose Synthesis Complex. *Sci. Rep.* **2016,** *6*, 28696.

58. Purushotham, P.; Ho, R.; Zimmer, J., Architecture of a catalytically active homotrimeric plant cellulose synthase complex. *Science* **2020,** *369* (6507), 1089-1094.

59. Nishiyama, Y.; Johnson, G. P.; French, A. D., Diffraction from nonperiodic models of cellulose crystals. *Cellulose* **2012,** *19* (2), 319-336.

Chapter 3

Crystallinity-independent yet modification-dependent true density of nanocellulose

3.1 Abstract:

In materials science and crystallography, the true density is an important derived physical quantity of solids. In this chapter, the correlation of the true density of nanometer-wide fibrillar crystallites of cellulose with their purity, crystallinity, morphology, and surface functionality is investigated. In the single fibrils, all the cellulose molecules are uniaxiallly oriented. Thus, the true density indicates the molecular packing density in the single fibrils and is essential for the precise estimation of the volume fraction of cellulose in fibril-based composites or porous structures. It is demonstrated that the true density of fibrillar crystallites of cellulose is approximately 1.60 g/cm^3 irrespective of the biological origins of the cellulose (wood, cotton, or a tunicate) and the crystallinity. The true density is in fact independent of the dimension of the crystallites and the atomic conformation of the uniaxially oriented but non-crystalline molecules at the crystallite surface. In the single fibrils, all the cellulose molecules are densely packed from the crystalline core to the non-crystalline outermost regions. The value of 1.60 g/cm^3 remains unchanged even when the fibrils are dispersed through the wet disintegration process of "nanocellulose" production. In contrast, tailoring the surface functionality of the fibrils by oxidation and/or adsorption results in a substantial change in the true density up to 1.8 g/cm^3 or down to 1.3 g/cm^3. The true density of nanocellulose is indeed governed by the surface functionality and has a strong gradient in the fibril cross-sectional direction.

3.2 Introduction

Mass density ρ is a derived quantity defined as the mass per unit volume of a substance. In materials science, the density is a structural factor that is correlated with mechanical and thermal properties as well as other functionalities. Therefore, precise measurement of the density is critical and is considered a starting point in material research.

The density of solids can be classified into several types, including the true density and bulk density, depending on the method of measuring the volume. The bulk density is used for porous structures, and the volume is determined by the outer borders of structures. The true density is derived from the "true" volume of a solid, excluding the contributions of pores and surface roughness. The volume here is defined as the space occupied by the solid itself and includes the free volume for polymeric solids. The free volume is the atomic-scale gap left between assembled molecules, which is the space allowing the atoms to thermally vibrate and is distinguished from pores.[1]

The key to obtaining a reliable value in true density measurements is thus to precisely measure the true volume. Gas pycnometry is commonly adopted for this purpose. The volume of a solid in gas pycnometry is determined as the volume of gas displaced with the target solid in a volume-known sealed space under constant pressure using Boyle's law describing the volume–pressure relationship of an ideal gas (see Figure 3.1). The solids must not contain closed pores; particular attention is needed when the sample is prepared from melt or wet states through cooling or drying, respectively. The use of helium as the introducing gas is preferable because it exists as a monatomic gas and its interaction with solid surfaces is negligible. For hygroscopic samples, moisture adsorption is also a serious concern. In gas pycnometry, sample weight is separately measured, such that the true densities of hygroscopic samples are significantly overestimated unless attention is paid to the weight measurement.

Naturally occurring cellulose is a fibrous material, which inevitably forms pores in its practical uses as papers and clothes. The material properties of such structures scale with their porosity, and the porosity is estimated from the true density. Accurate measurement of the true density of cellulose is thus important. The reported values of the true density of cellulosic materials, however, vary within the range of 1.42–1.67 g/cm^3 even when measured by helium pycnometry[2-5]. This variability has been interpreted as resulting not only from the contributions of the purity and crystallinity of cellulose but also from experimental issues, such as closed-pore formation by dry agglomeration or overestimation of sample weight by moisture adsorption.

In the last decade, cellulose nanofibers (CNFs) have attracted attention as emerging sustainable materials with superior mechanical and thermal properties. CNFs are produced by wet disintegration of wood pulp, and the pulp is purified or chemically modified in advance[6-10]. Various CNFs with different morphologies, crystallinities, and surface functionalities can be manufactured, as described in General introduction. Structuring of such CNFs into various forms such as films and fibers is also possible. The properties of CNF structures scale with their porosity, and the true density of CNFs is thus considered indispensable information. However, the true density of CNFs with structural variety has not been analyzed in detail; the correlation of true density with the morphology, crystallinity, and surface functionality remain unknown.

In this chapter, the correlation of the true density of various celluloses with their purity, crystallinity, morphology, and surface functionality is investigated. The samples analyzed include wood pulps, cotton linters, a tunicin, and CNFs. Two types of CNFs with different morphology were prepared by wet disintegration of a pulp with high purity of cellulose, one of which was chemically modified in advance. The modification adopted here was TEMPO oxidation, and the oxidized products possessed a significant amount of carboxylate groups.[6, 11, 12] The counter ion of the carboxylates is a dominant factor determining their functionality, as mentioned in General introduction.[13, 14] Thus, the correlation of the true density with the counter-ion structure was also investigated. All the samples examined in this study are graphically summarized in Scheme 3.1. A series of samples were prepared by freeze drying from a 30% *tert*-butyl alcohol-containing wet state to form aerogel-like porous solids,[15] and the true densities of the samples were analyzed using helium pycnometry.

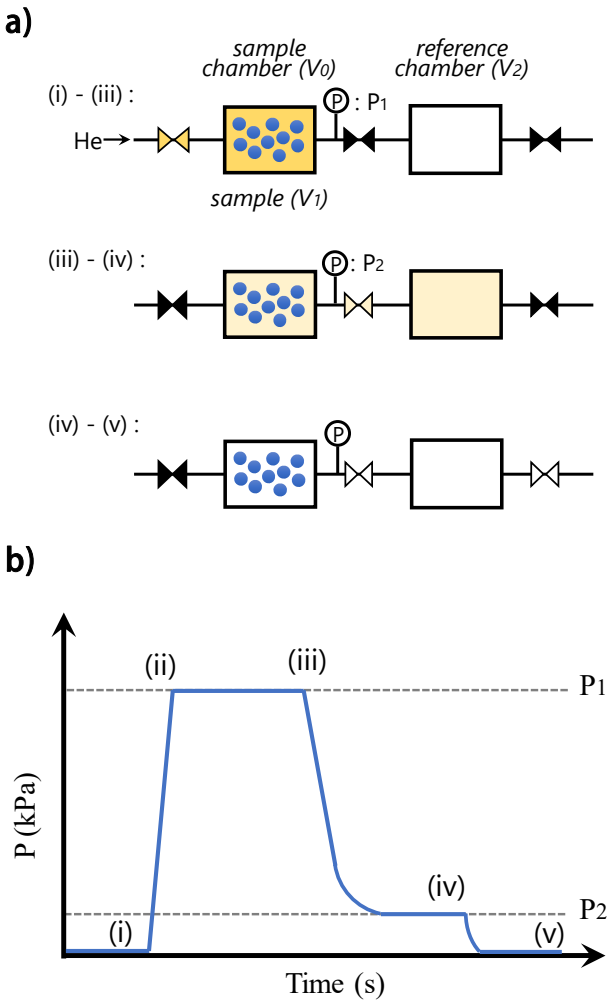

c) $$P_1(V_0 - V_1) = P_2(V_2 + V_0 - V_1)$$

$$V_1 = V_0 - \frac{P_2}{P_1 - P_2} \times V_2$$

$$\rho = \mathrm{m}V_1{}^{-1}$$

Figure 3.1. Schematic diagram of a) He pycnometer and b) a change in the pressure of He gas. c) Equation for the true density based on the Boyle's law of the volume-pressure relationship. The pycnometer consists of two chambers (sample and reference chambers). The two chambers are connected via a pressure gauge (P). In this system, the sample volume is determined from the difference between the pressure of a gas filled in the sample chamber (P_1) and the pressure of the gas diffused into both the chambers (P_2) by using the equation (c) where V_0 and V_2 are the internal volumes of the sample and reference chambers, respectively. The sample is placed into the sample chamber. The chamber is then filled with the gas (i–ii). After the pressure of the gas in the chamber reaches equilibrium (ii–iii), a valve separating the two chambers is opened (iii–iv). When the pressure of the gas in the system reaches the equilibrium, the gas is released (iv–v).

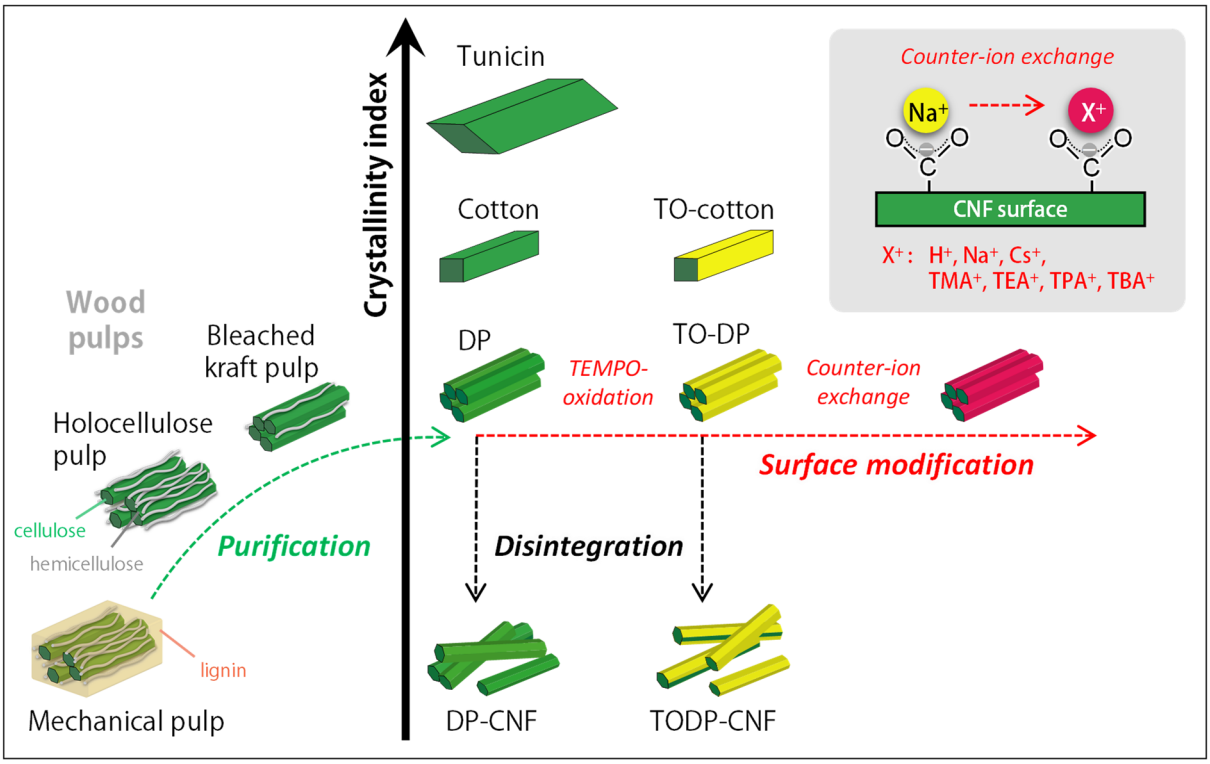

Scheme 3.1. Illustration of the purity, crystallinity, morphology, and surface functionality of the tested samples.

3.3 Experimental section

3.3.1 Materials

Five cellulosic samples were used as the starting materials: a softwood mechanical pulp, a softwood bleached kraft pulp, a softwood dissolving pulp [16], cotton linters, and a mantle of tunicate *Halocynthia roretzi*. The wood pulps were supplied by Nippon Paper Industries Co. Ltd., Japan, and had been kept in an undried state after pulping. The cotton linters were purchased from Advantec Toyo Co. Ltd., Japan. The tunicate mantle was supplied in an undried state by a domestic fish-processing company. The mechanical pulp was dewaxed with a mixture of acetone and water (9:1 by weight) before use. Holocellulose was prepared from the dewaxed pulp using the Wise method, and part of the holocellulose was alkali-treated with a 4% w/v NaOH solution according to the method described in a previous report.[17] Tunicate cellulose was purified from the mantle according to the procedure described in a previous report.[17] Part of the cotton linters and tunicate cellulose (0.1 g for each) were acid-hydrolyzed with a 1 M H_2SO_4 solution at 105 °C for 4 h. The residual solid hydrolysates were washed with distilled water by filtration. Amorphous cellulose was prepared from the cotton linters according to the method described in a previous report.[17] All the chemicals were of laboratory grade (FUJIFILM Wako Pure Chemical Corporation, Osaka, Japan) and used as received.

3.3.2 Cellulose content

The cellulose contents of the samples were determined by subtracting the lignin and hemicellulose contents from the sample weight. The lignin content was calculated from the Klason lignin content or Kappa number in the same manner described in the Experimental section in Chapter 2 (2.2.6. Cellulose content).[17] The hemicellulose content was calculated as the sum of the non-glucose sugars and the part of glucose corresponding to two thirds of mannose by weight. The non-glucose neutral sugars were measured according to the protocol described in the Experimental section in Chapter 2 (2.2.6. Cellulose content).[18] and the acidic sugars were quantified by electric conductivity titration.[19]

3.3.3 TEMPO-mediated oxidation.

The DP and cotton linters (2 g) were TEMPO-oxidized with NaClO addition of 2–10 mmol per gram of sample according to the method described in a previous report.[6] The oxidized

samples were treated with $NaBH_4$ (0.2 g) in water (200 mL) at pH 10 for 3 h to eliminate unstable aldehyde groups in the sample.[20] Hereafter, the TEMPO-oxidized DP and cotton are denoted as TO-DP and TO-cotton, respectively.

3.3.4 CNF preparation

Two types of CNF, DP-CNF and TODP-CNF, were prepared from the DP before and after TEMPO oxidation. The DP-CNF was prepared by passing a 0.1% w/w DP suspension (1 L) through a high-pressure water-jet system (HJP-25001, Sugino Machine) 100 times at 150 MPa. The TODP-CNF was prepared from a 0.1% w/w suspension of a TO-DP with carboxylate content of 1.7 mmol/g using a Microtec Physcotron NS-56 homogenizer equipped with a 20-mm-diameter shaft at 7500 rpm for 6 min, followed by sonication using a Nihon Seiki US-300T ultrasonic homogenizer equipped with a 18-mm-diameter tip at 70% output for 8 min.

3.3.5 Counter-ion exchange

The counter ions of the carboxy groups in the TO-DP (1.7 mmol/g) were exchanged with other inorganic or organic ions using the methods described in previous reports.[13, 21] The initial Na^+ ions were exchanged to H^+ or Cs^+ ions by soaking the TO-DP in a 0.1 M HCl or CsCl aqueous solution for 1 day, followed by washing with distilled water. Part of the protonated TO-DP (H^+) was then neutralized with four types of quaternary alkyl ammonium hydroxide: TMA, TEA, TPA, and TBA hydroxides, such that the carboxy groups were converted to the respective alkyl ammonium carboxylates.

3.3.6 Gravimetry

A series of the wet samples were freeze-dried after adding *tert*-butyl alcohol to be approximately 30 w/w% against their water content according to a method described in a previous report.[15] The freeze-dried sample (~60 mg) was placed into a weighing bottle and dried under vacuum at 105 °C for 3 h. After introducing dry air, the bottle was rapidly sealed and cooled in a desiccator for 20 min. The weight of the bottle containing the sample was measured with an analytical balance with an accuracy of ±0.0025 mg for 1 g (A&D, BM-20) in approximately 5 s at 23 °C and 50% relative humidity (see Figure 3.2). The weight of the empty bottle (13.028221 g) was also measured in the same manner. The sample weight was determined by subtracting the weight of the empty bottle from the total weight. The analytical balance was

placed on an anti-vibration table and was calibrated in advance. The measured weight of a dried sample was in good agreement with the weight estimated by thermogravimetric analysis (TGA) at 150 °C in a dry nitrogen atmosphere.

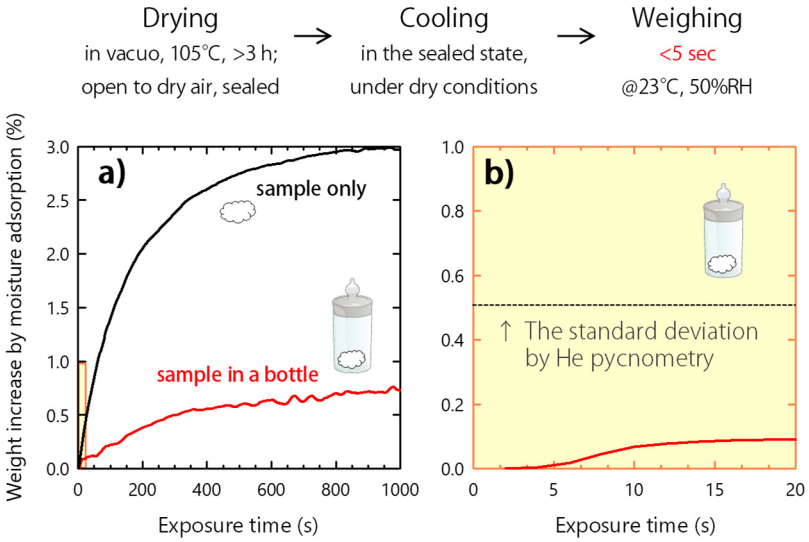

Figure 3.2. Weight increase by moisture absorption at 23 °C and 50% relative humidity.

3.3.7 Helium pycnometry

The true density was analyzed using a BELPycno helium pycnometer. The weight-measured sample (~60 mg) was placed into the chamber with a volume of 1 cm3 and exposed to a vacuum (~0.5 kPa). Then, helium gas was purged 30 times at 145 kPa. The density was measured at 25 ± 0.1 °C when no change of over 0.06 kPa for 30 s was observed. The measurement was repeated until a standard deviation of less than 0.5% was achieved for 30 consecutive measurements, and finally, the average of the last 5 measurements was taken as the true density of the sample.

3.3.8 CP/MAS ^{13}C NMR spectroscopy

CP/MAS ^{13}C NMR measurements were performed according to the method described in Chapter 2, Experimental section (2.2.8 CP/MAS ^{13}C NMR spectroscopy). Crystallinity Index (CI) value was calculated in the same way as calculation of CI-NA used in Chapter 2.

3.3.9 XRD

XRD measurements were performed according to the method described in the chapter 2, Experimental section (2.2.9 XRD). Crystal size value was calculated in the same way as calculation of CS-XI used in Chapter 2.

3.4 Results and discussion

3.4.1 Gravimetry

Supercritical CO_2 drying is known as the best method to prevent dry agglomeration of wet samples. However, the process of supercritical drying includes solvent-exchanging steps from water to liquid CO_2 via CO_2-miscible solvents such as alcohols or acetone. Its application to organic or dispersible samples thus requires attention to prevent extraction or flowing out of a part of the sample during the solvent-exchanging process. In the present study, a series of samples were directly prepared from 30% *tert*-butyl alcohol-containing pulp slurries or CNF dispersions by freeze drying without solvent exchanging.[15] The dried products are porous solids with high specific surface areas, which are structurally similar to aerogels from supercritical drying.[17] No significant difference in the true densities of the freeze-dried and supercritical-dried products of some wet samples was observed (< 0.01 g cm^{-3}, see Figure 3.3); in fact, the closed-pore formation by this specific freeze-drying was sufficiently suppressed as well as that by supercritical drying. The overestimation of the true density due to moisture adsorption was also suppressed to < 0.02% by careful monitoring of the weighing (Figure 3.2, see Gravimetry section for weighing); this difference is within the standard deviation for helium pycnometry (± 0.5% of the value, see Helium pycnometry section).

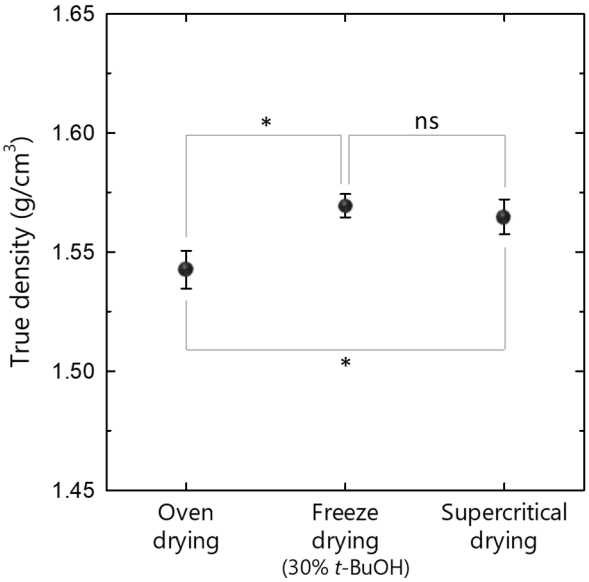

Figure 3.3. True densities of bleached kraft pulp dried using different methods. The asterisk * indicates significant differences between the values ($P < 0.05$), and ns indicates "not significant". The comparison was performed using one-way analysis of variance followed by the Holm–Sidak method.

3.4.2 Purity

Figure 1 shows the true density values of various pulps with different purity of cellulose (see Table 3.1 for the numerical data). Note here that the cellulose content is an estimate and has no accuracy on the order of 1%.

Table 3.1. The true density values and cellulose content of various cellulosic samples.

Sample	Cellulose content (%)	True density (g/cm^3)
MP	49	1.43 (±0.0072)
Holocellulose [22]	59	1.48 (±0.0066)
Alkali-treated holocellulose	68	1.52 (±0.0061)
KP	87	1.57 (±0.0047)
DP	96	1.59 (±0.0065)
Cotton linter	100	1.60 (±0.0070)
Acid-hydrolyzed cotton linter	100	1.60 (±0.0027)
Acid-hydrolyzed tunicate cellulose	100	1.60 (±0.0049)
Amorphous cellulose	100	1.43 (±0.0035)

The true density of the mechanical pulp with a cellulose content of approximately 50% (sample *i*) was 1.43 g/cm^3. As the cellulose content of the pulp increased to approximately 60% by delignification, the true density of the resulting holocellulose (sample *ii*) also increased to 1.48 g/cm^3. The subsequent alkali-extraction of a part of the hemicelluloses (sample *iii*) resulted in a further increase to 1.52 g/cm^3. The true densities of the bleached kraft pulp (sample *iv*) and DP (sample *v*) reached as high as 1.57 and 1.59 g/cm^3, respectively, depending on the cellulose content.

The trend in Figure 3.4 is reasonable because wood cellulose is crystalline, whereas other components such as lignin and hemicelluloses are amorphous. The true densities of the pulps should be positively correlated to their cellulose contents. The extrapolated values of the approximated line to both the vertical axes at cellulose contents of 0% and 100% are roughly 1.3 and 1.6 g/cm^3, respectively. These values imply the true densities of the mixture of lignin and hemicelluloses and of pure wood cellulose, respectively.

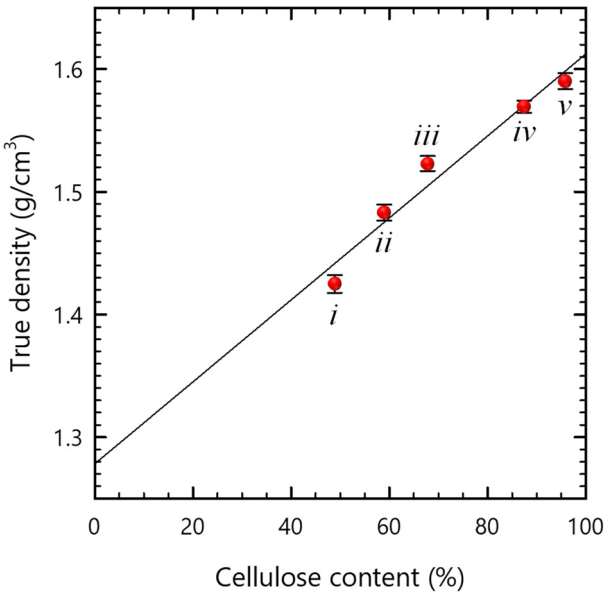

Figure 3.4. Relationship between true density values and cellulose content of wood pulps: i) mechanical pulp, ii) holocellulose pulp, iii) alkali-treated holocellulose pulp, iv) bleached kraft pulp, and v) DP.

3.4.3Crystallinity

Four samples of cellulose with different crystallinity were then analyzed: DP, cotton linter, and acid hydrolysates of cotton and a tunicin of *Halocynthia roretzi* (samples *v*, *vi*, *vii*, and v*iii*, respectively). The DP is a highly purified sample of wood cellulose, although it still contains approximately 4% hemicelluloses. The cotton linter is an ash-less pulp for filters and is chemically pure (cellulose content of ~100%). The cotton and tunicin were subjected to acid hydrolysis to isolate their crystallites. The CI values and Scherrer's crystal sizes of the samples were assessed using NMR spectroscopy and XRD, respectively (Figure 3.5.a,b). The CI values of the DP, cotton, and acid hydrolysates of cotton and tunicin were 48%, 63%, 65%, and 91%, respectively. Their Scherrer's crystal sizes were 4.2, 6.3, 6.5, and 10.0 nm, respectively, and increased in the same order as the CI values.

NMR analysis provides information on the conformation of the constituent carbon atoms of cellulose, (1→4)-*β*-glucan. The CI values were calculated as the signal ratios of the crystalline and non-crystalline C4 carbon atoms in the NMR spectra. These crystalline and non-crystalline atoms are often interpreted as those at the inner core and outermost regions of a crystallite, respectively. According to this interpretation, the CI represents the core-to-volume ratio of the crystallite. In contrast, the XRD analysis reflects the regularity of the molecular sheet stacking of cellulose, and the Scherrer's crystal sizes are a lower limit of the crystallite dimension, when the broadening from the beam size has not been taken into account[23]. The results shown in chapter 2 suggest that not only the inner but also the outermost molecules of a crystallite, the latter of which are regarded as being non-crystalline by NMR, are ordered in molecular sheet stacking to diffract X-rays, and are thus involved in the estimate of the Scherrer's crystal sizes.[17] In fact, NMR and XRD analyses provide different scales of information for the crystallinity of cellulose: the core-to-volume ratio and a dimensional index of the crystallite, respectively. Note that all the molecules in single crystallites of naturally occurring cellulose are uniaxially oriented irrespective of their crystallinity.[24]

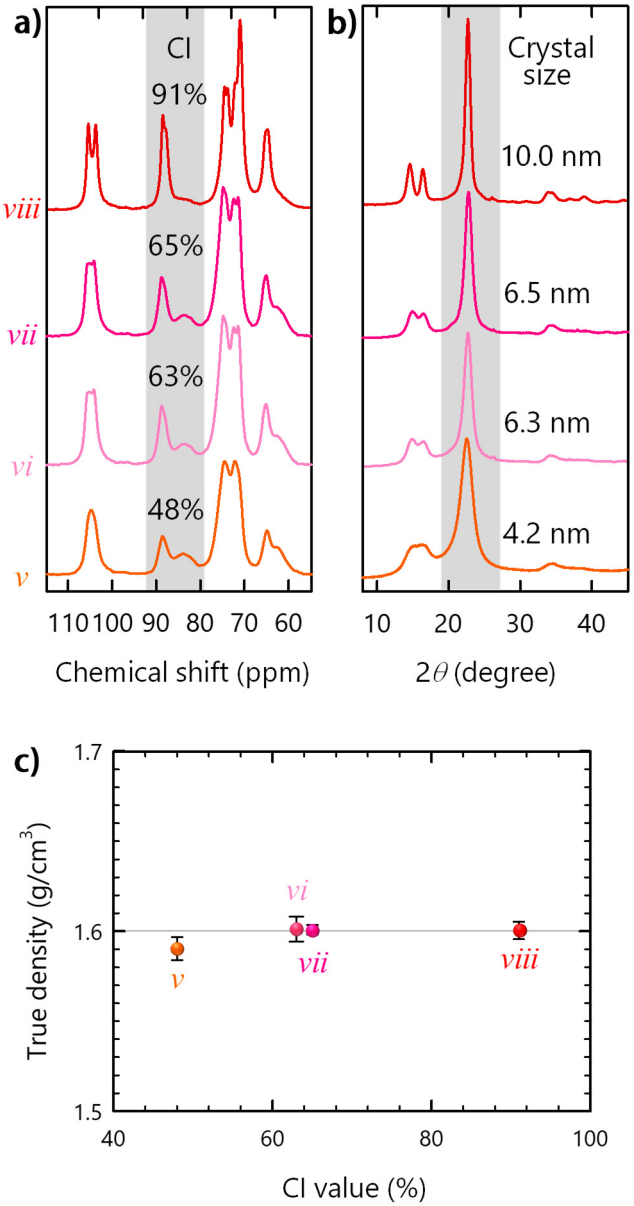

Figure 3.5. a) CP/MAS ^{13}C NMR spectra and b) XRD patterns of various celluloses with different crystallinity: v) DP, vi) cotton linter, vii) acid-hydrolyzed cotton linter, and viii) acid-hydrolyzed tunicin. c) Relationship between the true density and CI values. The grey line indicates the true density of 1.60 g/cm^3.

Figure 3.5.c shows the relationship between the true density and CI of the samples with different crystallinity (see Table 3.1 for the numerical data). It is significant that the true density of the cotton linter (sample *vi*) and the acid hydrolysates of cotton (sample *vii*) and tunicin (sample *viii*) were approximately 1.60 g/cm^3, irrespective of their CI. Considering that the CI represents the core-to-volume ratio of the crystallite, this finding indicates that even the surface molecules, including the carbon atoms with non-crystalline conformation, are packed in the same density as the inner crystalline molecules. In addition, the agreement of the true density for the cotton and its hydrolysate (samples *vi* and *vii*) indicates that the disordered region locally present along the fiber axis of cellulose crystallites represents a negligibly small fraction in the true density analysis.[25]

The value of 1.60 g/cm^3 is slightly lower than the true density of the ideal crystal of cellulose Iβ (~1.63 g/cm^3) at ambient temperature as defined by synchrotron XRD.[26] This discrepancy is perhaps due to the principal of measurement; XRD provides a weight-average structure of the crystal,[27] which should be denser than the number-average, molecular-packing structure estimated by helium pycnometry. The value for DP (sample *v*) was slightly lower at 1.59 g/cm^3, which may be explained by the ~4% residual hemicelluloses in the DP.

3.4.4. Surface oxidation

TEMPO oxidation was applied to the DP and cotton linter for surface modification. Figure 3.6 shows the relationship between the true density and carboxylate content of TO-DP and TO-cotton. The true density linearly increased with increasing carboxylate content in both cases. This tendency is reasonable because the conversion of the C6 primary hydroxy groups to sodium carboxylates by TEMPO oxidation increases the molecular weight of the anhydroglucose unit from 162 to 198 g/mol, and the oxidation occurs solely on the surfaces of cellulose crystallites (see Figure 3.7 for XRD profiles of the samples before and after oxidation).[11]

The straight line in Figure 3.6 represents the approximation of the function to all the plots and can be expressed by the following equation:

$$y = 0.063x + 1.594,$$

where y and x are the true density and carboxylate content of the sample, respectively. The R^2 value is as high as 0.98, and the plots fit well with the approximated line irrespective of the starting samples. The intercept is 1.594, which is an intermediate value between the true densities of the DP and cotton linter. The slope is 0.063, which is lower than the calculated slope of 0.072 assuming that the volume is unchanged by the increase in the molecular weight of cellulose by TEMPO oxidation. The oxidation of the C6 primary hydroxy groups to sodium carboxylates is thus accompanied by a slight increase in the volume.

The increase in the molecular weight is supported by the weight yield of the oxidized cellulose. The weight yield of the TO-DP with a carboxylate content of 1.7 mmol/g was roughly 110% relative to the weight of the starting DP, which is in good agreement with the theoretical weight gain resulting from the oxidation (~107%).

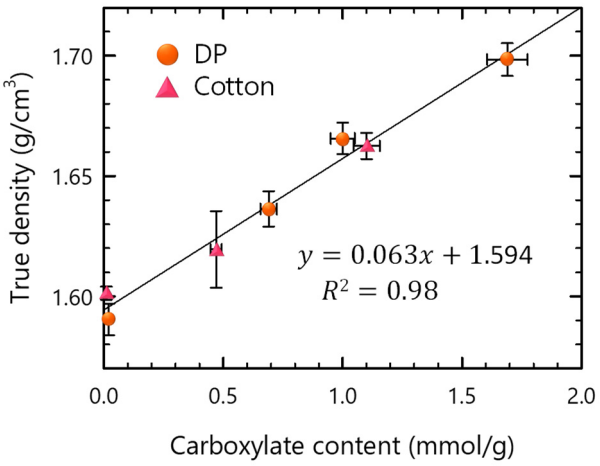

Figure 3.6. Relationship between the true density and carboxylate content of TO-DP and TO-cotton.

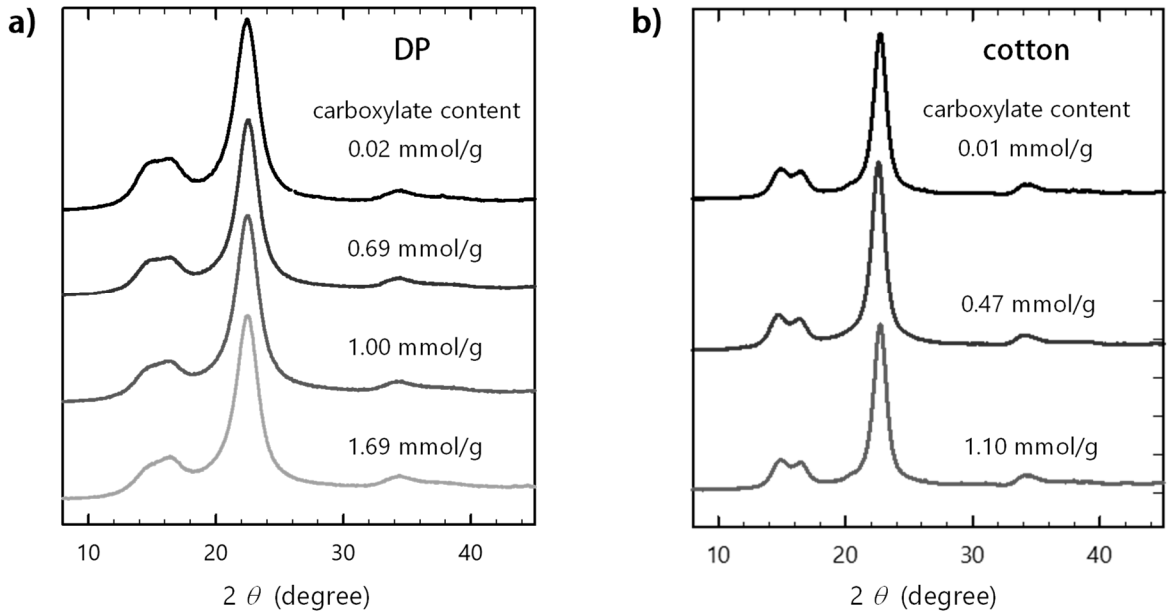

Figure 3.7. XRD patterns of the TEMPO-oxidized a) DP and b) cotton linters with different carboxylate contents.

3.4.5. Disintegration

Two types of CNF, DP-CNF and TODP-CNF, were prepared by wet disintegration of the DP and TO-DP with a carboxylate content of 1.7 mmol/g, respectively. The DP-CNF was composed of relatively thick and heterogeneous CNFs with diameters of approximately 3–20 nm (Figure 3.8a). In contrast, the TODP-CNF was composed of thin and homogeneous CNFs with diameters of approximately 3 nm (Figure 3.8b). Figure 3.9a shows the effect of the wet disintegration process on the true density. For both CNF samples, there were no significant changes from the true densities of the respective starting pulps.

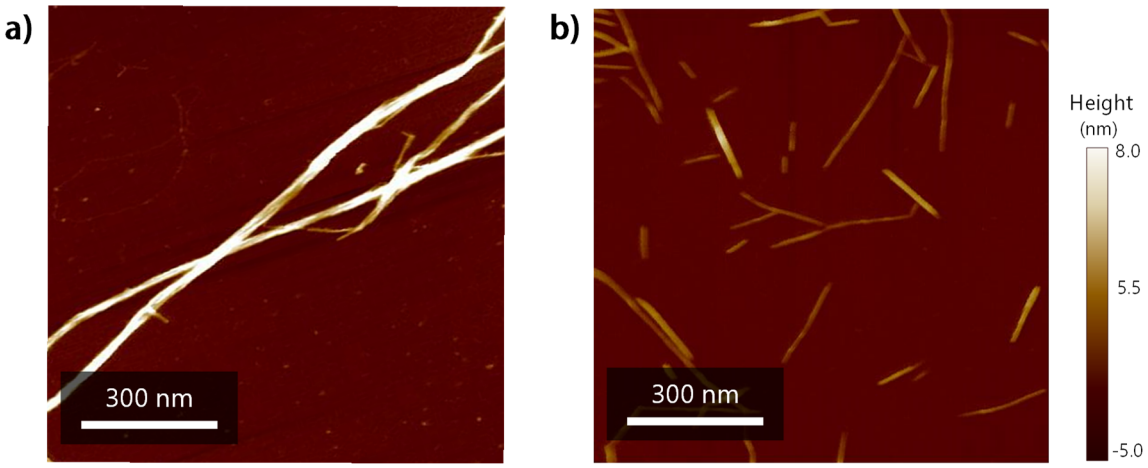

Figure 3.8. Atomic force microscopy images of a) DP-CNF and b) TODP-CNF.

The NMR spectra in Figure 3.9b,c show the changes in the crystallinity of cellulose resulting from wet disintegration. The signals of the crystalline and non-crystalline C4 carbon atoms appear at approximately 89 and 84 ppm, respectively. Their signal area ratio is defined as the CI (see the section "Crystallinity"). The DP has a CI value of 50% and sustained its CI at 48% even after being sufficiently oxidized. The CI of each pulp remarkably decreased when the pulp was disintegrated into CNFs. The decrease in the CI depended on the degree of disintegration, and the thick DP-CNFs and thin TODP-CNFs had the CI values of 38% and 22%, respectively. This phenomenon can be interpreted as resulting from the increase in the specific surface area by disintegration,[17] considering that the CI represents the core-to-volume ratio of the crystallite. Here, the crystallite is identical to the few-nanometer-wide crystalline fibrils histologically defined as "cellulose microfibrils". The results shown in chapter 2 indicate that these fibrils are closely bundled in a pulp fiber and that the cellulose molecules at the interface between bundled fibrils or at the surface of the individual fibrils are partly crystalline and become non-crystalline when the fibrils disperse as CNFs.[17] In fact, the decrease in the CI by wet disintegration represents the conformational change of the constituent carbon atoms at the crystallite surface to the non-crystalline state.

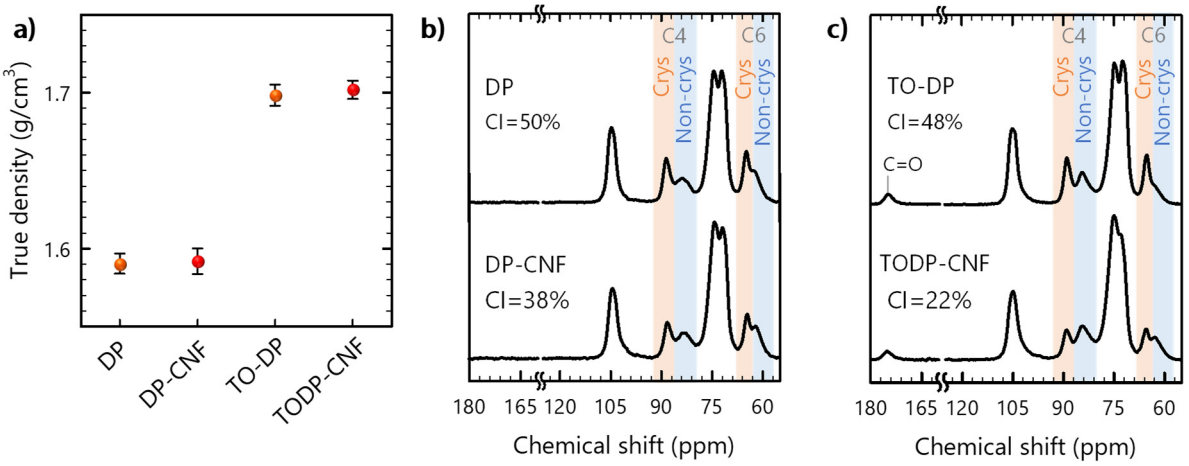

Figure 3.9. a) True density and b,c) CP/MAS ^{13}C NMR spectra of DP, DP-CNF, TO-DP, and TODP-CNF.

The series of results presented in Figure 3.9 show that the true density of CNFs is independent of the decrease in the CI resulting from the process of wet disintegration, leading to the same conclusion as that in Figure 3.5: the surface molecules including the carbon atoms with non-crystalline conformation are packed with the same density as the inner crystalline molecules. The conformational change of the C4 carbon atoms is accompanied by that of the C6 carbon atoms from the crystalline "trans–gauche (*tg*)" to non-crystalline "gauche–trans (*gt*)" or "gauche–gauche (*gg*)" C6–O6 bond configuration against the C5–O5/C4–C5 bonds (see the C6 region in Figure 3.9b,c).[28, 17] Although the C6 position is exocyclic and likely to be dominant in the true density, its conformational change was buried in the true density value.

Note again that all the molecules in the single crystallites are uniaxially oriented irrespective of their CI values. For reference, a truly amorphous sample of randomly packed cellulose molecules, which was prepared from the cotton linter through a dissolution–regeneration process (see Materials section), had a significantly lower true density of 1.43 g/cm^3.

3.4.6. Counter-ion exchange

CNFs are often post-modified to tailor their functionality in addition to the TEMPO oxidation and other pulp pretreatments. One of the simplest post-modifications is to exchange the counter ions of the surface ionic groups. Three inorganic (H, Na, Cs) and four organic [alkyl ammoniums: tetramethylammonium, tetraethylammonium (TEA), tetra-*n*-propylammonium (TPA), tetra-*n*-butylammonium (TBA)] cations were thus coupled with the surface carboxylate anions of the TO-DP (see Figures 3.10 and 3.11 for FTIR and XRF analyses of the products, respectively).

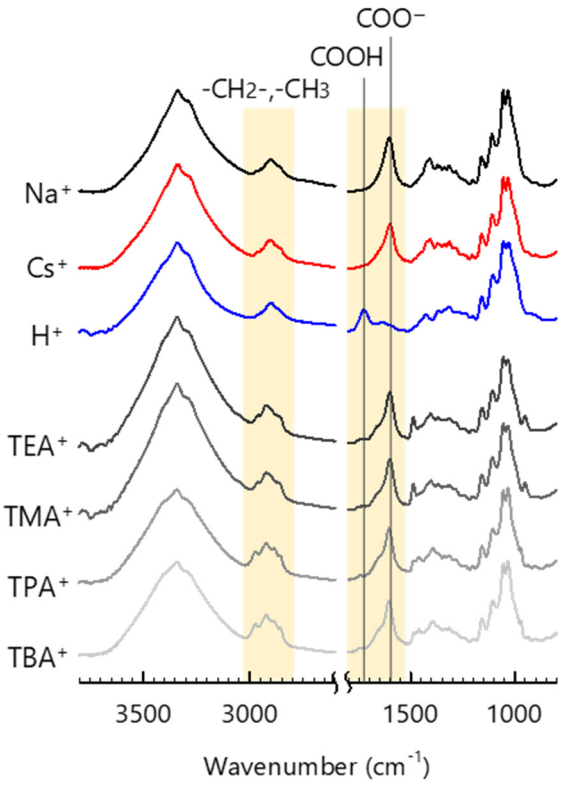

Figure 3.10. FTIR spectra of the TEMPO-oxidized DP with different carboxylate counter-ions.

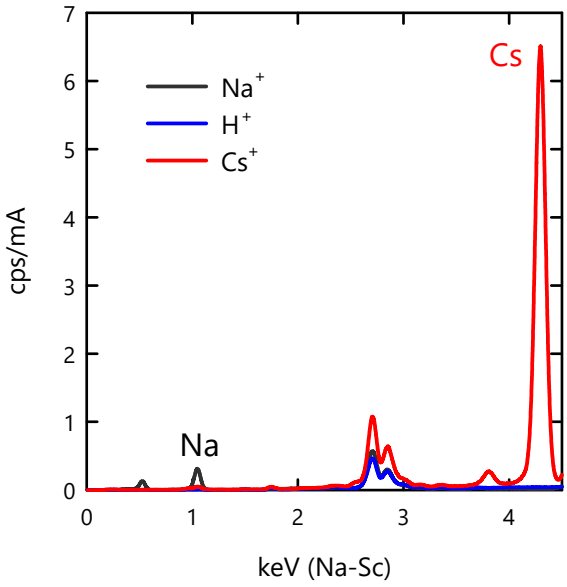

Figure 3.11. XRF spectra of the TEMPO-oxidized DP with inorganic conter-ions.

Figure 3.12 shows the true density correlations with these counter-ion structures. For inorganic ions, the true density increased in the order of H < Na < Cs ions (Figure 3.12a). This tendency is reasonable considering that the atoms differ greatly in weight but little in size;[29] the atomic weights of H, Na, and Cs are 1, 23, and 133, respectively, whereas the effective packing radii of these elements in the coupled states are estimated to be 0.11 nm (exposed radius in covalent bond), 0.095 nm, and 0.169 nm (bare-ion radius), respectively.[30] It is interesting here that the true density of the TO-DP-bearing cesium carboxylate groups reaches as high as nearly 1.8 g/cm^3.

In contrast, the true density largely decreased below 1.3 g/cm^3 for organic ions in the order of TMA > TEA > TPA > TBA, showing an inverse correlation with the alkyl chain length of the ammoniums (Figure 3.12b). This tendency can be interpreted as an increase in the free volume by the alkyl chains. The formula weights of TMA, TEA, TPA, and TBA are 74, 130, 186, and 242, respectively, and their ion radii are estimated to be 0.35, 0.40, 0.45, and 0.49 nm, respectively.[31]

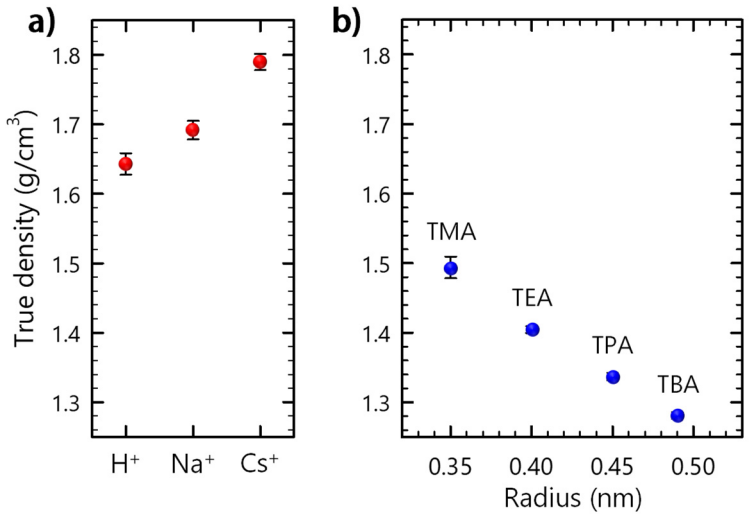

Figure 3.12. True density of TO-DP with a) inorganic (H^+, Na^+, Cs^+) and b) organic (TMA^+, TEA^+, TPA^+, TBA^+) counter ions.

3.5 Conclusions

The correlation of the true density of various celluloses with their purity, crystallinity, morphology, and surface functionality was investigated, leading to the following conclusions: 1) The true density of wood pulps is approximately linearly correlated to their cellulose purity. 2) The true density values of pure native celluloses, such cotton and tunicin, are approximately 1.60 g/cm^3 irrespective of the crystallinity. 3) The true density is unchanged during the process of wet disintegration from a pulp to CNFs, although the CI is significantly decreased. 4) The true density of TEMPO-oxidized CNFs is also linearly correlated to their carboxylate content and increases up to approximately 1.7 g/cm^3. 5) The counter-ion exchanging of the carboxylates is accompanied by a substantial change in the true density of the CNF, up to approximately 1.8 g/cm^3 or down to approximately 1.3 g/cm^3. The true density of TEMPO-oxidized CNFs is indeed governed by the surface functionality and has a strong gradient in the fiber cross-sectional direction.

3.6 References

1. White, R. P.; Lipson, J. E. G., Polymer Free Volume and Its Connection to the Glass Transition. *Macromolecules* **2016,** *49* (11), 3987-4007.

2. Stamm, A. J.; Hansen, L. A., The bonding force of cellulosic materials for water (from specific volume and thermal data). *J Phys Chem-Us* **1937,** *41* (7), 1007-1016.

3. Ek, R.; Gustafsson, C.; Nutt, A.; Iversen, T.; Nystrom, C., Cellulose powder from Cladophora sp. algae. *J Mol Recognit* **1998,** *11* (1-6), 263-265.

4. Hervy, M.; Santmarti, A.; Lahtinen, P.; Tammelin, T.; Lee, K.-Y., Sample geometry dependency on the measured tensile properties of cellulose nanopapers. *Materials & Design* **2017,** *121*, 421-429.

5. Rowe, R. C.; Sheskey, P.; Quinn, M., *Handbook of pharmaceutical excipients*. Libros Digitales-Pharmaceutical Press: 2009.

6. Saito, T.; Nishiyama, Y.; Putaux, J. L.; Vignon, M.; Isogai, A., Homogeneous suspensions of individualized microfibrils from TEMPO-catalyzed oxidation of native cellulose. *Biomacromolecules* **2006,** *7* (6), 1687-1691.

7. Paakko, M.; Ankerfors, M.; Kosonen, H.; Nykanen, A.; Ahola, S.; Osterberg, M.; Ruokolainen, J.; Laine, J.; Larsson, P. T.; Ikkala, O.; Lindstrom, T., Enzymatic hydrolysis combined with mechanical shearing and high-pressure homogenization for nanoscale cellulose fibrils and strong gels. *Biomacromolecules* **2007,** *8* (6), 1934-1941.

8. Henriksson, M.; Henriksson, G.; Berglund, L. A.; Lindström, T., An environmentally friendly method for enzyme-assisted preparation of microfibrillated cellulose (MFC) nanofibers. *European Polymer Journal* **2007,** *43* (8), 3434-3441.

9. Wagberg, L.; Decher, G.; Norgren, M.; Lindstrom, T.; Ankerfors, M.; Axnas, K., The build-up of polyelectrolyte multilayers of microfibrillated cellulose and cationic polyelectrolytes. *Langmuir* **2008,** *24* (3), 784-795.

10. Noguchi, Y.; Homma, I.; Matsubara, Y., Complete nanofibrillation of cellulose prepared by phosphorylation. *Cellulose* **2017,** *24* (3), 1295-1305.

11. Saito, T.; Hirota, M.; Tamura, N.; Kimura, S.; Fukuzumi, H.; Heux, L.; Isogai, A., Individualization of Nano-Sized Plant Cellulose Fibrils by Direct Surface Carboxylation Using TEMPO Catalyst under Neutral Conditions. *Biomacromolecules* **2009,** *10* (7), 1992-1996.

12. Saito, T.; Isogai, A., TEMPO-mediated oxidation of native cellulose. The effect of oxidation conditions on chemical and crystal structures of the water-insoluble fractions. *Biomacromolecules* **2004,** *5* (5), 1983-1989.

13. Shimizu, M.; Saito, T.; Isogai, A., Bulky quaternary alkylammonium counterions enhance the nanodispersibility of 2,2,6,6-tetramethylpiperidine-1-oxyl-oxidized cellulose in diverse solvents. *Biomacromolecules* **2014,** *15* (5), 1904-1909.

14. Okita, Y.; Fujisawa, S.; Saito, T.; Isogai, A., TEMPO-oxidized cellulose nanofibrils dispersed in organic solvents. *Biomacromolecules* **2011,** *12* (2), 518-522.

15. Nemoto, J.; Saito, T.; Isogai, A., Simple Freeze-Drying Procedure for Producing Nanocellulose Aerogel-Containing, High-Performance Air Filters. *ACS Appl Mater Interfaces* **2015,** *7* (35), 19809-19815.

16. Jonoobi, M.; Oladi, R.; Davoudpour, Y.; Oksman, K.; Dufresne, A.; Hamzeh, Y.; Davoodi, R., Different Preparation Methods and Properties of Nanostructured Cellulose from Various Natural Resources and Residues: a Review. *Cellulose* **2015,** *22*, 935.

17. Daicho, K.; Saito, T.; Fujisawa, S.; Isogai, A., The Crystallinity of Nanocellulose: Dispersion-Induced Disordering of the Grain Boundary in Biologically Structured Cellulose. *Acs Applied Nano Materials* **2018,** *1* (10), 5774-5785.

18. Ono, Y.; Tanaka, R.; Funahashi, R.; Takeuchi, M.; Saito, T.; Isogai, A., SEC–MALLS analysis of ethylenediamine-pretreated native celluloses in LiCl/N,N-dimethylacetamide: softwood kraft pulp and highly crystalline bacterial, tunicate, and algal celluloses. *Cellulose* **2016,** *23* (3), 1639-1647.

19. Kuramae, R.; Saito, T.; Isogai, A., TEMPO-oxidized cellulose nanofibrils prepared from various plant holocelluloses. *Reactive & Functional Polymers* **2014,** *85*, 126-133.

20. Takaichi, S.; Saito, T.; Tanaka, R.; Isogai, A., Improvement of nanodispersibility of oven-dried TEMPO-oxidized celluloses in water. *Cellulose* **2014,** *21* (6), 4093-4103.

21. Shimizu, M.; Saito, T.; Isogai, A., Water-resistant and high oxygen-barrier nanocellulose films with interfibrillar cross-linkages formed through multivalent metal ions. *Journal of Membrane Science* **2016,** *500*, 1-7.

22. Tanpichai, S.; Quero, F.; Nogi, M.; Yano, H.; Young, R. J.; Lindstrom, T.; Sampson, W. W.; Eichhorn, S. J., Effective Young's modulus of bacterial and microfibrillated cellulose fibrils in fibrous networks. *Biomacromolecules* **2012,** *13* (5), 1340-9.

23. Elazzouzi-Hafraoui, S.; Nishiyama, Y.; Putaux, J. L.; Heux, L.; Dubreuil, F.; Rochas, C., The shape and size distribution of crystalline nanoparticles prepared by acid hydrolysis of native cellulose. *Biomacromolecules* **2008,** *9* (1), 57-65.

24. Koyama, M.; Helbert, W.; Imai, T.; Sugiyama, J.; Henrissat, B., Parallel-up structure evidences the molecular directionality during biosynthesis of bacterial cellulose. *Proc Natl Acad Sci U S A* **1997,** *94* (17), 9091-9095.

25. Nishiyama, Y.; Kim, U. J.; Kim, D. Y.; Katsumata, K. S.; May, R. P.; Langan, P., Periodic disorder along ramie cellulose microfibrils. *Biomacromolecules* **2003,** *4* (4), 1013-1017.

26. Langan, P.; Sukumar, N.; Nishiyama, Y.; Chanzy, H., Synchrotron X-ray structures of cellulose Iβ and regenerated cellulose II at ambient temperature and 100 K. *Cellulose* **2005,** *12* (6), 551-562.

27. 理学電機株式会社 X 線研究所, *X 線回折ハンドブック*. 4 版 ed.; 理学電機: 2003; p ii, 157, 86p.

28. Yang, H.; Wang, T.; Oehme, D.; Petridis, L.; Hong, M.; Kubicki, J., Structural factors affecting 13C NMR chemical shifts of C4 and C6 of cellulose: a computational study. *Abstracts of Papers of the American Chemical Society* **2017,** *253* (1), 23-36.

29. Ashby, M. F.; Shercliff, H.; Cebon, D., *Materials: Engineering, Science, Processing and Design*. Elsevier Science: 2013.

30. Israelachvili, J. N., *Intermolecular and surface forces*. Academic press: 2015.

31. Robinson, R. A.; Stokes, R. H., *Electrolyte solutions*. Courier Corporation: 2002.

本章の内容は学術誌論文として投稿する計画があるため公表できない。
5 年以内に投稿予定。

本章の内容は学術誌論文として投稿する計画があるため公表できない。
5 年以内に投稿予定。

本章の内容は学術誌論文として投稿する計画があるため公表できない。
5 年以内に投稿予定。

本章の内容は学術誌論文として投稿する計画があるため公表できない。
5 年以内に投稿予定。

本章の内容は学術誌論文として投稿する計画があるため公表できない。
5 年以内に投稿予定。

本章の内容は学術誌論文として投稿する計画があるため公表できない。
5 年以内に投稿予定。

本章の内容は学術誌論文として投稿する計画があるため公表できない。
5 年以内に投稿予定。

本章の内容は学術誌論文として投稿する計画があるため公表できない。
5 年以内に投稿予定。

本章の内容は学術誌論文として投稿する計画があるため公表できない。
5 年以内に投稿予定。

本章の内容は学術誌論文として投稿する計画があるため公表できない。

5 年以内に投稿予定。

本章の内容は学術誌論文として投稿する計画があるため公表できない。
5 年以内に投稿予定。

本章の内容は学術誌論文として投稿する計画があるため公表できない。
5 年以内に投稿予定。

本章の内容は学術誌論文として投稿する計画があるため公表できない。
5 年以内に投稿予定。

本章の内容は学術誌論文として投稿する計画があるため公表できない。
5 年以内に投稿予定。

本章の内容は学術誌論文として投稿する計画があるため公表できない。
5 年以内に投稿予定。

本章の内容は学術誌論文として投稿する計画があるため公表できない。
5 年以内に投稿予定。

本章の内容は学術誌論文として投稿する計画があるため公表できない。
5 年以内に投稿予定。

本章の内容は学術誌論文として投稿する計画があるため公表できない。
5 年以内に投稿予定。

本章の内容は学術誌論文として投稿する計画があるため公表できない。
5 年以内に投稿予定。

本章の内容は学術誌論文として投稿する計画があるため公表できない。
5 年以内に投稿予定。

本章の内容は学術誌論文として投稿する計画があるため公表できない。
5 年以内に投稿予定。

本章の内容は学術誌論文として投稿する計画があるため公表できない。
5 年以内に投稿予定。

本章の内容は学術誌論文として投稿する計画があるため公表できない。
5 年以内に投稿予定。

本章の内容は学術誌論文として投稿する計画があるため公表できない。
5 年以内に投稿予定。

Appendix

Cross-polarization dynamics and conformational study of variously sized cellulose crystallites using solid-state ^{13}C NMR

A.1 Introduction

^{13}C CP/MAS NMR spectroscopy provides information on the conformation of the constituent carbon atoms of a system. Use of this NMR technique promotes a greater understanding of the structural features and dynamics of solid cellulose [1-6]. In the NMR spectra, the C4 and C6 carbon atoms are distinguishable into crystalline and noncrystalline signals [7], which have been attributed to the atoms at the core and surface regions of a crystallite, respectively. In particular, the signal ratio of the C4 crystalline and noncrystalline phases has been used as the crystallinity index (CI) value of CNF [8]; even for CNFs with high crystallinities, the contribution of the surface chains to the CI value is significant, due to the high surface-to-core ratios. To calculate the CI value, it is necessary to examine the dependence of the contact time (CT) for CP on the signal intensity and set the optimum CT to maximize the signal intensity [8-10]. However, the dependence has not been well investigated for cellulose samples with different crystallinities, even though the crystallinity could influence the CP dynamics.

In this appendix, the CT was optimized for the evaluation of the CI value of cellulose with different crystallinities. The crystallinity of the cellulose samples was finely tuned by changing the crystal size from a few nanometers to tens of nanometers. The NMR spectra were recorded at various CTs (0.1 to 10 ms), and the dependency of the CT to the signal intensity of the C4 crystalline and noncrystalline phases was investigated. At an optimized CT, the structural change via surface modification of native cellulose by TEMPO-oxidation was also analyzed from the NMR spectra of the C6 region.

A.2 Experimental

A.2.1 Materials

Five cellulosic samples were used as the starting materials: a softwood dissolving pulp (DP), two types of TEMPO-oxidized pulps with different carboxylate contents, cotton linters, and a mantle of tunicate *Halocynthia roretzi*. The DP and one TEMPO-oxidized pulp (carboxylate content: 1.2 mmol/g) was supplied by Nippon Paper Industries Co. Ltd., (Tokyo, Japan). The other TEMPO-oxidized pulp (carboxylate content: 1.8 mmol/g) was supplied by DKS Co. Ltd., Kyoto, Japan. The cotton linters were purchased from Advantec Toyo Co. Ltd., Tokyo, Japan. The tunicate mantle was supplied in an undried state by a domestic fish-processing company. Tunicate cellulose was purified from the mantle according to the procedure described in a previous report [11]. The cotton linters and tunicate cellulose (0.1 g for each) were acid-hydrolyzed with a 2 M HCl solution at 105 °C for 4 h. The residual solid hydrolysates were washed with distilled water by filtration. Amorphous cellulose was prepared from the cotton linters according to the method described in a previous report [12]. All the chemicals were of laboratory grade (FUJIFILM Wako Pure Chemical Corporation, Osaka, Japan) and used as received.

A.2.2 Sample preparation

The DP (1 g) was TEMPO-oxidized with NaClO addition (10 mmol per gram of sample) according to the method described in a previous report [13]. The oxidized samples were treated with $NaBH_4$ (0.1 g) in water (100 mL) at pH 10 for 3 h to eliminate unstable aldehyde groups in the sample. The resulting pulp is from here on referred to as TEMPO-oxidized DP (TO-DP). The carboxylate content of TO-DP was determined to be 1.6 mmol/g. Some of the 0.1% w/w suspension of the oxidized samples were mechanically treated by using a Microtec Physcotron NS-56 homogenizer (Microtec Co., Ltd. Chiba, Japan) equipped with a 20-mm diameter shaft at 7500 rpm for 6 min, followed by sonication using a Nihon Seiki US-300T ultrasonic homogenizer equipped with a 26-mm diameter tip at 70% output for 8 min. The resulting sample is from here on referred to as TEMPO-oxidized cellulose nanofiber (TO-CNF). All the

samples were freeze-dried from the wet state, containing 30% w/w *tert*-butyl alcohol, to prevent dry agglomeration [14].

A.2.3 XRD.

XRD measurements were performed according to the method described in the chapter 2, EXPERIMENTAL SECTION (2.2.9 XRD). Crystal size value was calculated in the same way as calculation of CS-XI used in the chapter 2.

A.2.4 CP/MAS ^{13}C NMR spectroscopy.

The samples conditioned at 23 °C and 50% relative humidity were packed into air-tight tubes and analyzed using CP/MAS ^{13}C NMR spectroscopy. The reason the dried stay sample was used for the analyses is described in a paper reported by Heux *et. al* [10]. The CP/MAS ^{13}C NMR measurements were performed using a JEOL JNM-ECAII 500 spectrometer (JEOL Ltd., Tokyo, Japan) equipped with a 3.2-mm HXMAS probe and ZrO_2 rotors at 125.77 MHz for ^{13}C. The samples were spun at 15,000 Hz and the spectra were obtained with 0.1–10 ms CT and a 5-s relaxation delay. The CI value was calculated from the integral ratio of the signals in the region of 93–86 and 86–80 ppm, corresponding to the crystalline and noncrystalline C4 carbon atoms of cellulose, respectively, and any fitting function was not used for peak separation. This is because it is difficult to unambiguously fix the fitting factor such as the peak position, function, and number in the NMR spectra of all the samples and CP conditions. Note here that the peak separation in this appendix is different from that performed in other chapters.

A.3 Results and discussion

A.3.1 C4-based CI value

The NMR spectra of the samples with different crystal sizes were recorded at various CTs (0.1–10 ms). The Scherrer crystal sizes of the acid hydrolysates of tunicin and cotton, DP, TO-DP, and TO-CNF were 10.0, 6.5, 4.0, 3.6, and 2.0 nm, respectively. For all the samples, the intensity of the C4 region changed depending on the CT (Figure A.1a). Furthermore, the spectra became sharper and split into several peaks as the crystal size increased, which is clearly visible in the spectra of the tunicate cellulose. These results can be interpreted as the crystallographic inequivalence of the glycosidic unit, and the resolution is improved when the crystal size is

larger [2]. In the case of the crystalline atoms in small crystallites or the noncrystalline atoms, the structural heterogeneity might be too large to produce clearly resolved peaks in the spectrum.

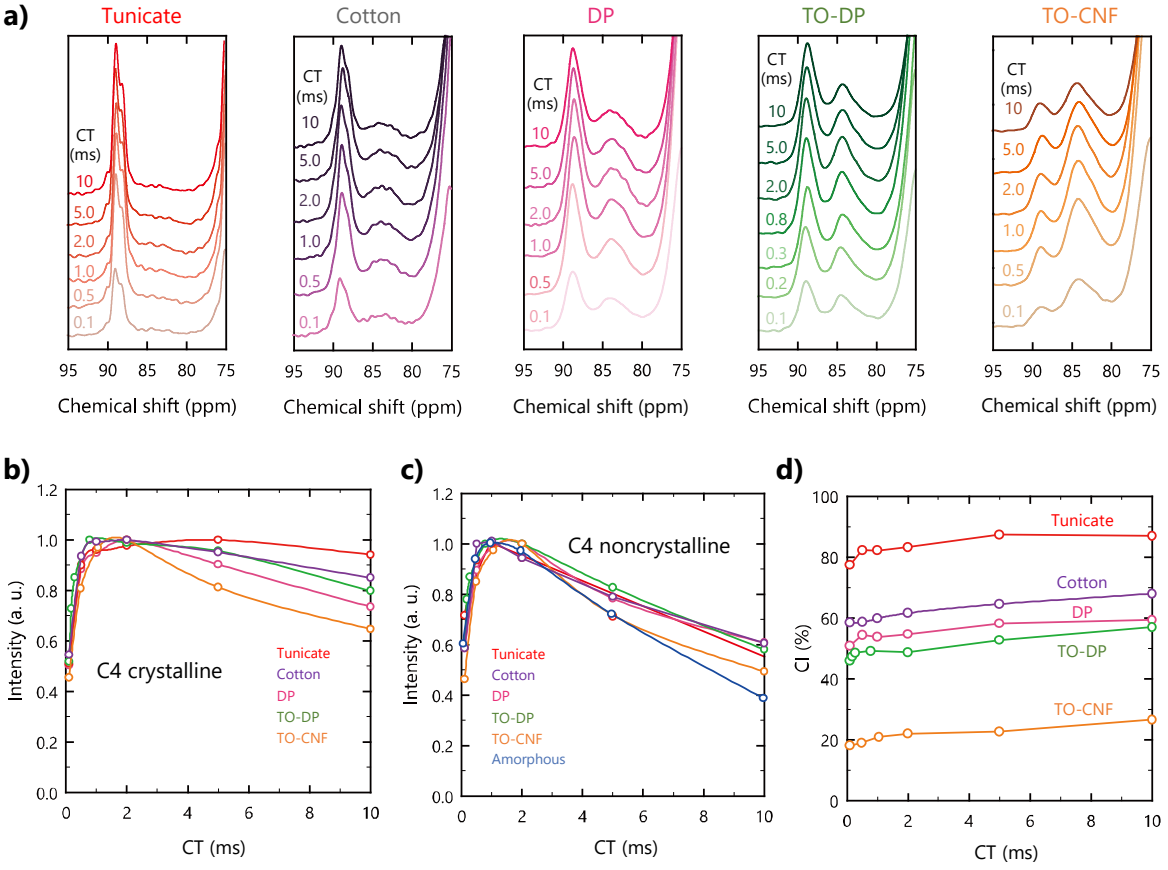

Figure A.1. a) NMR spectra of a series of samples at several CTs. The Scherrer crystal sizes of the acid hydrolysates of tunicin and cotton, DP, TO-DP, and TO-CNF were 10, 6.5, 4.0, 3.6, and 2.0 nm, respectively. **b)** Dependency of CT on the signal intensity corresponding to the C4 crystalline region. **c)** Dependency of CT on the signal intensity corresponding to the C4 noncrystalline region. **d)** Dependency of CT on the CI values.

The dependency of the CT to the signal intensities of both the C4 crystalline and noncrystalline regions was then analyzed. Figure A.1b and A.1c show the CP curves for the C4 crystalline and noncrystalline regions, respectively. The signal intensities were normalized at the maximum intensity for each carbon. In both regions, all the signal intensities were rapidly increased at the initial stage before reaching a maximum. The maximum of these intensities was at approximately 1–2 ms CT, irrespective of the crystal size. This region was in accordance with the reported CT as a preferable time for evaluation of the CI value of cellulosic materials [10, 15, 16].

At the initial increase in the C4 crystalline and noncrystalline regions, there was no significant difference in the trend and slope (Figure A.1b and A.1c). The initial increase mainly reflects the efficiency of magnetization transfer from the ^{1}H spin reservoir to the ^{13}C spin, described by the time constant of T_{CH}. In general, a rigid structure has a smaller T_{CH} than a nonrigid system, although the chemical structure may be the same. Therefore, this result indicates that the rigidity of the C4 carbons is similar in the time scale represented by the T_{CH} relaxation, regardless of the crystal size.

In contrast, the decay in the C4 regions showed different behavior depending on the crystal size. The decay of each sample was steeper in the noncrystalline region than that in the crystalline region. In the crystalline region, the decay slope became steeper with a decrease in the crystal size (Figure A.1b). The decay at the longer CT reflects the relaxation of the ^{1}H and ^{13}C spins in the rotating frame [$T_{1\square}$ (H) and $T_{1\square}$ (C), respectively], which are related to molecular mobility. Thus, the decay trends shown in Figure A.1b indicate that the crystalline region of large crystallites, such as the tunicate cellulose, have lower molecular mobility.

However, the smaller crystallites exhibited the higher mobility, even in the crystalline region, because of the large contribution of the crystallite surface. Furthermore, the similar trend was visible in the decay of the noncrystalline region; the decay was faster with a decrease in the crystal size (Figure A.1c). Indeed, the conformational heterogeneity is present in both the crystalline and noncrystalline regions. It has been reported that part of the molecules that exist close to the surface sit in a noncrystalline conformation even in the interior of the microfibril [17, 18].

Another possibility of the existence of heterogeneity is also conceivable. As shown in the results in chapter 2, the crystalline C4 signal decreased when the bundled fibers dispersed as microfibrils and, correspondingly, the noncrystalline signal increased [12]. Indeed, the cellulose molecules at the interface between bundled fibrils or at the surface of the microfibrils are partially crystallized. This interface has been regarded as an inaccessible surface, where solvent molecules cannot penetrate. It has been proposed that the NMR signal due to the molecules at the inaccessible surface appear in the noncrystalline region [19]. Taking these phenomena into account, some of the inaccessible molecules at the bundled interfaces are probably occupied in

the crystalline region of the NMR spectra rather than in the noncrystalline region, thus causing the structural heterogeneity.

The CP curve of the amorphous cellulose sample, whose molecular sheet stacking and the atomic conformation are disordered and noncrystalline, respectively [20], was also compared with other cellulosic samples (Figure A.1c). The initial increase and the maximum were similar to that observed for the C4 noncrystalline carbons in other samples. The decay slope was slightly steeper than that of TO-CNF but this difference is somewhat minimal. These results suggest that the glycoside linkage may be restricted even in the randomly packed cellulose molecules.

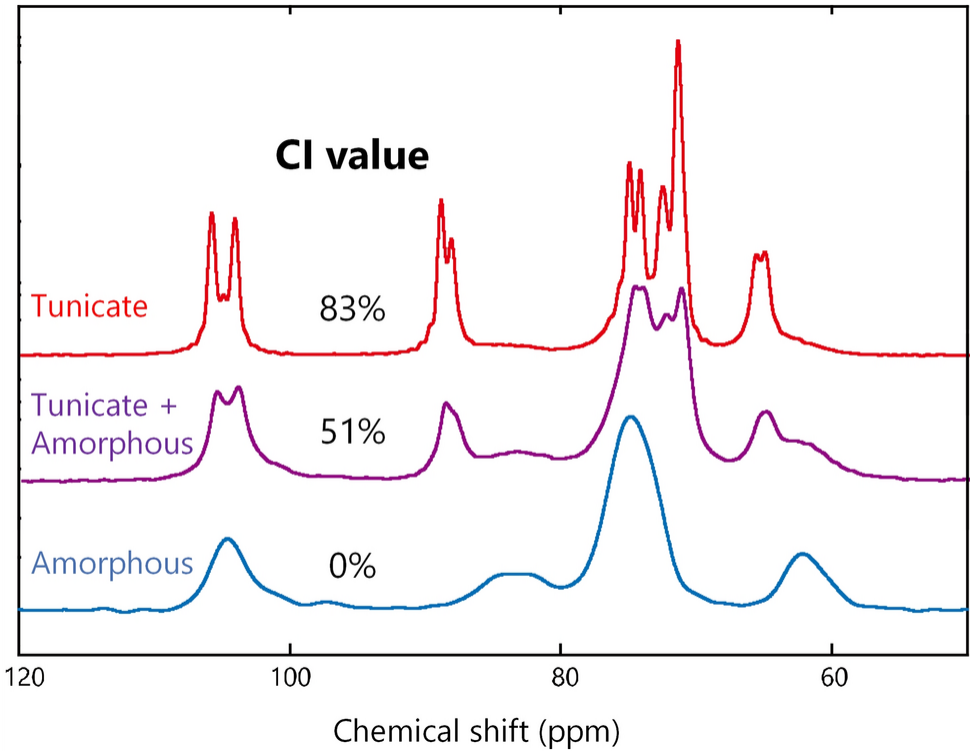

Figure A.2. NMR spectra of tunicate cellulose, a mixture of the tunicate and amorphous celluloses, and amorphous cellulose at 2 ms CT. The mass ratio of the tunicate cellulose in the mixture was 60%.

The CI values for all the samples were then plotted against the CT (Figure A.1d). In the range of approximately 1–2 ms CT, where the signal intensities were at a maximum, the CI values of each sample were almost the same, and the difference in the CI values was within

only 3%. At over 2 ms CT, the CI values gradually increased. This is because of the decrease in the intensity of the noncrystalline region resulting in overestimation of the CI value (see Figure A.1c).

For a quantitative demonstration, the CI value of the mixture of the tunicate and amorphous cellulose was calculated from the NMR spectra recorded at 2 ms CT (Figure A.2). The calculated CI value was 51%, which is in good agreement with the ideal value (49%) determined gravimetrically. These results indicate that, although the CP/MAS NMR spectroscopy is generally not quantitative for polymers having crystalline and amorphous regions, it is possible to evaluate the CI value of cellulose with an accuracy <3% from the NMR spectra at the optimized CT of 2 ms.

A.3.2 Carboxylate groups at the C6

In the process of CNF production, cellulose is often surface modified in advance before wet disintegration. One example is by TEMPO oxidation. By this method, the primary hydroxy groups exposed on the surface of the cellulose crystallite were converted to carboxyl groups, maintaining the crystallinity [21]. Figure A.3a shows the NMR spectra of the C6 carbonyl region of TO-DP and TO-CNF at various CTs (0.1–10 ms). Both the shape and intensity of these NMR spectra changed depending on the CT, similarly to the C4 region.

The signal intensities of the carbonyl carbon were then plotted against the CT, see Figure A.3b. Interestingly, TO-DP having bundled microfibrils showed similar CP dynamics with TO-CNF. The signal intensities of the carbonyl carbon increased more slowly than the signals of the C4 carbon, and then reached a maximum at approximately 3 ms. In other words, the T_{CH} of the carbonyl carbon was larger than that of the C4 carbons (see Figure. A.1 for the dependency of the CT to the signal intensity of the C4 carbons). This is likely because of the longer distance between the proton and carbonyl carbon. Furthermore, the signal intensities of the TO-DP were the same as that of the TO-CNF. This result indicates that the mobility of the carbonyl carbon on the surface of cellulose crystallite is independent of the crystal size.

Figure A.3c shows the change in the NMR spectra at 2 ms CT before and after TEMPO oxidation. The signals corresponding to C=O, trans-gauche (*tg*), gauche-trans (*gt*), and gauche-gauche (*gg*) are centered at approximately 174.8, 65.2, 62.6, and 60.6 ppm, respectively [22]. By

the oxidation, the signal corresponding to the noncrystalline *gg* or *gt* was remarkably decreased, whereas the signal of the crystalline *tg* ratio remained constant, and the signal of the carbonyl carbon appeared at approximately 175 ppm. As shown in Figure A.3d, there was a 19% decrease in the signal ratio of the noncrystalline hydroxy group, and this value is in good agreement with the increase in the signal of the carbonyl carbon (22%). This result is consistent with data reported by Montanari *et. al.* [23], suggesting the conversion to carboxyl groups from the hydroxy groups can be evaluated from the NMR spectra under optimized conditions.

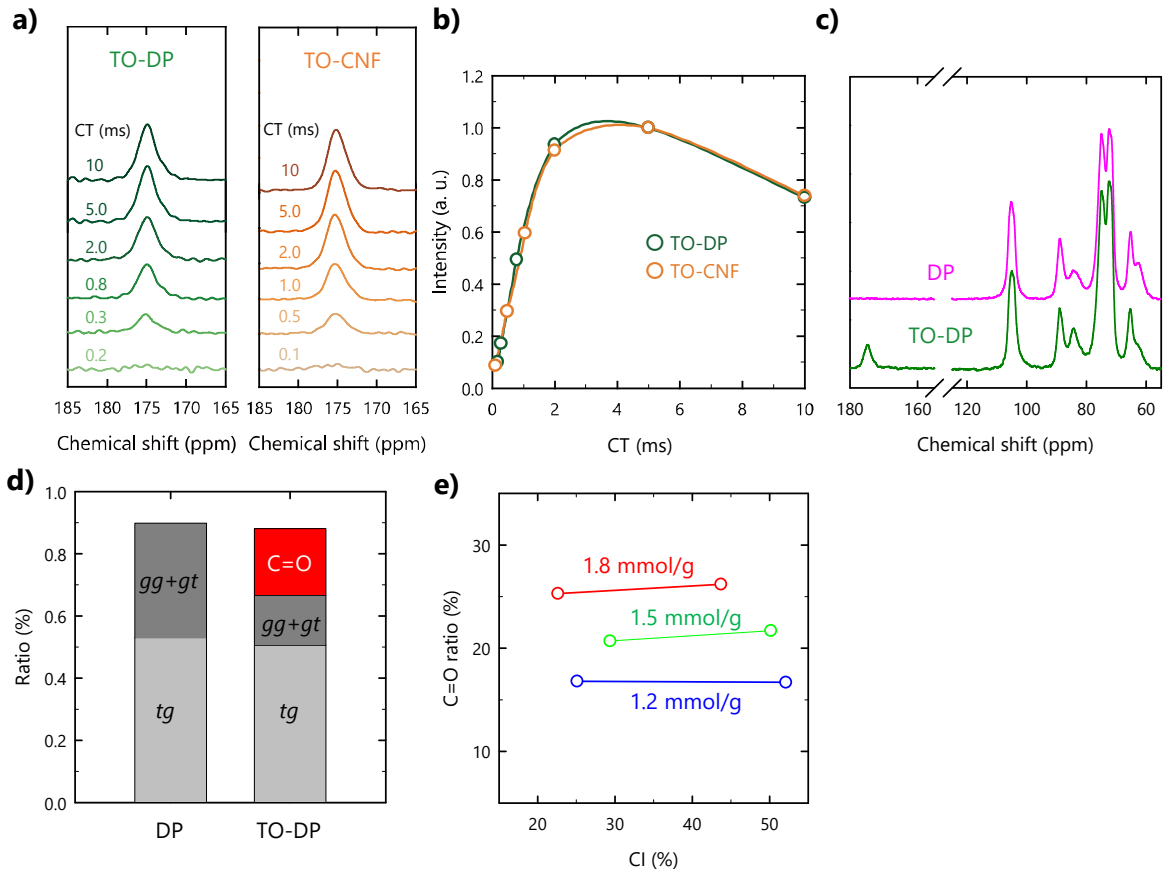

Figure A.3. a) Spectral change in the carbonyl region of TO-DP and TO-CNF with CT. **b)** Dependency of CT on the signal intensity corresponding to the carbonyl carbon. **c)** Change in the NMR spectra at 2 ms CT with TEMPO-oxidation. **d)** Change in the signal ratio of the conformation of the C6 hydroxy group and carbonyl carbon. **e)** Relationship between the CI value and the carbonyl ratio calculated as the signal ratio of the carbonyl carbon to the C1 carbon.

Furthermore, the relationship between the CI value and the degree of oxidation of the samples, see Figure A.3e, shows that the degree of oxidation can be evaluated from the NMR spectra at the optimized CT, irrespective of the crystallinity of cellulose. Note here that the total C6 signal intensities were slightly smaller than the C1 signal intensity, and the degree of oxidation evaluated from the spectrum was lower by approximately 16% than that estimated from conductivity titrations (Figure A.3e). This is probably because the chemical structure and molecular mobility are different between the C6 noncrystalline carbons and C1 carbons [9, 24], and both the total C6 signal and the amount of the carboxy groups were underestimated in the present pulse condition.

A.3.3 Relationship between C4-based CI value and C6-based *tg* ratio

Based on a computational study, it has been reported that the conformation of the exocyclic groups at C6 significantly influences the C4 peak separation, and the signal at approximately 89 ppm, corresponding to the crystalline C4 carbon, is dominated by the *tg* conformation [25]. Figure A.4 shows the relationship between the C4-based CI value and the C6-based *tg* ratio of samples with different crystal sizes. Interestingly, the CI value was found to be linearly correlated to the *tg* ratio, with a slope of 0.9 ($R^2 = 0.98$). Note here that the calculation of the *tg* ratio is different from the method described in Chapter 2–4, and the *tg* ratio exclude the contribution of C6 carbonyl carbon. This result demonstrates that the change in the C4 crystalline signal is strongly affected by the *tg* conformation. The slight difference from 1.0 in the slope leads to the interpretation that the glycosidic linkage is partly restricted even when the C6 hydroxy groups sit in the noncrystalline conformation [25].

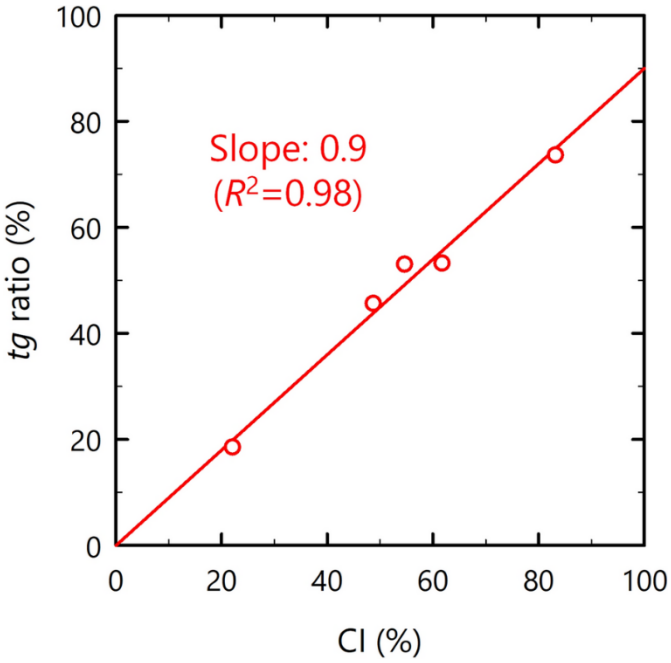

Figure A.4. Relationship between the CI value and *tg* ratio.

A.4 References

1. Horii, F.; Hirai, A.; Kitamaru, R., Solid-state high-resolution 13C-NMR studies of regenerated cellulose samples with different crystallinities. *Polymer Bulletin* **1982,** *8* (2-4).

2. Atalla, R. H.; Vanderhart, D. L., Native cellulose: a composite of two distinct crystalline forms. *Science* **1984,** *223* (4633), 283-5.

3. Newman, R. H.; Hemmingson, J. A., Determination of the Degree of Cellulose Crystallinity in Wood by Carbon-13 Nuclear Magnetic Resonance Spectroscopy. *Holzforschung* **1990,** *44* (5), 351-356.

4. Kono, H.; Yunoki, S.; Shikano, T.; Fujiwara, M.; Erata, T.; Takai, M., CP/MAS (13)C NMR study of cellulose and cellulose derivatives. 1. Complete assignment of the CP/MAS (13)C NMR spectrum of the native cellulose. *J Am Chem Soc* **2002,** *124* (25), 7506-11.

5. Vietor, R. J.; Newman, R. H.; Ha, M. A.; Apperley, D. C.; Jarvis, M. C., Conformational features of crystal-surface cellulose from higher plants. *Plant J* **2002,** *30* (6), 721-31.

6. Phyo, P.; Wang, T.; Yang, Y.; O'Neill, H.; Hong, M., Direct Determination of Hydroxymethyl Conformations of Plant Cell Wall Cellulose Using (1)H Polarization Transfer Solid-State NMR. *Biomacromolecules* **2018,** *19* (5), 1485-1497.

7. Earl, W. L.; VanderHart, D. L., Observations by high-resolution carbon-13 nuclear magnetic resonance of cellulose I related to morphology and crystal structure. *Macromolecules* **1981,** *14* (3), 570-574.

8. Larsson, P. T.; Wickholm, K.; Iversen, T., A CP/MAS13C NMR investigation of molecular ordering in celluloses. *Carbohydrate Research* **1997,** *302* (1-2), 19-25.

9. Hill, D. J. T.; Le, T. T.; Whittaker, A. K., A technique for the quantitative measurements of signal intensities in cellulose-based transformer insulators by13C CPMAS NMR. *Cellulose* **1994,** *1* (4), 237-247.

10. Heux, L.; Dinand, E.; Vignon, M. R., Structural aspects in ultrathin cellulose microfibrils followed by 13C CP-MAS NMR. *Carbohyd Polym* **1999,** *40* (2), 115-124.

11. Daicho, K.; Kobayashi, K.; Fujisawa, S.; Saito, T., Crystallinity-Independent yet Modification-Dependent True Density of Nanocellulose. *Biomacromolecules* **2020,** *21* (2), 939-945.

12. Daicho, K.; Saito, T.; Fujisawa, S.; Isogai, A., The Crystallinity of Nanocellulose: Dispersion-Induced Disordering of the Grain Boundary in Biologically Structured Cellulose. *Acs Applied Nano Materials* **2018,** *1* (10), 5774-5785.

13. Okita, Y.; Saito, T.; Isogai, A., Entire surface oxidation of various cellulose microfibrils by TEMPO-mediated oxidation. *Biomacromolecules* **2010,** *11* (6), 1696-700.

14. Nemoto, J.; Saito, T.; Isogai, A., Simple Freeze-Drying Procedure for Producing Nanocellulose Aerogel-Containing, High-Performance Air Filters. *ACS Appl Mater Interfaces* **2015,** *7* (35), 19809-19815.

15. Terenzi, C.; Prakobna, K.; Berglund, L. A.; Furo, I., Nanostructural effects on polymer and water dynamics in cellulose biocomposites: (2)h and (13)c NMR relaxometry. *Biomacromolecules* **2015,** *16* (5), 1506-15.

16. Sparrman, T.; Svenningsson, L.; Sahlin-Sjovold, K.; Nordstierna, L.; Westman, G.; Bernin, D., A revised solid-state NMR method to assess the crystallinity of cellulose. *Cellulose* **2019,** *26* (17), 8993-9003.

17. Funahashi, R.; Okita, Y.; Hondo, H.; Zhao, M.; Saito, T.; Isogai, A., Different Conformations of Surface Cellulose Molecules in Native Cellulose Microfibrils Revealed by Layer-by-Layer Peeling. *Biomacromolecules* **2017,** *18* (11), 3687-3694.

18. Oehme, D. P.; Downton, M. T.; Doblin, M. S.; Wagner, J.; Gidley, M. J.; Bacic, A., Unique aspects of the structure and dynamics of elementary Ibeta cellulose microfibrils revealed by computational simulations. *Plant Physiol* **2015,** *168* (1), 3-17.

19. Wickholm, K.; Larsson, P. T.; Iversen, T., Assignment of non-crystalline forms in cellulose I by CP/MAS 13C NMR spectroscopy. *Carbohydrate Research* **1998,** *312* (3), 123-129.

20. Isogai, A.; Atalla, R. H., Amorphous celluloses stable in aqueous media: Regeneration from SO2–amine solvent systems. *Journal of Polymer Science Part A: Polymer Chemistry* **1991,** *29* (1), 113-119.

21. Saito, T.; Hirota, M.; Tamura, N.; Kimura, S.; Fukuzumi, H.; Heux, L.; Isogai, A., Individualization of nano-sized plant cellulose fibrils by direct surface carboxylation using TEMPO catalyst under neutral conditions. *Biomacromolecules* **2009,** *10* (7), 1992-6.

22. Horii, F.; Hirai, A.; Kitamaru, R., Solid-state 13C-NMR study of conformations of oligosaccharides and cellulose. *Polymer Bulletin* **1983,** *10* (7-8), 357-361.

23. Montanari, S.; Roumani, M.; Heux, L.; Vignon, M. R., Topochemistry of Carboxylated Cellulose Nanocrystals Resulting from TEMPO-Mediated Oxidation. *Macromolecules* **2005,** *38* (5), 1665-1671.

24. Horii, F.; Hirai, A.; Kitamaru, R., CP/MAS Carbon-13 NMR Study of Spin Relaxation Phenomena of Cellulose Containing Crystalline and Noncrystalline Components. *Journal of Carbohydrate Chemistry* **2006,** *3* (4), 641-662.

25. Yang, H.; Wang, T.; Oehme, D.; Petridis, L.; Hong, M.; Kubicki, J. D., Structural factors affecting 13C NMR chemical shifts of cellulose: a computational study. *Cellulose* **2017,** *25* (1), 23-36.

Acknowledgments

This thesis is a compilation of studies carried out from April 2016 to March 2021 under my supervisor, Associate Professor Saito Tsuguyuki at the University of Tokyo. I would like to express my deepest respect and appreciation to Associate Professor Saito Tsuguyuki for his generous guidance and continuous encouragement throughout this research.

I am grateful to Professor Isogai Akira, Assistant Professor Fujisawa Shuji, and Kobayashi Kayoko for their continuous encouragement and advice. I thank Dr. Ono Yuko, Dr. Kimura Minoru, Dr. Isobe Noriyuki, Dr. Tanaka Reina, Dr. Sun Zhifang, Dr. Soeta Hiroto, Dr. Ning Ruizhi, Dr. Zhou Yaxin, Dr. Goi Yosuke, Dr. Nemoto Junji, Dr. Takeuchi Miyuki, Dr. Lavoine Nathalie, Mr. Mengchen Zhao, Mr. Sakuma Wataru, Mr. Ishioka Shun, Mr. Nakamura Yasutaka, Mr. Kubo Ryuji, Mr. Yamasaki Syunsuke, Mr. Ochiai Yu, Mr. Kaku Yuto, Mr. Kotsuka Junki, Mr. Ishida Suguru, Mr. Ito Tomoki, Mr. Yagita Yasuhito, Mr. Iijima Takumi, Mr. Tamura Naoki, Mr. Doi Yoshinori, Ms. Sato Yuriko, and the other members of the Pulp & Paper Science laboratory for their kind cooperation and advice.

Dr. Nishiyama Yoshiharu provided useful suggestions and advice about the XRD measurement and crystal structure of cellulose. Discussions on the microfibril structure with Dr. Pan Chen in KTH were very insightful. I would like to thank Dr. Furihata Kazuo and Dr. Ashida Jun for their technical support and the valuable suggestions of solid-state NMR. I sincerely thank Dr. Ishida Yasuhiro and Dr. Sano Koki for the SAXS measurements and fruitful discussions. I also thank Associate Professor Koga Hirotaka for the measurement of the electrical properties and insightful discussions. Professor Berglund Lars, Dr. Rojass Ramiro, and Dr. Willhammer Tom gave me precious opportunities to discuss with researchers and showed me gracious hospitality during my visit to Stockholm. I would like to express my gratitude to them for their favors. I would like to thank Associate Professor Kontturi Eero, Dr. Tekla Tammelin, and Assistant Professor Stefan Spirk for instructive discussions and great opportunities in a summer school in Finland in 2018. I gratefully acknowledge Dr. Alfred French, Professor Kim Seong, Dr. Laurent Heux, Professor Nogi Masaya, Professor Lennart Bergstrom, and other researchers for their valuable advice and sincere encouragement.

Acknowledgments

My supervisor in my undergraduate course, Professor Sawatari Chie, introduced me to the field of cellulose science. I would like to express my gratitude to her for her support and encouragement.

Special thanks are extended to Professor Tadahisa Iwata, Professor Kiyohiko Igarashi, Professor Saito Yukie, and Professor Masahisa Wada for their careful review of this thesis and valuable suggestions and comments.

I have been a research assistant as part of the JST-Mirai R&D Program from 2018 to 2020, and the Japan Society for Promotion of Science from 2020 to 2021. I would like to express my gratitude to all the people mentioned above. I would like to acknowledge the financial support from the JST-Mirai R&D Program and the Research Fellowship for Young Scientists from the Japan Society for the Promotion of Science, PHOENIX Grant-in-Aid, and Research Program for Next Generation Young Scientists of Dynamic Alliance for Open Innovation Bridging Human, Environment, and Materials in Network Joint Research Center for Materials and Devices.

Last but not least, I thank my family for their sincere support and encouragement.

March 19, 2021

Kazuho Daicho

大長 一帆

Publications

Peer-reviewed journal articles

1. **Daicho, K.**, Saito, T., Fujisawa, S., Isogai, A., The Crystallinity of Nanocellulose: Dispersion-Induced Disordering of the Grain Boundary in Biologically Structured Cellulose. *ACS Applied Nano Materials* **2018**, 1 , 5774-5785.
2. **Daicho, K.**, Kobayashi, K., Fujisawa, S., Saito, T., Crystallinity-Independent yet Modification-Dependent True Density of Nanocellulose. *Biomacromolecules* **2020**, 21 , 939-945.
3. **Daicho, K.**, Fujisawa, S., Kobayashi, K., Saito, T., Ashida, J., Cross-polarization dynamics and conformational study of variously sized cellulose crystallites using solid-state ^{13}C NMR. *Journal of Wood Science* **2020**, 66 , 62.
4. Medina, L., Nishiyama, Y., **Daicho, K.**, Saito, T., Yan, M., Berglund, L. A., Nanostructure and Properties of Nacre-Inspired Clay/Cellulose Nanocomposites—Synchrotron X-ray Scattering Analysis. *Macromolecules* **2019**, 52 , 3131-3140.
5. Yamasaki, S., Sakuma, W., Yasui, H., **Daicho, K.**, Saito, T., Fujisawa, S., Isogai, A., Kanamori, K., Nanocellulose Xerogels With High Porosities and Large Specific Surface Areas. *Frontiers in chemistry* **2019**, 7, 316.
6. Hirano, T., Mitsuzawa, K., Ishioka, S., **Daicho, K.**, Soeta, H., Zhao, M., Takeda, M., Takai, Y., Fujisawa, S., Saito, T., Anisotropic Thermal Expansion of Transparent Cellulose Nanopapers. *Frontiers in chemistry* **2020**, 8, 68.
7. Willhammar, T., **Daicho, K.**, Johnstone, D., Kobayashi, K., Liu, Y., Midgley, P., Bergström, L., Saito, T., Local Crystallinity in Twisted Cellulose Nanofibers. *ACS Nano*, **2020**, 15, 2, 2730-2737.
8. Adachi K., **Daicho, K**., Furuta K., Shiga, T., Saito, T., Kodama T. , Thermal conduction through individual cellulose nanofibers, *Appl. Phys. Lett.*, **2021**, 118, 053701.

Reviews

1. 大長一帆, 齋藤継之, ナノセルロースの結晶性解析, *ナノセルロースジャパン 研究最前線シリーズ*, **2020**
2. 大長一帆, 齋藤継之, ナノセルロースの真密度, *ナノセルロースジャパン 研究最前線シリーズ*, **2020**
3. 大長一帆, 齋藤継之, セルロースナノファイバーの結晶性解析, *Cellulose Communications* **2020**, 27, 3, 85-90

International conference

Oral presentation (Peer-reviewed)

1. **Daicho, K.**, Saito, T., Fujisawa, S., Isogai, A., Dispersion-induced Disordering of the Grain Boundary in Wood Cellulose Governs the Crystallinity of Nanocellulose. 2018 SWST/JWRS International Convention, Nagoya, Japan, **2018**.
2. **Daicho, K.**, Saito, T., Fujisawa, S., Isogai, A., Crystallinity of nanocellulose: Dispersion-induced disordering of the grain boundary in biologically structured cellulose. 257th ACS National Meeting & Exposition, Orlando, **2019**.
3. **Daicho, K.**, Kobayashi, K., Fujisawa, S., Saito, T., Crystallinity-Independent yet Modification-Dependent True Density of Nanocellulose. The 6th EPNOE International Polysaccharide Conference, Aveiro, **2019**.

Oral presentation

1. **Daicho, K.**, Saito, T., Isogai, A., The dispersion-induced disordering of the fibril interfaces in biologically-structured cellulose determines the crystallinity of cellulose nanofibers. Nanocellulose seminar, Stockholm, **2017**.
2. **Daicho, K.**, Saito, T., Isogai, A., Crystallinity index of cellulose nanofibers: The assembly and dispersion of cellulose microfibrils as a dominant factor to determine their surface molecular conformation. UT-RIKEN Soft Matter Joint Seminar, Saitama, **2017**.

3. **Daicho, K.**, Kobayashi, K., Fujisawa, S., Saito, T., Crystallinity-Independent yet Modification-Dependent, True Density of Nanocellulose. The 2nd RIKEN-UT joint seminar, Tokyo, **2019**.

Poster presentation (Peer-reviewed)

1. **Daicho, K.**, Saito, T., Fujisawa, S., Isogai, A., The crystallinity of nanocellulose: Assembly-induced ordering and dispersion-induced disordering of the grain boundary in biologically structured cellulose. MoDeSt2018, Tokyo, **2018**.
2. **Daicho, K.**, Saito, T., Fujisawa, S., Isogai, A., Dispersion-Induced Disordering of the Grain Boundary in Wood Cellulose. TAPPI Nano 2019, Chiba, **2019**.

Domestic conference

Oral presentation

1. 大長一帆, 小野祐子, 齋藤継之, 磯貝明, 木材パルプ及びセルロースナノファイバーの結晶性評価. 第 67 回日本木材学会大会, 福岡, 2017 年.
2. 大長一帆, 小野祐子, 齋藤継之, 磯貝明, セルロースナノファイバーの結晶性解析. 平成 29 年度繊維学会年次大会, 東京, 2017
3. 大長一帆, 小野祐子, 齋藤継之, 磯貝明, セルロースナノファイバーの結晶性評価（III）. 第 68 回日本木材学会大会, 京都, **2018**.
4. 大長一帆, 齋藤継之, 藤澤秀次, 磯貝明, ナノセルロースの結晶性：分散と会合が支配する界面構造. セルロース学会第 25 回年次学会, 京都, **2018**.
5. 大長一帆, CNF 素材の結晶性. JFlex 2019, 東京, **2019**.
6. 大長一帆, 齋藤継之, 藤澤秀次, 磯貝明., セルロースナノファイバーの真密度 ― 結晶性および表面改質との相関分析. 第 86 回紙パルプ研究発表会, 東京, **2019**.
7. 大長一帆, ナノセルロースの結晶性解析. セルロース学会関東支部ミニシンポジウム, 東京, **2019**.
8. 大長一帆, セルロースナノファイバーの結晶性：分散と会合が支配する界面構造. 第一工業製薬 若手研究者スキルアップセミナー, 東京, **2020**.

9. 大長一帆, 小林加代子, 藤澤秀次, 齋藤継之, CNF 間相互作用が結晶性を回復させる. 第 71 回日本木材学会大会, 東京, **2020**.

Poster presentation

1. 大長一帆, 小野祐子, 齋藤継之, 磯貝明, 澤渡千枝, セルロースナノファイバーの結晶性評価（II）. セルロース学会第 24 回年次学会, 岐阜, **2017**.
2. 大長一帆, 齋藤継之, 藤澤秀次, 磯貝明., ナノセルロースの結晶性：会合と分散が支配する界面構造. 第 9 回 島津 新素材セミナー2018, 東京, **2018**.
3. 大長一帆, 齋藤継之, 小林加代子, 藤澤秀次, 磯貝明, ナノセルロースの真密度：結晶性と表面改質の寄与. 第 69 回日本木材学会大会, 函館, **2019**.
4. 大長一帆, 齋藤継之, 小林加代子, 藤澤秀次, 磯貝明, 結晶性に依存せず表面改質に依存するナノセルロースの真密度, セルロース学会第 26 回年次学会, 福岡, **2019**.
5. 大長一帆, 齋藤継之, 藤澤秀次, 磯貝 明, 小林加代子, ナノセルロースの結晶性操作. 第 70 回日本木材学会大会, 鳥取, **2020**.

Awards

1. 第 69 回 日本木材学会大会, 優秀ポスター賞
2. 2019 年度 日本木材学会 優秀女子学生賞
3. 令和２年度 農学生命科学研究科 研究科長賞